PHOTOELEKTROCHEMISCHE BILDUNG UND UMWANDLUNG VON GRENZFLÄCHENPHASEN IN n-$CuInSe_2$/ELEKTROLYT SOLARZELLEN

PHOTOELECTROCHEMICAL FORMATION AND TRANSFORMATION OF INTERPHASES AT n-$CuInSe_2$/ELECTROLYTE JUNCTION SOLAR CELLS

Inaugural - Dissertation

zur Erlangung der Doktorwürde
der Freien Universität Berlin
Fachbereich Chemie

Vorgelegt von

Shalini Menezes

1985

UNIV.
LEIDEN.
MUS.

PHOTOELEKTROCHEMISCHE BILDUNG UND UMWANDLUNG VON GRENZFLÄCHENPHASEN IN n-$CuInSe_2$/ELEKTROLYT SOLARZELLEN

PHOTOELECTROCHEMICAL FORMATION AND TRANSFORMATION OF INTERPHASES AT n-$CuInSe_2$/ELECTROLYTE JUNCTION SOLAR CELLS

Inaugural - Dissertation

zur Erlangung der Doktorwürde
der Freien Universität Berlin
Fachbereich Chemie

Vorgelegt von

Shalini Menezes

Prof. H. Tributsch
W. Thiele

Prom.: 1.2.85

ABSTRAKT

Durch Kontrolle elektrochemischer Parameter wurde eine photoelektrochemische Solarzelle mit einem Wirkungsgrad von 12% entwickelt, deren Funktionsweise auf einer in-situ Filmbildung am Halbleiter-Elektrolyt Kontakt beruht. Zur detaillierten Untersuchung der Umwandlung an der Grenzflache wurden voltammetrische sowie oberflachenanalytische Verfahren in verschiedenen Stadien der Filmbildung eingesetzt. $CuInSe_2$ passiviert in neutralen und alkalischen Losungen unter Bildung von Oxiden, die eine deutliche Verringerung der charge transfer Kinetik in S^{2-}/S_x^{2-} (pH 14) sowie J^-/J_2 (pH 7) bewirken. In saurem Medium wird eine Abnahme der Oberflachenpassivitat und effiziente Photooxidation von Iodid beobachtet. Die Zell-Leistung nimmt jedoch schnell unter gleichzeitiger Bildung von CuJ Kristalliten und elementarem Se ab. CuJ lost sich teilweise unter Bildung von CuJ_2^-. Die Zugabe von 20 mM CuJ zum Elektrolyten bewirkt eine Anderung der Umwandlung der Halbleiteroberflache durch Erzeugung eines Films aus hexagonalen Kristalliten. Bei Belichtung erlaubt dieser Film effizienten charge transfer zwischen n-$CuInSe_2$ und dem J^--J_2-Cu^+-HJ Elektrolyten bei gleichzeitiger Unterdruckung der Korrosionsreaktion. Selbst nach ausgedehnten Stabilitatstests (70,000 Cb/cm^2) wachst die Filmdicke nicht uber ~2um. Dieser photoelektrochemisch synthetisierte Film besteht uberwiegend aus $CuJSe_3$ und bis zu 30% Se Und ist p-leitend. Die Analyse der Energieniveaus von n-$CuInSe_2$, p-leitendem Film und des Elektrolyten weist darauf hin, dass die photoaktive Barriere zwischen Halbleitersubstrat und dem Film lokalisiert ist, wobei der Elektrolyt als Frontkontakt wirkt. Tempern an Luft nach der Herstellung bewirkt eine Restrukturieung der Grenzflachenphase unter Ausbildung hexagonaler Saulen von $CuJSe_3$ und binaren Strukturen von Cu und J bzw. In und J. Im Kontakt mit dem Elektrolyten erfolgen weitere Unwandlungen, bei denen quaternare Verbindungen der Elemente Cu, In, Se und I unterschiedlicher Stoichiometrie erzeugt werden, die offenbar eine Erhohung der Leistungsdaten der Solarzelle bewirken.

ABSTRACT

A 12% efficient and stable n-$CuInSe_2$ based photoelectrochemical solar cell has been developed by in-situ interfacial film formation, induced by controlling electrochemical parameters. The interface was analyzed during various stages of the cell development by voltammetric and surface analytical methods. $CuInSe_2$ passivates in neutral and alkaline solutions forming oxides which contribute to the sluggish charge transfer kinetics in S^{2-}/S_x^{2-} (pH 14) and I^-/I_2 (pH 7) electrolytes. Reduced surface passsivity and efficient photooxidation of the iodide species is observed in an acidic medium. The cell output, however, degrades rapidly via concurrent formation of triangular CuI crystallites and elemental Se. CuI dissolves partially via CuI_2^- formation. Addition of 20mM CuI to the electrolyte transforms the electrode surface generating a film comprising of hexagonal crystallites. Under illumination this film mediates efficient charge transfer between the $CuInSe_2$ and I^--I_2-Cu^+-HI electrolyte while inhibiting corrosion and does not grow beyond ~2 microns even after extended (70,000 C/cm^2) stability tests. The photoelectrochemically synthesized film comprises mainly $CuISe_3$ and upto 30% Se, and exhibits p-type conductivity. Correlation of the energy levels of n-$CuInSe_2$, p-film and the electrolyte suggests that the principal barrier is located in the solid p-n heterojunction with the electrolyte providing the front contact. Post growth air anneal results in restructured interphase comprising of hexagonal columns of $CuISe_3$ and binary structures of Cu and I, or In and I. Exposure of the annealed surface to the electrolyte leads to further transformations generating quarternary composites of Cu, In, Se and I with different stoichiometries which contribute to a higher cell efficiency.

Digitized by the Internet Archive
in 2026

https://archive.org/details/lA41549615_0019

CONTENTS

Introduction 1

1. Stabilization Strategy 6
   1.1. Reaction Paths in Photoelectrochemical Cells 6
   1.2. Films Grown in-situ from Corrosion Products 7

2. Photoelectrochemical Reactions with Rotating Ring-Semiconductor Disk Electrodes 10
   2.1. Rotating Ring-Disk Voltammetry 10
   2.2. Interplay of Photon Flux and Mass Flux Current Control Modes 13
   2.3. Ring Monitoring of Redox Potentials 16

3. Experimental 17
   3.1. Electrochemical Experiments 17
   3.2. Surface Analysis 21

4. Films and their Impact on Charge or Mass Transport 23
   4.1. Types of Interfacial Films on Semiconductors 23
   4.2. EIS and EMIS Structures 24
   4.3. Effects of Electrolyte pH on Formation and Dissolution of Films 29
   4.4. Surface Films on GaInPAs 30
      4.4.1. Behavior in Supporting Electrolytes 30
      4.4.2. Redox Reactions in Acids and Bases 32

5. Interfacial Electrochemistry of $CuInSe_2$ 36
   5.1. Surface Reactions 36
   5.2. Behavior in Alkaline Polysulfide 39
   5.3. Behavior in Neutral and Alkaline Polyiodide 41

6. Partly Soluble Interphase 44
6.1. Voltammetry of $CuInSe_2$ in Iodide/Iodine 44
6.1.1. Characteristics of I^-/I_2 Couple 44
6.1.2. Behavior in Concentrated Iodide under Photon Flux Control 46
6.1.3. Mass Flux Controlled Reactions in Dilute I^-/I_2 at pH 0. 49
6.1.4. Behavior at pH 7. Effect of H^+ 54
6.2. Analysis of Corroded Surfaces 56
6.3. Voltammetry of $CuInSe_2$ in $Cu^{+/++}$ 59
6.3.1. Characteristics of $Cu^{+/++}$ Couple 59
6.3.2. Redox Reactions and Surface Incorporation of $Cu^{+/++}$ 61
6.4. Reactions at $CuInSe_2$ in a Composite Electrolyte of Cu^+, I^-, I_2 and H^+ ions 66
6.5. Formation and Dissolution of CuI 69
6.6 Corrosion Inhibition via Film Formation 71

7. Stable Semiconducting Interphase 72
7.1. Photoelectrochemical Film Growth 72
7.2. Cell Performance and Stability after Film Formation 73
7.3. Film Composition, Morphology during and after Growth 74
7.4. Film Identification 79
7.4.1. Oxidation States of Components, Depth Profile 79
7.4.2. X-Ray Diffraction Analysis 82
7.5. Surface Conversion of $CuInSe_2$ to $CuISe_3$-Se 84
7.6. Opto-Electronic Properties of the Film 87
7.6.1. Spectral Response 87
7.6.2. Microwave Conductivity 88
7.6.3. Electronic Structure 89

8. Transformation to an Efficient Interphase 92
8.1. Effects of Surface Pretreatments 92
8.1.1. Chemical Etching of Surface Layers 93
8.1.2. Mechanical Polishing 97
8.2. Influence of Crystal Orientation 100
8.3. Concentration Dependance of Electrolyte Constituents 102
8.4. Influence of Ambient Temperature 107
8.5. Post Growth Air Anneal 112
8.6. Morphology and Composition of Annealed Films 115
8.7. Transformation of $CuISe_3$-Se to $CuIn_xI_ySe_z$
8.8. Performance of $n\text{-}CuInSe_2/p\text{-}CuISe_3\text{-}CuIn_2ISe_3/I^-\text{-}I_2\text{-}Cu^+\text{-}HI/C$ cell. 123

Summary 125

References 129

INTRODUCTION

Interphases generally exhibit structures and properties different from the bulk materials constituting a junction and can thus exert a major influence on their behavior. A fundamental understanding of the interfacial phenomena is crucial to the elucidation of materials properties and in devising structures with dissimiliar materials. Reasons underlying active interest in interfaces, including the present work, are related to the dominant role that they play in solar energy conversion systems. This study focusses on the interfacial chemistry at the semiconductor-electrolyte junction and its role in photoelectrochemical (PEC) solar cells and heterojunctions.

PEC cells utilize the semiconductor-electrolyte junction for optical to electrical conversion in regenerative photovoltaic cells and to chemical conversion in photoelectrolysis cells. In these cells photoactive semiconductor electrodes absorb sunlight to create electron hole pairs which are separated in the space charge layer produced at the semiconductor-electrolyte interface. The separated charge carriers are subsequently injected into the electrolyte to drive chemical reduction and oxidation reactions. The principles of operation of PEC cells and the criteria for selection of components have been the subject of a number of publications and reviews [1-7].

Potential advantages of the regenerative PEC cells over conventional solid state cells include: spontaneous junction formation thus elliminating surface preparation, lattice matching,

doping, diffusion and front contact formation steps; and the relative insensitivity to gross defects in the semiconductor, thus allowing access to polycrystalline materials. The major limitation in the implementation of these advantages is the instability of the semiconductors to photodegration, particularly photoanodes with solar matched band gaps, in aqueous electrolytes.

Thermodynamic considerations show that the photogenerated holes will oxidise n-type semiconductors, unless an adsorbed reductant species can selectively compete for the holes [6,7]. Strong reductants such as Se_2/Se_2^{-2} can scavenge the photoproduced holes at n-GaAs and thus extend the cell lifetime considerably [8]. Incorporation of Ru ions enhances the efficiency [9]. Residual corrosion and deterioration of the surface treatment are the primary limitations of this system. A different approach due to Tributsch, employs transition metal dichalcogenides in which the d-d photoexitation does not break bonds [10]. The n-WSe_2/polyiodide cell is one of the rare examples to sustain long term stability without the requiring stringent sealing [10,12]. The random growth of these materials and the structurally associated defects, such as carrier type inhomogeneity [13], anisotropic conductivity [14] and corrosion along edges [10,11] limit its utility in a practical device. The inherent cathodic protection of photocathodes has been used in the p-InP based cell [15]. Output stability in this system, however, does not match that of the WSe_2 cell, concurrent oxide growth and the deterioration of the surface treatment contributing to the slow degradation of the photocurrent. Other strategies at circumventing decomposition reactions include the use of non-aqueous solvents [16,17], or semiconductor surface modifications (adsorbed ions [9], organic dyes [18,19] and various coatings [20-25]). These approaches have provided a number of new insights into the intricacies of the semiconductor interface and several have succeeded in promoting stability

unfortunately with considerable losses in efficiency. High resistance of non-aqueous electrolytes, redox couple solubility and air sensitivity, and light losses in the coatings are some of the efficiency limiting factors associated with these approaches. Thus the search for semiconductor-electrolyte systems, which can meet the necessary criteria of high efficiency and long term stability continues and simultaneous optimisation of these two key parameters remains a challenging problem.

Performance of PEC cells is critically dependent on the chemistry at the photoactive junction. Operation of the semiconductor in a PEC cell or mere immersion in a redox electrolyte may lead to the formation of an overlayer from insoluble corrosion products, from ion exchange or adsorption of solution species. III-V semiconductors exhibit varying degrees of passivity depending on their constituents, the electrolyte pH and the potential region of film formation [26]. The thickness, conductivity and coherence of these passive films determine their role in PEC cells. If the layer grows thick, a buried semiconductor-semiconductor junction, which may be detrimental to the cell performance, such as the CdS layer in the CdSe/polysulfide/C cell [27], may exist. If the layer is thick and insulating as with the oxide film on GaAs in acetate buffer it can quench current flow to the redox species [28]. The interfacial layer may remain sufficiently thin to allow passage of current by tunneling through an oxide layer in the InP/V(II)-V(III)-HCl/C cell [15,29] or the Ga_2Se_3 layer in the n-GaAs/polyselenide/C cell [9]. One of the more fruitful outcomes of ion-exchange between a semiconductor and an electrolyte is the thin film p-Cu_2S/n-CdS solid state cell, fabricated by dipping CdS into a CuCl solution [30].

From these examples one might deduce that in-situ grown interphases could be advantageously exploited to overcome photocorrosion, if they retain tunneling dimensions or form appropriately matched heterojunctions. The principle of stabilization of PEC cells using corrosion products to grow interfacial films is elaborated in chapter 1. Tayloring interfacial films to combine specific chemical and electronic properties requires a detailed knowledge of the interfacial chemistry between the semiconductor and the electrolyte, judicious selection of electrolyte components and control of the film growth conditions. The rotating ring-semiconductor disk electrode (RRDE) under illumination, introduced in chapter 2, combines the analytical capabilities of the ring, for quantitative identification of reacting species, with precise control of the current by hydrodynamic mass transport as well as by the light flux and is thus used for in-situ elucidation of photoelectrochemical processes at semiconductor-electrolyte interfaces. Ex-situ surface analytical techniques, listed in chapter 3, are used to follow surface transformations and to characterize the interphases grown under various conditions. The role of electrolyte pH and the impact of films in hindering or fostering charge or ion transport is illustrated in chapter 4 with examples of III-V semiconductor based electrolyte-insulator- semiconductor (EIS) and electrolyte-metal-insulator-semiconductor (EMIS) structures, and of surface processes at GaInAsP, as they relate to its two binary components.

Ternary and even more complex semiconductors offer the possibility of using stoichiometry to control band gaps and lattice constants. Although the presence of extra elements introduce additional complexities, they also permit greater flexibility in manipulating interfacial reactions, hence in the design of interfacial layers. Ternary compounds of III-V and

II-IV semiconductors, and their I-III-IV analogues have been explored for energy conversion devices. Considerable attention has been focussed on $CuInSe_2$ for photovoltaic applications because of its direct band gap and unusually steep absorption edge. The low minority carrier diffusion length needed for efficient charge collection makes $CuInSe_2$ ammenable to thin film solar cell construction and has already resulted in efficient thin film and single crystal based photovoltaic devices[31,32].

Photoelectrochemical investigations on the CuIn chalcogenides involve attempts at constructing cells by combining the semiconductors with chalcogenide redox electrolytes [33,34]. Stability in these systems may be derived from the kinetic competition for S^{2-} oxidation versus lattice decomposition. Low conversion efficiencies, resulting from poor fill factors are also attributed to poor kinetics of the S dissolution step. In order to enhance the efficiency while retaining the stability, detailed elucidation of the interfacial processes in various media is required. Surface and redox processes at $CuInSe_2$ are compared in polyiodide and polysulfide in chapter 5. The influence of electrolyte composition, concentration, pH and illumination on these processes are systematicaly examined with the RRDE in chapter 6. These results corroborated with those of surface analysis are used to construct and stabilize a $CuInSe_2$ based PEC cell in chapter 7. Chapter 8 deals with surface transformations using various pre and post film growth treatments to enhance the cell efficiency.

1. STABILIZATION STRATEGY

1.1 REACTION PATHS IN PHOTOELECTROCHEMICAL CELLS

A schematic of a photoelectrochemical cell comprising an n-type semiconductor electrode linked to a metal counter electrode through an external circuit, is shown in figure 1. A redox electrolyte, with both oxidized and reduced species present, completes the electric circuit. Under illumination, electron-hole pairs are generated at the semiconductor surface by photoexitation. Recombination attempts to restore the non-equilibrium carrier densities generated by light to their dark thermal equilibrium values. The electric field at the interface acts to separate the charge carriers which will eventually recombine if no sink is supplied. Three principal channels available to the light generated charge carriers, in PEC cell, are illustrated in figure 1. (1)Recombination at imperfections or interface states can dissipate the e-h pair through radiative or nonradiative processes resulting in a current loss. (2)The more desirable route of regenerative operation, involves charge transfer to the electrolyte. In a n-type semiconductor holes are injected into the donor states, the oxidising species R, and the excited electrons are transported through the external circuit to the counter electrode where they can reduce the species O. The electron energy can be tapped through an external load while the system remains invariant. (3) The more commonly encountered process involves corrosion of the semiconductor surface.

(a)

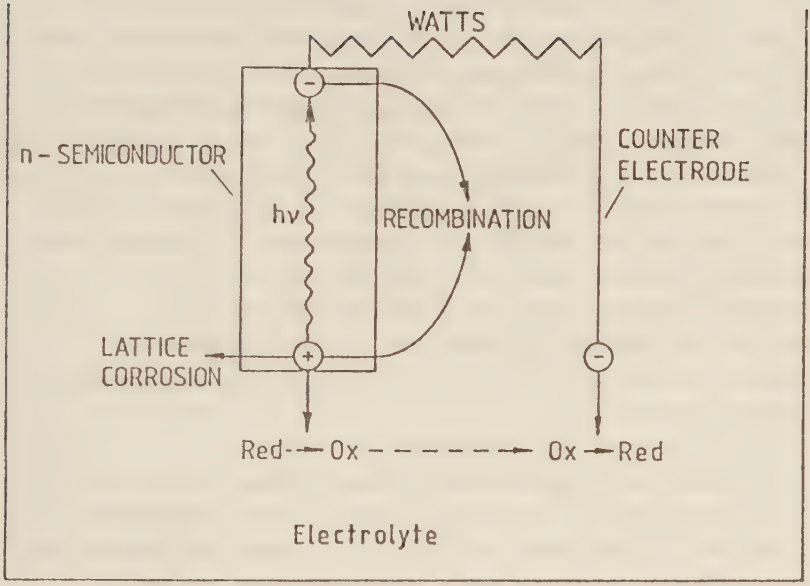

(b)

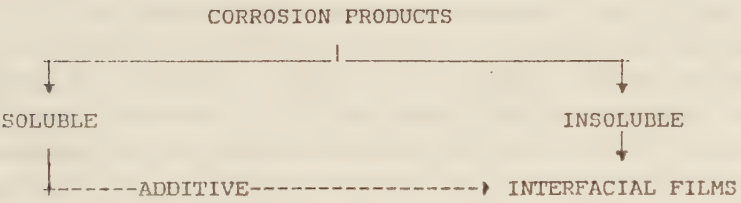

Figure 1. Schematic showing (a) the principal paths of the photoholes in an n-type semiconductor-electrolyte junction cell and (b) the principle of the cell stabilization by in-situ film growth using the corrosion products.

1.2 FILMS GROWN IN-SITU FROM CORROSION PRODUCTS

Corrosion of semiconductor surfaces can proceed by chemical etching or electrochemical corrosion. In chemical etching, a carrier injected by an electrolyte component is localised at the surface of the semiconductor breaking a bond. Electrochemical corrosion occurs during current flow and is related to a carrier from the solid being localized at the surface breaking a bond. Photoanodes are in general less stable than photocathodes because of the relatively slower electrochemical kinetics of photoholes and their ability to photocorrode the lattice anions. Thermodynamic considerations show that all n-type semiconductors are susceptible to photoanodic decomposition [6,7]. The probability of photocorrosion depends, in addition to the interface energetics, on the solubility of the cation and the anion of the semiconductor.

Of particular relevance to this work is the solubility of the products of the corrosion reaction. The semiconductor will dissolve if the ions are soluble (A) when oxidised by the holes to a higher valence state. When the ions from the semiconductor are insoluble (B), a new phase can form on the surface. In this case the corrosion reaction may be advantageously exploited to grow an interfacial layer which can alter the reaction paths. Film formation may be followed by passivation and virtual cessation of all reactions. Under favorable circumstances film formation can lead to reduction of recombination sites in the forbidden gap by terminating the semiconductor lattice, shielding the semiconductor surface against further degradation and continuation of charge transport to the redox electrolyte. Thus by suppressing the two deleterious competing channels the film can reroute the photogenerated charge carriers into the regenerative redox channel.

More commonly encountered systems, particularly in aqueous solutions, are of type A involving soluble corrosion products. The high energy of solvation of photocorroded lattice ions makes the photocorrosion process thermodynamically favorable. Stabilization under these more deleterious circumstances may be possible if film formation is induced by a chemical reaction of the corroding surface with specific electrolyte additives. Thus deliberately induced films could also be taylored to have similar passivating, protecting and charge conducting properties as the type B films.

2. PHOTOELECTROCHEMICAL REACTIONS WITH ROTATING RING-SEMICONDUCTOR DISK ELECTRODES

The rotating disk electrode(RDE) and allied techniques allow precise hydrodynamic control of the flux of electrolyte to and from the reacting surface and may be thus used to unravel reactions associated with charge transfer. The rotating ring-disk electrode (RRDE) configuration extends the capabilities of the RDE allowing quantitative, qualitative and virtually instantaneous identification of electrode processes. It is particularly useful in detecting photoinduced corrosion of semiconductor electrodes, where the consumption or the generation of solution species at the semiconductor disk is monitored by the ring. RDE and RRDE have been the subjects of many books and reviews [35-38]. A brief introduction to the RRDE methodology and its application to processes at illuminated semiconductor electrolyte interfaces is presented here.

2.1. ROTATING RING-SEMICONDUCTOR DISK VOLTAMMETRY

RRDE is illustrated by the composite structure rotating about an axis, z, in Figure 2. The disk electrode of radius r_1 fabricated from semiconductor material is surrounded by a coplanar metal ring electrode of inner radius r_2 and outer radius r_3. The insulating material is also coplanar with the electrode surfaces and prevents lateral contact to the electrolyte and between the two electrodes.

Typical flow lines of the solution species to and from the RRDE are shown by the dashed and solid lines with arrowheads respectively. The disk and ring processes and flow patterns on either side of the z-axis, illustrate the different situations possible by varying the disk and ring potentials, E(D) and E(R), respectively.

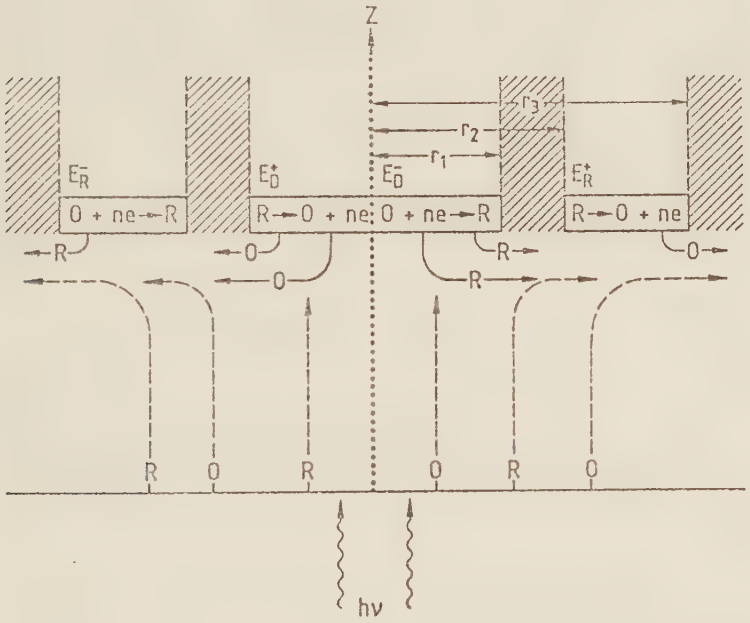

Figure 2. Schematic of rotating ring-semiconductor disk electrode and flow pattern of redox species, O and R, in solution. E(D) and E(R) denote the oxidation(+) and reduction(-) potentials at the disk and ring. r_1, r_2 and r_3 are the disk and inner and outer ring radii.

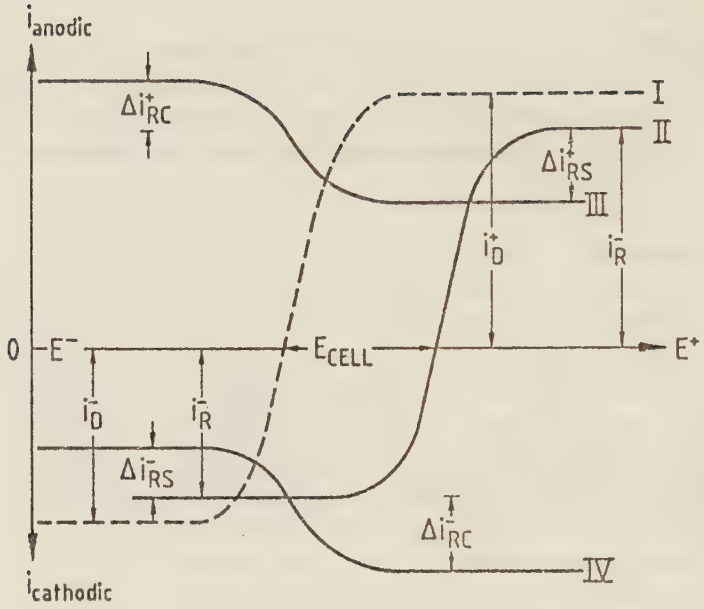

Figure 3. Anodic (+) and cathodic(-) ring and disk currents, i(R) and i(D),in a solution containing a redox couple O/R. Curve I (disk) i(D)-E(D); curve II (ring) i(R)-E(R); curve III (ring at E(R+)) i(R)-E(D); curve IV (ring at E(R-)) i(R)-E(D).

If the solution contains a redox couple O/R in a supporting electrolyte reaction 1 or 2,

$$R \rightarrow O + ne \qquad (1)$$

$$O + ne \rightarrow R \qquad (2)$$

where n denotes the number of electrons, can occur at the illuminated disk depending on the applied disk potential, E(D+) or E(D-). The resultant disk current is given by the Levich equation [35],

$$i(D) = 0.62nFAD^{2/3}v^{-1/6}[C-Cs]w^{1/2} \qquad (3)$$

where F is the Faraday constant, A the area of the disk, D the diffusion coefficient of species R (or O), v the kinematic viscosity, w the radial velocity of rotation, and C and Cs are the bulk and surface concentrations respectively of R (or O).

Curve I of figure 3 represents the disk current-disk potential, i(D)-E(D) curve for the reversible processes in reactions 1 and 2. The maximum anodic(or cathodic) disk current, i(D)L, occurs under total mass transfer, where Cs -->0. Equation 3 then reduces to

$$i(D)L = 0.62nFAD^{2/3}v^{-1/6}Cw^{1/2} \qquad (4)$$

This equation predicts that i(D)L varies linearly with $w^{1/2}$ and the shape of the curve is independant of w.

2.2. INTERPLAY OF PHOTON FLUX AND MASS FLUX CURRENT CONTROL

In the case of an illuminated semiconductor RDE in a PEC cell another variable, namely the photon flux is introduced. The photocurrent response may be controlled by the fluxes of light and mass transport. Interactions between the two modes of current control specify the contributions of the photoactive junction and the electrode reactions. Qualitative electrochemical and quantitative mathematical analyses indicate that the variables controlling the voltammetric behavior of these junctions can interact in an extremely complex fashion

[39,40]. For most cases of interest, it is however possible to design an appropriate light flux or mass transport flux controlled experiment from which information on the redox reactions may be obtained [39]. The effects of coupling light and redox elements may be circumvented in the two limiting cases dominated by either (a) photon flux, so that

$$i(photo) < i(mass\ transfer)$$

or (b) mass flux where the redox species surface concentration is low, so that

$$i(mass\ transfer) < i(photo).$$

Case (a) prevails in normal PEC cells where the redox species are present at high concentrations. It is generally not possible to distinguish between the surface and solution reactions in this mode without a ring analysis. In semiconductor studies the RDE method is more effectively applied under the condition (b). The level of illumination has to be maintained so that the anodic current (for n-type semiconductors), i(D)L, is due to mass transfer of R and the flux of photogenerated holes is sufficient to realize the condition of $Cs(R) \dashrightarrow 0$. Since only n-type semiconductors are experimentally represented in this work, figure 3 and the following discussion will be limited to this category. The extension to the p-type case involves only attention to reaction directions and sign conventions.

The ring current-ring potential, i(R)-E(R), curve II of Figure 3, has same shape as curve I obtained at the disk electrode. Curves I and II are displaced by the photoelectrochemical cell voltage, E(cell), since the metal ring is essentially measuring the redox potential of the electrolyte. The ratio i(R)/i(D) is constant for a given electrode design and is determined solely by the geometry of the electrode.

$$i(R)/i(D) = [r3/r1-r2/r1]^{2/3} \qquad (5)$$

If reaction 1 occurs at the disk at a potential E(D+), O formed at the disk escapes by diffusion and is transported radially by the convective transport occuring in the hydrodynamic boundary layer adjacent to the rotating disk. Thus the solution normal to the electrode region contains the product of the disk reaction O in addition to O and R from the electrolyte. This region is, however, depleted in the concentration of R because of conversion of some R into O at the disk electrode. The changes in the fluxes of O and R at the ring due to the disk reaction can be monitored by application of a suitable, constant ring potential, E(R), while scanning E(D).

Curve III shows i(R)-E(D) scan with E(R) set at the limiting current potential, E^{+}, of reaction 2. As reaction 2 proceeds at the disk under steady state conditions at E^{-}, a fraction of the flux of R produced is 'collected' at the ring in addition to the flux of R from the electrolyte. The increase in i(R+), $\Delta i(R+)c$, resulting from 'collection' of products of the disk reaction is related to i(D-) by the collection efficiency, N, given by

$$N = n(D)\backslash i(R+)c/n(R)i(D-) \qquad (6)$$

and can be calculated from the geometry of the RRDE [41]. During the anodic photoreaction 1, at the disk electrode, some R is consumed, thus reducing the flux of R reaching the ring and hence i(R+) by $\Delta i(R+)s$. The disk current is related to this decrease, $\Delta i(R+)s$, resulting from the ring being 'shielded' by the disk by equation 7.

$$N = n(D)\backslash i(R+)s/n(R)i(D+) \qquad (7)$$

Comparing curves IV and I, we see that similiar relationships can be derived between i(D-) and the decrease, $\Delta i(R-)s$ due to

'shielding' and between i(D+) and the increase, $\Delta i(R-)c$ from 'collection'. Comparison of the shielding and collection efficiencies for a given disk process, makes it possible to determine precisely how much of an electroactive species is consumed at the disk by faradaic and non faradaic processes.

In addition, comparison of collection and shielding efficiencies for the anodic and cathodic branches of current provides internal calibration for N. This calibration is useful in situations where the geometric N is not easily calculated because of symmetry and concentricity irregularities in the RRDE construction.

2.3. MONITORING OF OXIDATION AND REDUCTION POTENTIALS

Before investigating the electrochemical behavior of a semiconductor in a specific electrolyte the voltammetric characteristics of the redox species in the respective supporting electrolyte have to be established with a noble metal electrode with well defined behavior. Oxidation and reduction potentials have to be determined in order to enable detection of the electroactive solution species generated or consumed by the disk. This is conveniently accomplished by sweeping the platinum ring electrode potential, E(R), in millimolar solutions of the redox species in a supporting electrolyte under steady state conditions. The development of an anodic or cathodic wave reaching a plateau, during an i(R)-E(R) sweep, curve II of Figure 3, is an indication of limiting currents for the oxidation or reduction of the respective species. Rotational speed dependence of this wave distinguishes the mass transport controlled redox reaction from surface or solvent processes and is used as a further confirmation. E(R) for detecting the redox species is generally selected in the flat region of this plateau, where a maximum limiting current is attained and the interference of currents from other reactions is minimal.

3. EXPERIMENTAL

3.1. ELECTROCHEMICAL EXPERIMENTS

SEMICONDUCTOR ELECTRODE PREPARATION: Single crystals of n-$CuInSe_2$ were grown from the melt by the gradient freeze technique [42]. The net carrier concentration was 2×10^{17} cm^2 and the room temperature mobility was 920 cm^2/Vsec. Figure 4 shows an ingot of $CuInSe_2$ with large (112) faces that are characteristic for directional solidification of nearly stoichiometric melts in pyrolytic BN boats. Although the ingot is composed of several large grains of typically 1 cm^3 volume, oriented single crystal bars and wafers can be cut from this material.

p-$CuInSe_2$ and n-GaInAsP were polycrystalline material [43]. The carrier concentration for $CuInSe_2$ was of the order of $\sim 10^{16}$ cm^{-3}. The stoichiommetry of GaInAsP was estimated from X-ray flourescence measurements as $Ga_{0.11}In_{0.89}P_{0.5}As_{0.5}$.

Electrode surfaces of n-$CuInSe_2$ were prepared by either cleaving on (110) or cutting and polishing (112) faces with Linde B powder. Additional polishing with 0.07 microns diamond paste to a shiny smooth finish was used for the efficiency measurements. The p-$CuInSe_2$ and n-GaInPAs electrodes were similiarly prepared. Approximately 1 mm thick slices were back-ohmic contacted with In-Hg eutetic (n-type) or evaporated Au (p-type) and side mounted on Cu wires, brass shafts or bottom mounted on steel shafts for the RDE configuration, with silver epoxy (Scotchcast 3M). Si rubber or insulating epoxy (Scotchcast 3M) were used to encapsulate the crystals mounted on Cu wires and sealed in glass tubes. The other electrodes were encapsulated in Teflon mantles.

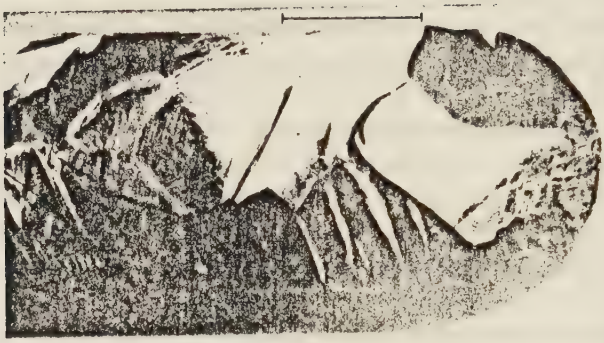

Figure 4. $CuInSe_2$ ingot grown by horizontal gradient freezing. Marker represents 1 cm.

The exposed electrode surfaces were in an etching sequence consisting of 3:1 $HCl:HNO_3$ etch, H_2O rinse, 10% KCN etch and H_2O rinse before immersion into the electrolyte and as required for various experiments.

ROTATING RING-DISK APPARATUS: The RRDE were constructed with demountable disks in order to facilitate disk removal and reuse of the ring assembly. In this construction the center rod is drilled and tapped to a convenient screw size as pictured if Figure 5, following rod tube alignment and insulation. Stainless steel screws with ~ 0.5cm diameter head machined flat serve as convenient disk mounts. Ohmic contacted $CuInSe_2$ crystals of slightly larger diameter were mounted on these screws with silver epoxy and shaped into disks on a mini-drill with an abrasive paper.

The disk was treated to approximate planarity to the ring. The gap between the ring and the disk was filled with epoxy soluble in most organic solvents. Coplanarity was achieved by mechanical polishing. Regular polishing of the electrode with 0.3 micron Allumina between experiments was necessary to eliminate the anomalous residual currents on the platinum ring, resulting from adsorbtion of halides and other ions, and to ensure surface reproducibility. Chemical etching in 3:1,$HCl:HNO_3$ was used to renew the $CuInSe_2$ disk surface.

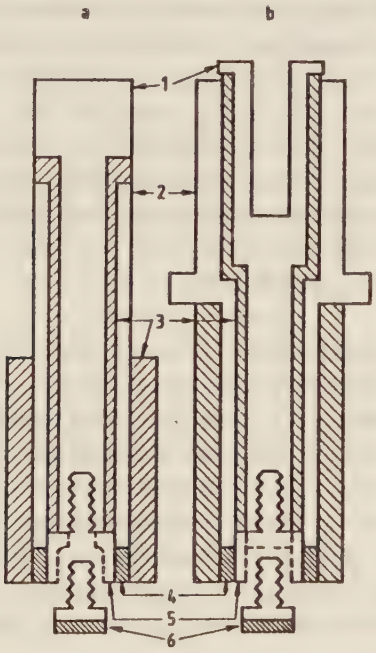

1) DISK CONTACT
2) RING CONTACT
3) INSULATION
4) RING
5) GAP TO FILL
6) DISK

Figure 5. Schematic diagram of demountable disk, ring-disk electrodes.

Current voltage curves were obtained with a Pine Instruments RD3 dual potentiostat and a Philips XYY' recorder. An MSR rotator from Pine Instruments Company or a PI-Regler SR374 Model from Jaissle Electronic Labor was used to drive the RRDE. Schematics of the RRDE assemblies constructed to adapt to these rotators are illustrated in Fig. 5a and b. The dimensions of the disk and ring were approximately the same for the two assemblies. Platinum was used as ring material.

ELECTROLYTE: Reagent grade chemicals and distilled water were used to prepare solutions. The electrolyte comprised 1M CaI_2, 50 mM I_2, 20 mM CuI and 2.5 M HI for the initial solar cell and 1M CaI_2, 50 mM I_2, sat.CuI and 4M HI for the improved version. Redox potentials for the two solutions were 0.16 $\pm$ 0.02 V and 0.20 $\pm$ 0.02 V respectively. Electrolyte compositions for the other experiments are specified in the respective sections. A steady flow of nitrogen was maitained in the cell during most experiments.

CELL AND ILLUMINATION: Conventional electrochemical cells fitted with fritted compartments for reference electrode and nitrogen bubbling and a were used for measurements in the concentrated electrolyte and side mounted electrodes. The cell was illuminated through a vertically mounted optical flat on one side of the cell. A three compartment cell with a bottom optical flat in the centre compartment was used for the rotating ring-disk experiments. Spectroscopic grade carbon rods served as counter electrodes and saturated calomel electrodes (SCE) as reference.

For measurement of cell efficiency, illumination was provided by natural sunlight or by an 81101 Oriel Solar Simulator. The latter was calibrated with a Pyroelectric PK 5000 Radiometer to deliver AM1 intensities. All other photoelectrochemical experiments were performed under tungsten-halogen (Oriel) irradiation.

A 250 W Oriel lamp and a Kratos grating monochromator comprised the spectral source. Photocurrent was synchronously detected with a PAR lock-in amplifier and processed with a computer.

3.2. SURFACE ANALYSIS

SAMPLE PREPARATION: Electrodes treated in electrochemical experiments were dismantled mechanically and the crystals transfered to the respective chambers for analysis. For XRD and UPS measurements films were grown by suspending $CuInSe_2$ wafers partially immersed in the electrolyte.

SCANNING ELECTRON MICROSCOPY (SEM) AND X-RAY FLUORESCENCE (XRF): Back contacted samples were mounted in a vacuum chamber of an SEM system, JSM-35 (JEOL) evacuated to ~1 x 10^{-5} torr. The beam voltage was 20 kV. The spacial resolution was ~100 A^{o}. The XRF spectra were analyzed with a 'Link' computer system.

X-RAY AND UV PHOTOELECTRON SPECTROSCOPIES (XPS, UPS): XPS measurements were performed in a Kratos ES 300 electron spectrometer using non-monochromatized Mg(Ka) X-rays for determining binding energies. The Au $4f_{7/2}$ line served as reference. The base pressure in the spectrometer sample chamber was 2 x 10^{-10}. An Argon ion beam of E = 4 keV was used to sputter the samples at a rate of ~20 A^{o}/min. A UV source of He II ions was attached to this system for the UPS measurements.

X-RAY DIFFRACTION (XRD): X-ray diffraction analysis was performed with a Guinier thin film camera. Incident angle of the X-ray beam was 2^{o} (grazing incidence). The spectrum was recorded using CuK(a) radiation and was not corrected for the air scattering component.

MICROWAVE CONDUCTIVITY: Surface microwave conductivity measurements were performed in air. Principles and circuitry of the method are described elsewhere [44]. Excitation was provided by a frequency doubled Nd-YAG laser at wavelength of 530 nm or 1060 nm with a 20 3ns pulse. Microwaves of 30 GHz frequency were directed perpendicular to the semiconductor surface. Light induced conductivity changes were detected by analyzing the relative changes in the reflected microwaves.

4. FILMS AND THEIR IMPACT ON CHARGE/MASS TRANSPORT

4.1. TYPES OF INTERFACIAL FILMS AT SEMICONDUCTOR ELECTRODES

Films, inadverdently present or deliberately inserted at the semiconductor-electrolyte interface, can intervene in the corrosion process by removing the photoactive junction from chemical attack by the electrolyte. Interfacial films may be deposited externally or grown in-situ as described above.

Deposited foreign films include noble metals [20.21], conducting oxides [22], inert macromolecular layers [23] and charge transfer bridge molecules [24,25]. In addition to the extra steps involved in deposition of these films, their chemical and physical incompatibility with either or both the substrate semiconductor and the electrolyte, poses problems and limits their utility in PEC cells.

In-situ grown films involving corrosion products would be expected to be more stable in their native electrolytic environment and physically adapted to the substrate (lattice matching) and to allow further manipulation of their properties. Metal films can be deposited in-situ by reduction of the cations of compound semiconductors. Reduced metallic films of most compound semiconductors are of low transparency, usually dissolve or oxidize at relatively low potentials and are therefore, unsuitable in systems involving photoanodes. Semiconducting or insulating films include elemental or compound semiconductors, the latter usually in the form of oxides. Current transport through the film can proceed by more than one mechanism. The prevalent mode is determined by the conductivity, thickness and

structure of the film. Tunneling of carriers directly through the film is expected to be the dominant transport mechanism in thin films. Transport of carriers through the conduction or valence band is expected for semiconductive films. Insulating films normally passivate the surface and if they are thick, the applied voltage can drop partly across the film instead of across the barrier. The holes will then be consumed by simple recombination at the interface states. Current transport through insulating films depends on their defect structure and on the presence of mobile ions in the film.

4.2. ELECTROLYTE-INSULATOR-SEMICONDUCTOR(EIS) AND ELECTROLYTE-METAL-INSULATOR-SEMICONDUCTOR(EMIS) STRUCTURES

The beneficial effects of interfacial transition layers at junctions between metals, semiconductors and liquids such layers in reducing interface state density and modifying the barrier have been recognized and utilised in the construction of MIS and SIS devices [45,46]. When interposed at the semiconductor/electrolyte interface, the insulating films can serve an additional function of protecting the semiconductor from photocorrosion. The film is required to have a fairly large band gap and tunneling thickness so that the wavefunction of charge carriers can penetrate across the interfacial layer, resulting in current flow. Two versions of EIS structures are schematically depicted in figure 6, the electrolyte (a) replaces or (b) is added to the metal, in MIS structures. A counter electrode completes the cell.

The EIS structure (a) is modelled by a p-InP/film/V(II)-V(III)-HCl/C cell [29]. A patchy native oxide of ~4 A° thick is found on InP [47]. The I-V curves in figure 7 show the behavior and the optimization of this oxide layer. For curve I_1 obtained in an acidic supporting electrolyte, three characteristic potential regions may be distinguished.

(A) Cathodic reduction and associated oxidation(peak), (B) region of low cathodic currents indicative of formation of a thin film which inhibits semiconductor corrosion and (C) anodic activity due to breakdown of the protective film. The current associated with the anodic peak at 0 V, has been identified with a rotating ring-disk electrode as partially comprising of dissolution of In, which deposits during the cathodic reduction [26]. With the addition of V(II)-V(III) couple, the photocurrent onset in curve II shifts positive, thus locating the operational range (maximum power point) of the cell in the region B of curve I. Curve II, however, represents the behavior of the electrode after the oxide film has been electrochemically conditioned by cyclic polarization in the potential regime B of curve I. The initial output of an etched, air exposed electrode covered with the native oxide resembles curve III. In addition to a lower open circuit potential, Voc, and fill factor, FF, this curve exhibits considerable hystheresis between the forward and the reverse traces.

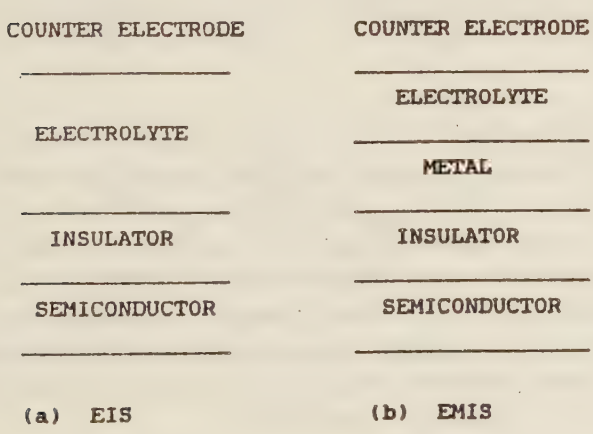

Figure 6. Schematic diagram of EIS and EMIS cell structures.

In MIS or SIS structures native oxides on InP have been found to be inadequate compared to the deposited dielectrics [48]. Cyclic reduction and growth of the film in the region of the thin oxide formation evidently helps to eliminate defects and voids yielding a compact film which hinders ion transport, and thus further growth, and remains thin enough to conduct by tunnelling. That the film thickness is a critical parameter is demonstrated by the deterioration in the FF and Voc, curve III, also observed either by reduction of the oxide film in the region A or on further oxidation in the region C. Slow thickening in the region C eventually suppresses current flow.

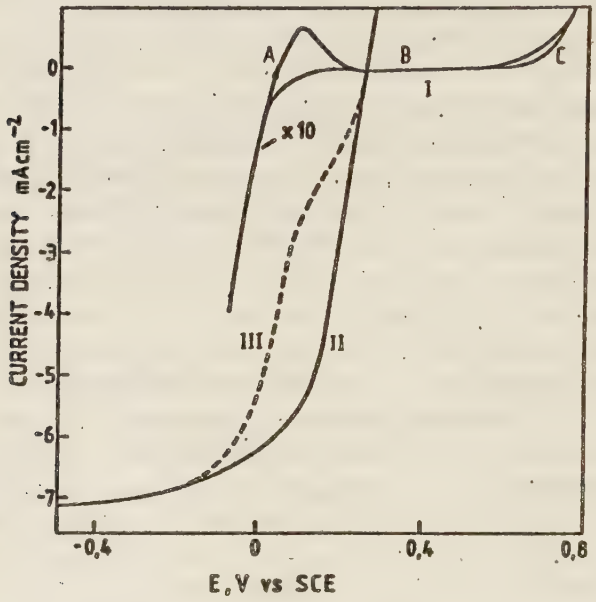

Figure 7. Current-voltage characteristics of illuminated p-InP(111), showing potential regions of (A) film reduction, (B) thin film formation and (C) film thickening in 1M HCl; II, with optimized film; and III, with etched, reduced or oxidized film in V(II)-V(III)-HCl.

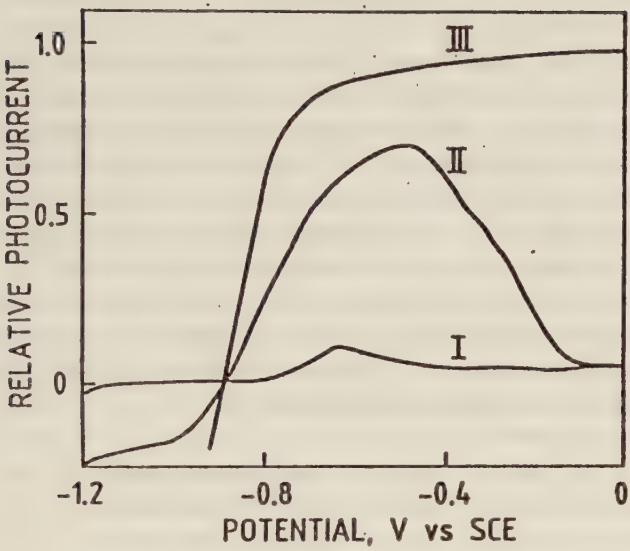

Figure 8. Current-voltage curves at illuminated n-GaAs showing I (A)reduction, (B)passivation and (C)oxidation regimes in acetate buffer, pH 5; II photooxidation of Fe(II) with concurrent passivation at pH 5; III photooxidation of $Fe(CN)_6^{-4}$ at Au plated n-GaAs.

The EMIS structure in figure 6b is modelled by a n-GaAs/oxide/Au/Fe(II)-Fe(III)cyano-acetate buffer/C cell. GaAs oxides are insoluble only in electrolytes of intermediate pH and film formation in strong acids or bases is not possible [28,49,50]. Formation and behavior of an oxide film on GaAs at pH 5 is shown in curve I of figure 8. As seen for InP in figure 7, curve I exhibits three characteristic regions A(without the peak), B and

occurs at much lower current densities. The photocurrent seen in curve II indicates that in the initial stages of growth, regions A and B, the film is sufficiently thin to support efficient photooxidation of Fe(II). Mass transport controlled oxidation of Fe(II) in this system was detected by rotating ring disk electrode [28]. Thickening of the film in the region C or with time leads to virtual cessation of all reactions at the electrode. Film thickening can be inhibited if an inert metal film is interposed between the oxide and the electrolyte to generate the hybrid structure EMIS. Photooxidation of $Fe(CN)^{-4}$ at a Au plated GaAs eletrode is shown by curve III. No passive transitions are observed indicating that the metal film is effective in preventing oxide thickening. The current is controlled by the photon flux penetrating the three layers of electrolyte, metal and oxide on GaAs.

Stability tests with this system showed no deterioration in Isc for passage of 3000 Coulombs cm^{-2}, when the electrolyte (which photodegrades) was periodically renewed [21]. Thicker metal films improve stability but at the cost of substantial reduction in the photocurrent. Photopotentials in GaAs based EMIS cells are a function of the semiconductor-metal pairing and relatively independent of the redox couple as is the case with metallized GaP and Si electrodes [20].

These results on EIS structures based on InP and GaAs evidence that film formation leading to current flow inhibition and its growth and breakdown, is often the determining factor in the utility of these semiconductors in PEC cells. Thus before pairing semiconductors with redox couple it is essential to understand the dissolution/passivation characteristics of the semiconductors particularly the influence of pH of supporting electrolytes.

4.3. EFFECTS OF ELECTROLYTE pH ON FORMATION AND DISSOLUTION OF INTERFACIAL FILMS ON III-V SEMICONDUCTORS

Since film formation is central in EIS structures, substantial pH effects are anticipated. In acidic electrolytes III-V binaries (III = Ga, In and V = P, As, Sb) exhibit a range of interfacial behavior [26]. The probability of film formation and the nature of the film, depend on chemical components of the semiconductor, the potential of electrode operation and the pH of the electrolyte. Under controlled potential cycling these semiconductors exhibit the three characteristic regions as seen in figures 7 and 8 for InP and GaAs. The degrees of definition of the three potential regions vary with pH for a given semiconductor. All III-V compounds investigated, exhibit considerable passivity in solutions of intermediate pH. In acids and bases the passivation behavior varies for the different compounds with InP and GaAs ranking at the opposite extremes of the series.

Dissolution of InP on anodization is severely inhibited even in aggressive acidic medium by the formation of a coherent film removable only by extensive cathodic reduction. GaP, InSb and GaSb passivate less readily forming solubility limited precipitates on the surface at high current densities. Films do not play a role in the anodic reactions of GaAs in acids and bases. Passivation of InAs and GaAs is virtually unreacheable except at extremes of current densities, with films being quite porous and permitting considerable surface corrosion.

4.4. SURFACE FILMS ON GaInPAs

Ternary and quarternary semiconductors allow additional degrees of freedom in the selection of band gap and lattice constants to give optimal junction properties. The gradation of properties observed for the III-V binary series between InP and GaAs endpoints suggest that both group members are involved in the film formation. It is thus of interest to examine the passivation properties of a solid solution of the two extreme members of the binary series. The I-V behavior of GaInPAs is examined under the controlled hydrodynamics of the rotating disk electrode in the regions of open circuit potential, at the more positive potentials where the film may breakdown and regrow, and at the more negative potentials, where the film may be reduced. In the more promissing cases, where the film could hinder mass transfer while allowing charge transfer, possibilities of charge transfer to solution species are explored.

4.4.1 BEHAVIOR IN SUPPORTING ELECTROLYTES

Figure 9 shows the behavior of n-GaInAsP in acidic, neutral and basic solutions. I-V characteristics in the light and dark are shown by dashed and solid lines. The three representative potential regimes, discussed above, are denoted by A, B, and C.

At pH 0, the separation of the regions A, B and C in the I-V curve I resembles that observed for InP, figure 7. The anodic peak at -0.7 V is observed only when the electrode is reduced at E < -1.5 V. A similiar peak, seen for In compounds in the binary series, was identified as mainly dissolution of In layers deposited during the cathodic reduction [26]. The presence of a passive region B over a wide potential region

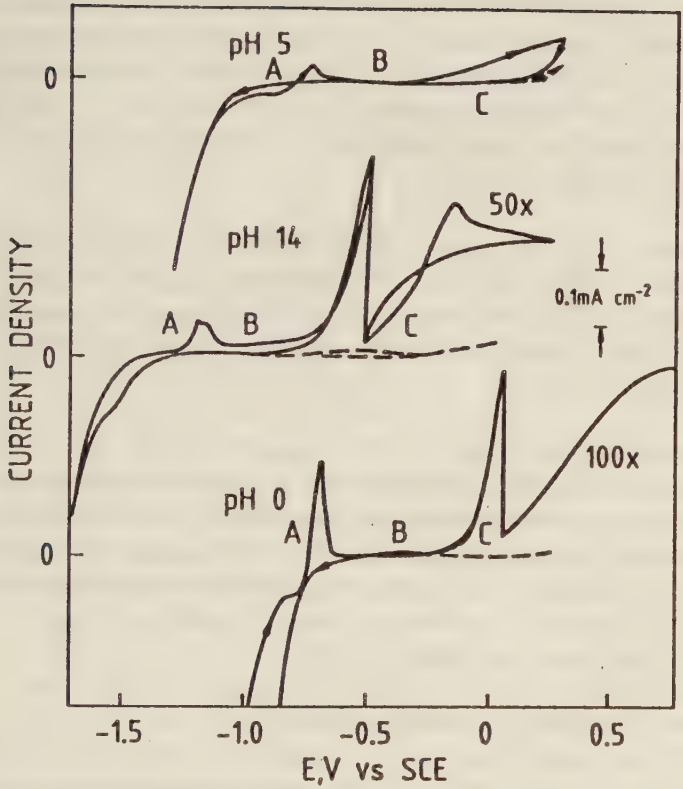

Figure 9. Current-voltage curves at illuminated (solid) and dark (dashed) n-GaInPAs in (I) 1M HCl, (II) 1M NaOH and (III) acetate buffer. Potential regimes, as in figure 7, are designated by letters A, B and C.

suggest that the InP characteristics predominate. The I-V curve of GaAs shows a transition directly from the region A to the region C without the intermediary region B. The GaAs characteristics , however, are more prevalent in the transpassive region C. Filming in this region is not observed at the current levels shown in the figure. At these currents, InP passivates forming thick, current blocking films whereas GaAs attains transpassive behavior only at currents > 1 A/cm^2. A similiar transition could probably be reached for GaInAsP at much higher illumination levels.

Curve II shows a transition peak and a passive region B, representative of InP. The transpassive currents in the region C are higher than those of InP by an order of magnitude reflecting the greater tendency towards dissolution due to the Ga and As content.

Curve III obtained at pH 5 exemplifies the behavior of most III-V semiconductors in neutral and complexing solutions. The curve shows extensive surface passivation following the transition(peak) A. The transition between regions (B) and (C) is not distinguishable in neutral solutions. Photoeffects are negligible in region C indicating that the passive film severely blocks mass and charge transport.

4.4.2 REDOX REACTIONS IN ACIDS AND BASES

Although the surface electrochemistry of GaInAsP resembles that of InP, the behavior in the presence of redox couples approaches that of GaAs. Curves I and II in figure 9 suggest that the films formed in the region B may be sufficiently passive to prevent further growth and sufficiently thin to sustain a redox reaction as in the case of InP at pH 0(EIS). These possibibilities are investigated in several redox electrolytes at pH 0 and 14.

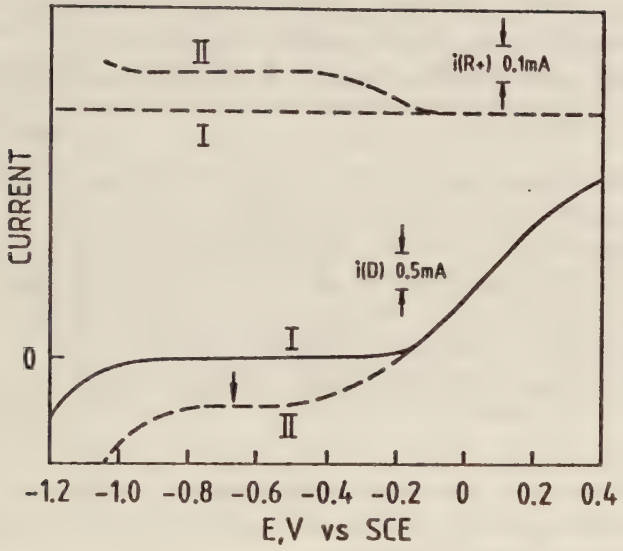

Figure 10. Disk and ring currents, i(D), i(R) during a potential scan at an illuminated n-GaInAsP RRDE electrode in (I) 1M HCl and (II) 0.1M Fe(II)-Fe(III) 1M HCl. Effect of light blocking is shown by dotted lines.

pH 0: Addition of Fe(II)/Fe(III) redox couple does not alter the anodic characteristics of curve I , figure 9; specifically, no negative shift in the onset potential of the photocurrent is observed. This result, however does not rule out the possibility that the photoxidation of Fe(II) and photocorrosion process of curve I, figure 9, occur simultaneously. This ambiguity was clarified with a GaInAsP rotating disk-Pt ring electrode shown in figure 10. The ring set to monitor the Fe(III) ions, does not detect any changes in the flux of these species during the anodic photoprocesses at the disk indicating that these processes do not involve generation of

Fe(III). The ring, however, detects the cathodic reduction of Fe(III), also evidenced by the development of a cathodic wave in the disk curve. Similiar behavior was observed with the I^-/I_2 couple at pH 0. These results are consistent with the behavior of GaAs in the same solutions [26].

pH 14: GaInAsP passivates readily at potentials positive of the peak(A) in curve II, figure 9, even with redox couples present. Although charge transfer to the polysulfide species is initially possible, the photocurrent decreases as the film grows with time. Highly reducing solutions such as polyselenide at pH 14 appears to be better able to sustain redox reactions over longer periods but the stability is inferior to that of GaAs [8].

Neutral solutions are clearly unsuitable for redox processes. The high degree of passivity blocks charge transport almost completely, unless a metal film intervenes to prevent film thickening as in the GaAs EMIS structure.

Films do not seem to play a significant role in the surface reactions of GaInPAs in acids. In bases and neutral solutions, the films are either too porous to prevent mass transfer or too thick to allow charge transfer. The electrochemical characteristics are consistent with the prior observations of InP and GaAs [26,28]. While InP tends to induce film formation, the As content enhances its dissolution. By combining appropriate fractions of In, P, Ga and As it may be possible to taylor the interfacial films to incorporate dissolution/passivation properties of both members.

These results illustrate the role of electrolyte pH and the impact of interfacial films in hindering or fostering charge or ion transport. Electrolyte pH and electrode potential determine the nature of the interfacial process. Differences in

the behavior of the III-V and I-III-VI compounds indicate that semiconductor components play a definite role in controlling the film properties. A high hydrogen ion activity appears to be essential to maintain tunnelling thickness in these films. Films formed in basic and neutral solutions can stabilize the semiconductor against corrosion and may be initially thin enough to sustain a redox reaction. Film thickness increases as a function of time and potential and eventually inhibit both corrosion and redox reaction. For maximum efficiency and stability, the operation of the electrode must be confined to the region B, where the film formed is adequately protective and permits unhindered charge transfer. It is thus imperative to avoid region A where the films tend to reduce and region C where the films may be too thick to permit transfer of charge carriers.

5. INTERFACIAL ELECTROCHEMISTRY OF $CuInSe_2$

Attempts at constructing PEC cells with the ternary chalcopyrites [33,34], have not yielded cell peformances comparable to the existing benchmarks [9,15] although their stability was notable. Low conversion efficiencies, in these systems have been attributed to the poor kinetics of the S dissolution step. Simultaneous optimization of stability and efficiency requires detailed knowledge of the interfacial processes in various media. The influence of pH, illumination and applied potential on the voltammetric characteristics of n- and p-$CuInSe_2$ is shown in figures 11-13 in three representative electrolytes.

5.1 SURFACE REACTIONS of n- and p-$CuInSe_2$ IN REPRESENTATIVE ELECTROLYTES

pH 0: The behavior in HCl is shown in figure 11. The illuminated curves for the two conductivity type semiconductors are quite similiar exhibiting the three characteristic potential regimes seen for the III-V compounds. No anodic (In dissolution) peak is seen in region A. Instead oxidation and reduction peaks appear in region B. The magnitude of these peaks and the hystheresis in the region B diminishes on repeated cycling between a potential span of -0.8 V and 0.3 V for the n-type and of -0.5 V and 0.6 V for the p-type semiconductor. This may be interpreted as semiconductor passivation. The shifts of scale and the dark behavior is consistent for the two charge types. Breakdown in passivity in the region C results in a photocurrent for the n-type crystal and forward current for the p-type. The current may result from either semiconductor dissolution, formation of a new phase or

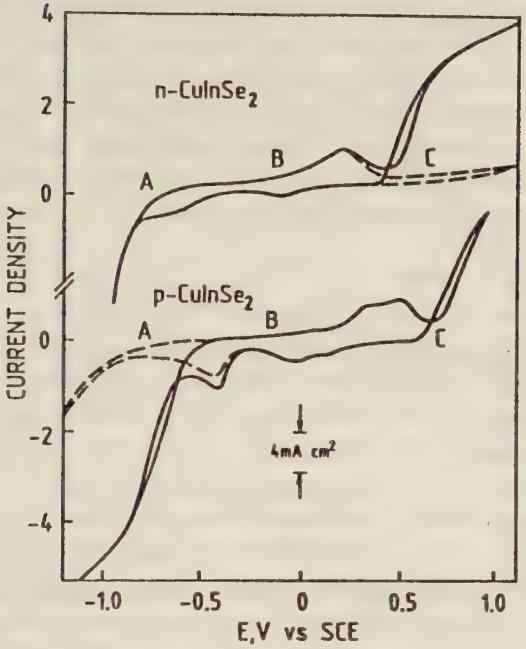

Figure 11. Current-voltage behavior of n- and p-$CuInSe_2$ in 1M HCl. Illuminated (solid curves) and dark (dashed curves).

from solution oxidation. At the current levels shown in figure 11 anodic etching of $CuInSe_2$ proceeds at high rates at potentials positive enough to cause an oxidative breakdown of the passive film. Evidence of the formation of an insoluble phase is seen by the increased structure in the region B after extensive anodization. Absence of a peak in the region A argues that the cathodic reduction does not deposit In layers as in the case of the III-V In compounds. Thus reductive decomposition of $CuInSe_2$ appears more difficult and the current in the region C is mainly H^+ reduction.

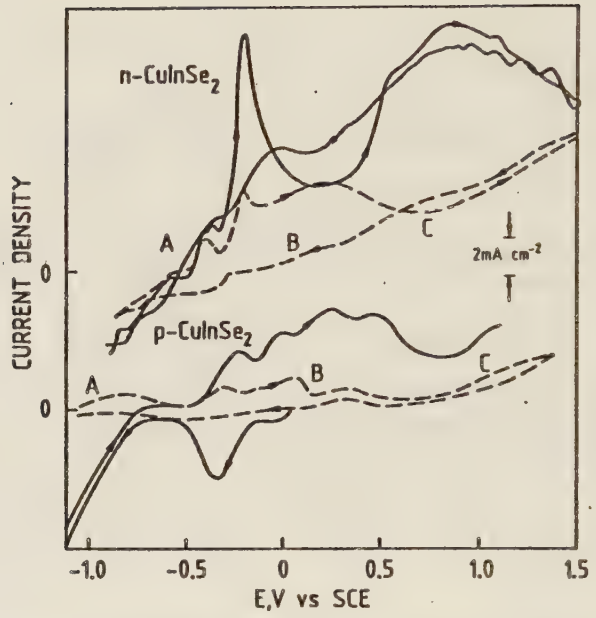

Figure 12. Experiment of figure 11 in 1M NaOH.

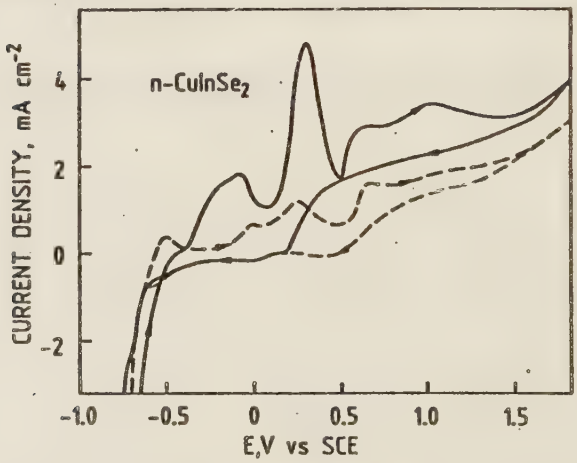

Figure 13. Experiment of figure 11 in acetate buffer for $n\text{-}CuInSe_2$.

pH 14: Figure 12 shows the behavior of $CuInSe_2$ in alkaline solutions. The solid lines show the initial curves under illumination. For both conductivity types the curves show several anodic transitions. Photocurrents are observed in the region A (cathodic) for p-type and in the region C (anodic) for n-type. Cycling between the potential limits shown in the figure decreases both anodic and cathodic currents. Both n- and p-$CuInSe_2$ electrodes loose their photosensitvity and the I-V behavior in the light and dark is given by the dashed curves.

pH 5: Figure 13 shows the I-V characteristics in acetate buffer for n-$CuInSe_2$. The characteristics are similiar to those in figure 12 for both conductivity types. The peak heights and the hystheresis continue to decline on repeated cycling. As with III-V semiconductors, photoactivity is negligible in this media.

The voltammetric behavior in neutral and basic solutions is quite different from that observed in acid. Instead of the sharp passive active transition between regions B and C, seen in figure 11, several transitions are observed in figures 12 and 13. These transitions indicate semipassive behavior but no film breakdown and surface reactivation. The high initial currents suggest that the films are porous allowing ion transport. They continue to grow thick and passivate the surface. The loss of photoactivity indicates that they are poor electronic conductors and therefore unsuitable for regenerative PEC cells.

5.2 BEHAVIOR IN ALKALINE POLYSULFIDE

The low efficiency of $CuInS_2$ and $CuInSe_2$ in polysulfide solutions has been attributed to the sluggish kinetics of the redox couple, dissolution of sulfur being the rate limiting step [33,34]. Other semiconductors, such as CdS, CdSe or GaAs do not show nearly as low FF and poor behavior at the foot of the I-V curve in polychalcogenide solutions, where the same step should be limiting, as in curve I of figure 14 for $CuInSe_2$. From figure

12 we can infer that that the interfacial phase of $CuInSe_2$ at pH 14 might have larger contributions to the poor kinetics. The higher porosity of this film in alkaline media probably allows it to grow thicker than it does in acids. Loss of cathodic photoactivity for the p-type and anodic photoactivity for the n-type in regions A and C of figure 12, respectively, indicate that the film strongly resists both anodic dissolution and cathodic reduction. On the other hand, films in acids allow uninhibited current flow at either ends of the passive region B.

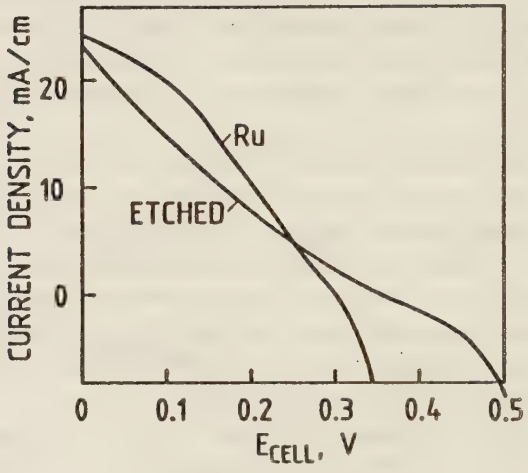

Figure 14. Current-voltage curves of illuminated n-$CuInSe_2$ in S_x^{2-}/S^{2-}/NaOH. I, etched and II, dipped in $RuCl_3$.

The redox potential of the polysulfide solution appears not sufficiently negative to move the potential span of operation of the cell outside the passive region. the effect of dipping $CuInSe_2$ in Ru(III) solutions is seen as an improvement in curve II, figure 14. This improvement is evidenced primarily by steeper cathodic currents. The catalytic action of Ru for H+ reduction might assist in partially reactivating the electrode surface and thus improve interfacial kinetics at the foot of the curve. Unlike the GaAs/polyselenide cell [9] the Ru effect is transitory again illustrating the dominant role of films on $CuInSe_2$.

Figure 14 suggests that similar interface kinetics could dominate in solutions of intermediate pH, where passivation of $CuInSe_2$ is even larger than at pH 14. Its behavior in acids, figure 11, appears more favorable. From the distinct active/passive/active transitions in the three regions, we may infer that the interfacial film formed in the region B is impervious to ion transport and therefore resists growth. Growth occurs in region C due to electrical breakdown caused by increasing electrical field. Similiarly, increased electrical field reduces the film in region A. In addition, the potential limits of the passive regime B do not increase with repeated cycles or time as observed at pH 5 and 14. This film could thus conduct by tunneling, if the electrode operation is confined to the regime B.

5.3. VOLTAMMETRY OF $CuInSe_2$ IN NEUTRAL AND ACIDIC IODINE/IODIDE

Photocurrent-voltage curves for n-$CuInSe_2$ in (1) 1M HCl, (2) I^-/I_2 redox couple and (3) I^-/I_2 + HI, compiled in figure 15 provide intercomparison and illustrate potential shifts. Passive region of curve 1 is located between -0.7 V and +0.4 V versus SCE. Breakdown of the passivity results in photocurrents at potentials $>$ 0.4 V vs SCE. A negative shift in the photocurrent onset potential of ~0.16 V is observed in the I^-/I_2 solution

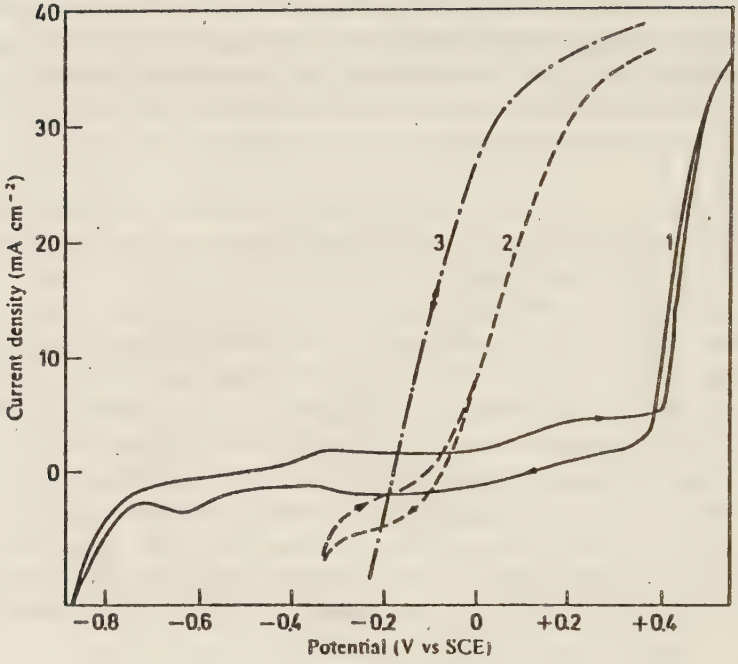

Figure 15. Comparison of current-voltage characteristics of illuminated n-$CuInSe_2$ in (1) 1M HCl; (2) 1M CaI_2 + 0.05M I_2; (3) 1M HI added to solution (2).

(curve 2), which locates the maximum power point in the passive region of curve 1. From the potential shift and the color change observed visually at the electrode surface during the anodic reaction, the photocurrent is infered as resulting from oxidation of iodide. Low fill factor and poor behavior at the foot of the curve characterizing curve 2 indicate that passivation dominates the surface kinetics as expected in solutions of intermediate pH from figure 13. Anodic and cathodic slopes of curve 2 imply that photooxidation proceeds reasonably fast while reduction of I_2 is inhibited by a film formation process. Addition of HI, curve 3, shows a dramatic improvement in fill factor, open circuit voltage and short circuit current as well as steeper cathodic slopes. These improved characteristics are, however, transitory. Long term stability tests, with the electrode held at the maximum power point under AM1 illumination, indicate surface deterioration, manifested in a gradual decrease of the current output and altered surface morphology. Visual inspection of the electrode surface showed a crusty deposit.

The behavior of $CuInSe_2$ in the polysulfide and the polyiodide systems is quite different. The semiconductor is quite stable in polysulfide but the efficiency is low. Reverse behavior prevails in the polyiodide system. From comparison of the two systems, it appears that simultaneous optimization of the two key parameters of PEC cells, efficiency and stability is difficult. Stabilisation via insulating oxide formation, as in the InP case appears to be not feasible. We know from the survey of electrochemical properties of III-V semiconductors that the formation and the type of films formed are dependent on both the cationic and anionic components of the semiconducting compounds [26]. Substitution of P with As or Sb greatly alters the passivation properties of In compounds. Interfacial chemistry of $CuInSe_2$ involving Cu and Se ions in addition to In, is also expected to be quite different from InP.

6. PARTLY SOLUBLE INTERPHASE

Understanding interactions of $CuInSe_2$ with the electrolyte species and the factors governing these interactions in the interfacial region is crucial to devising stabilisation schemes. Figure 15 implies that these interactions may include several concurrent processes involving film formation, substrate dissolution and photooxidation of iodide. the role of electrolyte constituents, concentration, pH, illumination on the charge transfer and surface reactions have to be systematically examined.

6.1 VOLTAMMETRY OF $CuInSe_2$ IN IODINE/IODIDE

The analytical capabilities of the rotating ring disk electrode are used to unravel the interfacial processes at the $CuInSe_2$ in the polyiodide system. The variables include rotation speed, illumination, iodide concentration and solution pH.

6.1.1 CHARACTERISTICS OF I^-/I_2 COUPLE

The voltammetric behavior of iodide and iodine has been widely investigated [51]. A complication exists in the detection of iodide or iodine involving the adsorption and desorption of these species at platinum electrodes. The reaction mechanism and reversibility vary with pH, the relative concentrations of iodide, iodine and the supporting electrolyte,the presence of complexing agents and the electrode material (Pt, C, Hg). In the case of Pt electrodes, the adsorption of iodine/iodide as well as the formation of platinum oxide alters the electrode surface characteristics and the kinetics of the iodide oxidation reaction [52, 53].

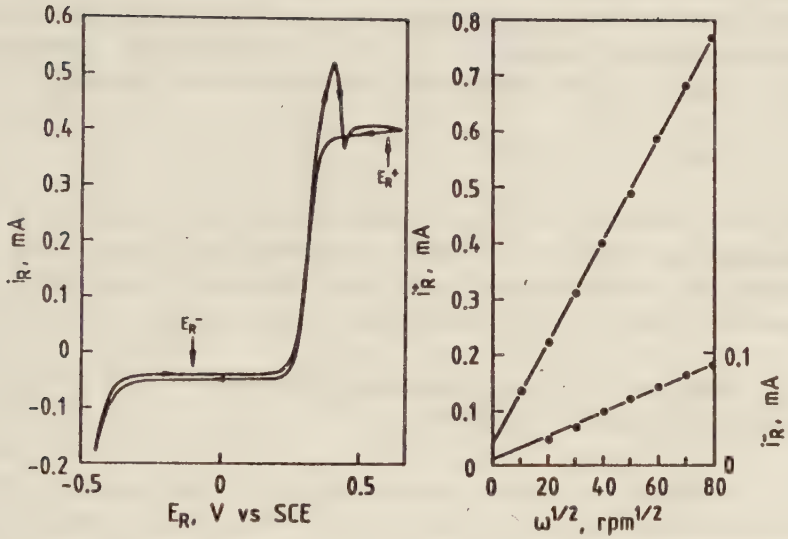

Figure 16. (a) Platinum ring potential scan at 2 mV/sec in 2mM I^- + 0.2 mM I_2 + 1M H_2SO_4 at 1600 rpm to determine E(R+) and E(R-). (b) Ring currents at E(R+) = 0.6 V and E(R-) = -0.1 V vs SCE as a function of rotation speed.

Figure 16a shows i(R) - E(R) curve at the Pt ring electrode in 1M H_2SO_4 containing 2mM I^- + 0.2mM I_2 at a rotation speed of 1600 rpm. The anodic current rises to a peak and levels off to a limiting current plateau. The anodic peak resulting from iodine film formation on Pt is observed only under steady state conditions,i.e. scan rate < 0.1 V/min. At more positive potentials and on the reverse trace the limiting current is proportional to the square root of the rotation speed,

$w^{1/2}$, as predicted by the Levich equation 6 for a convective-diffusion limited process. The linearity of the Levich plot, shown by curve I in figure 16b, and the magnitude of the limiting current compared to the value expected from equation 5, confirm that the wave represents the oxidation of iodide,

$$2I^- \text{ (--> } I_2 + 2e \qquad (8)$$

The ring potential, E(R+), selected to monitor I^- flux is indicated on the curve. Similiar considerations were used to locate E(R-) on the cathodic I_2 reduction wave, the reverse reaction 8, which also exhibits Levich behavior, curve II.

6.1.2 BEHAVIOR OF $CuInSe_2$ IN CONCENTRATED(1M) IODIDE UNDER PHOTON FLUX CONTROL

Figure 17 compares disk currents, i(D0), i(D1), i(D2), i(D3) and ring currents, i(R0), i(R1), i(R2), i(R3), during disk potential sweep cycles for n-$CuInSe_2$-Pt RRDE in 1M HCl and 1M CaI_2 under photon flux limited conditions. The ring potential, ER- is fixed at -0.4V vs SCE to monitor I_2 flux at mass transfer limited rates.

The i(D0) and i(R0) traces in 1M HCl were obtained in order to ascertain that the background currents from oxidation of the semiconductor or the solvent do not interfere with the detection of I_2 at the ring, in the potential range of the subsequent experiments in the iodide solutions. i(R0) is negligible at E(D) < 0.5V. Beyond this potential i(R0) increases gradually to ~0.1 mA at 1V, from detecting the products of the photocorrosion reaction at the disk.

The onset potential of the photocurrent and the shapes of the i(D0) and i(D1) curves in the two solutions resemble curves 1 and 2 of figure 15 respectively. The sluggish charge transfer

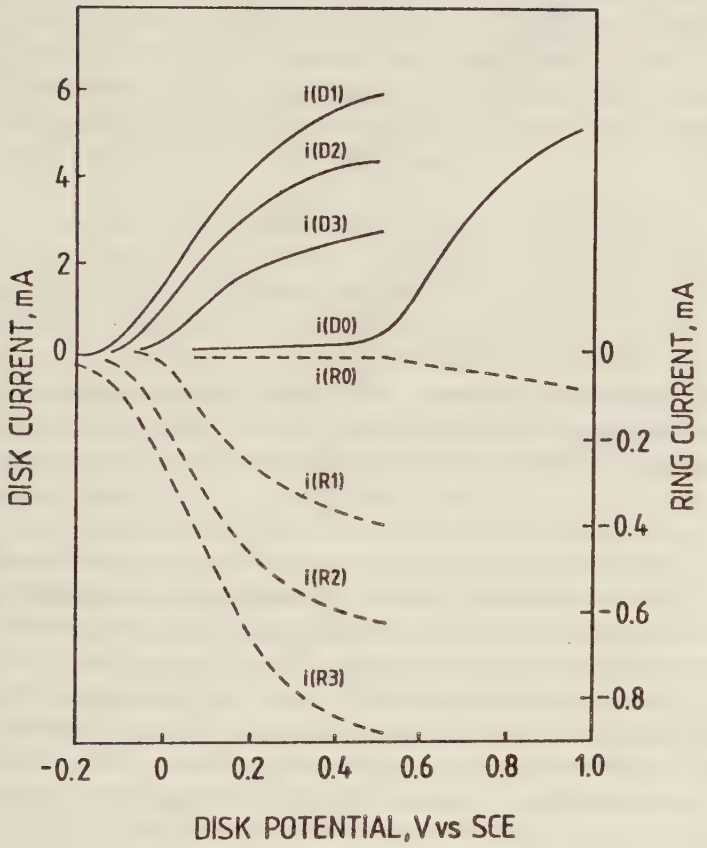

Figure 17. $CuInSe_2$ disk current (solid curves) and Pt ring current (dashed curves) response to decreasing light intensity in 1M iodide solution. E(R) = -0.4 V vs SCE. Rotation speed = 1600 rpm.

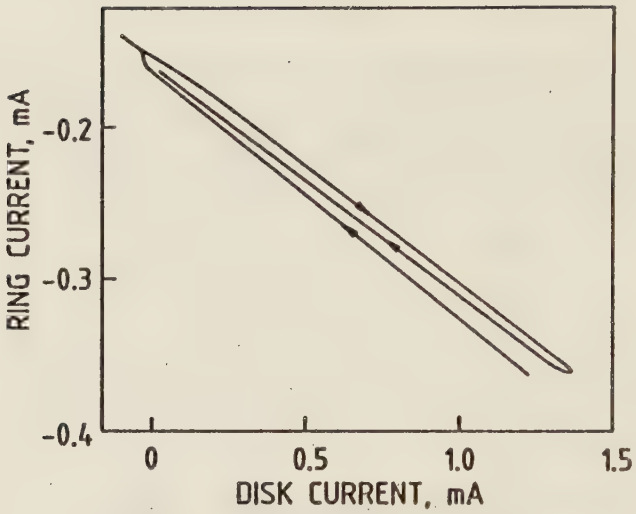

Figure 18. Ring current plotted vs disk current for illuminated $CuInSe_2$ disk-Pt ring in 1M iodide solution. Arrows indicate scan direction. E(R) = -0.4 V vs SCE. w = 1600 rpm.

kinetics and the nearly passive behavior at the foot of curve 2, figure 15, prevail in curve i(D1). The absence of a cathodic wave in curve i(D1) reflects the absence of iodine in solution. This is also indicated by the very low initial level for i(R1) when i(D1) is zero. The subsequent rise in i(R1) parellels the onset and the rise in the disk photocurrent, i(D1) and reaches a plateau as iD1 becomes limited by the photon flux. If the light intensity is decreased i(D) decreases to i(D2) and i(D3) levels and to zero when the light is completely interrupted. Corresponding reduction is observed in i(R1) to i(R2), i(R3) and ~zero level. This indicates that the ring current originates from collection and reduction of the photooxidised soluble products of the disk reaction.

Quantitative determination of the collection properties is provided by a plot of i(D) vs i(R) (for reaction 8) during an E(D) cycle under illumination, shown in figure 18. For

quantitative collection the plot should be linear and yield a slope equal to N(0.18). Less than the theoretically expected value, of N = 0.15 suggests that the charge transfer to iodide (reaction 8) may be dominant but not the exclusive path available to the photoholes or that a fraction of the photogenerated iodine is consumed by the disk. The difference in the forward and reverse curves is a further indication of a decrease in the yield of soluble iodine.

The experimental circumstances of figures 17 and 18 correspond to the case (a), in which the photon flux < the iodide flux at the disk electrode surface. The anodic disk current is light controlled and is thus independent of the rotation speed. Under these conditions a rigorous resolution of mass transfer limited currents from other disk current components is difficult. Although the ring indicates that regenerative photooxidation of iodide is the dominant process we know from the deterioration of interface kinetics and stability measurements, that film formation and substrate dissolution additionally consume photogenerated holes. In order to asses the effects of the electrolyte components on the $CuInSe_2$ performance it is necessary to operate under mass transport conditions, case (b), so that i(redox species) < i(photo). To attain this condition low concentrations of the respective redox species with the illumination used in the experiment of figure 17 were employed.

6.1.3 MASS TRANSFER CONTROLLED REACTIONS IN DILUTE(2mM) IODIDE/IODINE , pH 0

Figure 19 shows i(D)-E(D) traces in 2mM I^-/I_2 + 1M H_2SO_4 of $CuInSe_2$ disk, under sufficient illumination to achieve mass transport control,case (a). The initial anodic trace, solid curve, from 0-0.3 V shows a well defined wave under steady state conditions. Reversal of the scan direction as iD starts to increase at 0.3 V produces some hysteresis. Scanning to -0.2 V also yields a cathodic current wave. Subsequent anodic scan,

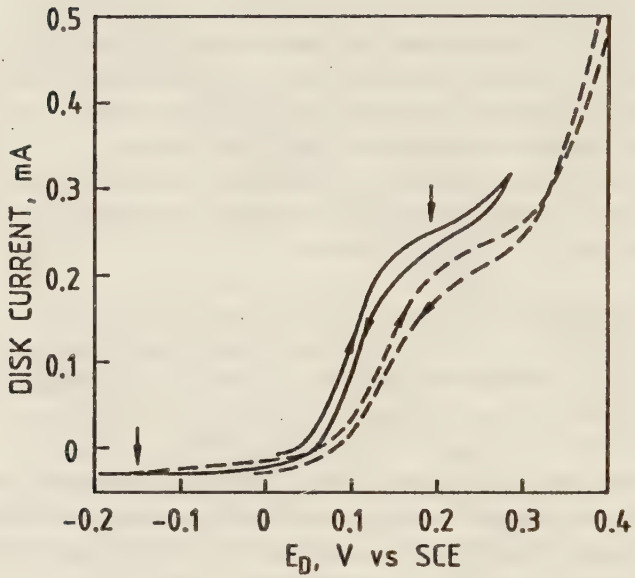

Figure 19. Current-potential curves at illuminated $CuInSe_2$ disk- Pt ring in 2mM I^-/I_2 and 1M H_2SO_4. Arrows indicate scan direction and sequence at the rate of 20 mV/sec.

dashed curve, shows increased hysteresis and poorer definition in the anodic wave. Exceeding the anodic current, in the corrosion region at 0.4 V, does not seem to deteriorate the electrode behavior to the extent of the deterioration from the cathodic scan. Subsequent scans between these potential limits yield more reproducible curves.

Differentiation between solution transport dependent and surface processes is possible through the sensitivity of the current to the rotation speed. One approach at observing this difference is by potentiostating the disk electrode in the limiting current regions, indicated by the arrows in figure 19,

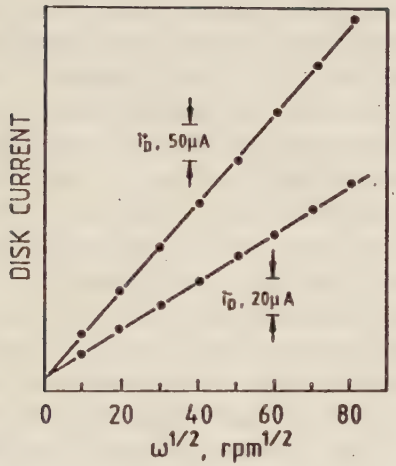

Figure 20. CuInSe2 disk currents, i(D+) at E(D) = 0.175 V and i(D-) at E(D) = -0.15 V vs SCE, plotted versus square root of rotation speed. Experimental conditions as in figure 19. current levels when i(D) = 0.

and measuring the $i(D)$-$w^{1/2}$ relation. The Levich plots obtained for the cathodic and the anodic branches of the disk current, i(D-) and i(D+) are shown in figure 20. From the linearity of these plots we conclude that the anodic and the cathodic waves represent solution transport dependent processes and further that the light intensity is not a limiting factor for the anodic process even at the higher rotation speed.

Identification of the solution species transported to and from the $CuInSe_2$ disk during the anodic and cathodic process is possible with the Pt ring. Operation in the mass transport control mode allows further resolution than was achieved under the experimental conditions in figure 17, and provides an additional ring monitor i.e. the shielding and collection of

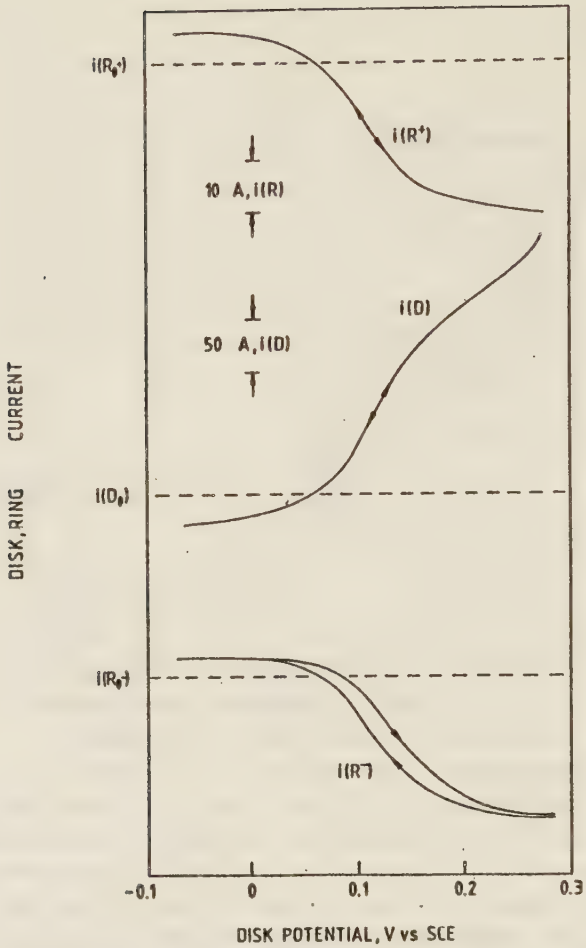

Figure 21. Disk potential scans at 10 mV/sec in 2mM I^-/I_2 + 1M H_2SO_4 wih n-$CuInSe_2$ disk current, i(D), ring oxidation, i(R+), and ring reduction, i(R-). i(R+)o and i(R-)o are ring current levels in the absence of a disk reaction.

iodide. Since iodide is present in millimolar concentration, steady state limiting currents for oxidation of I^- can be attained at the ring, as in figure 16. It is thus possible to detect the I^- consumption as well as generation at the disk.

Figure 21 is a composite of disk, ring shielding and collection currents for the anodic and cathodic disk potential scan under the intense illumination of figure 19. The ring data were accumulated in successive scans. Since the disk behavior is reproducible, both ring processes can be considered as occuring simultaneously. The ring potentials, E(R+) and E(R-), are set according to figure 16, to oxidise I^- and reduce I_2, forward and reverse reaction 8, at limiting currents in the i(R+) and i(R-) scans. The dashed lines show the unshielded ring currents for the two reactions in the absence of disk processes. If I- is removed by the disk oxidation at E(D) > 0.8 V, i(R+) should decrease from i(R+)o to a shielded level and i(R-) should increase from i(Ro-) due to collection of the disk products. The changes in i(R+) and i(R-) ought to be equal in magnitude and opposite in sign. Similar but reverse changes are expected at E(D) > 0.8 V, if the cathodic disk process involves reduction of I_2. Figure 21 shows that these conditions are realized for both anodic and cathodic branches of the i(D) curve. It may be, therefore, concluded that these processes represent oxidation of iodide and reduction of iodine. As seen in figure 20 both redox processes are convective diffusion controlled and further the anodic process is also light controlled, figure 17.

Simultaneous monitoring of species consumed and species generated at the disk, indicates that the photooxidation of iodide and the reduction of iodine yield soluble products, at limiting currents, nearly quantitatively. However, although the anodic i(D) and i(R+) curves are retraceable on the cathodic reverse, at the scan rate of 0.1 V/min, the hystheresis in the rising part of the (iR-) trace is significant. The iodine collection current actually increases during the cathodic scan. This hystheresis is more pronounced at faster scan rates suggesting surface processes involving I^- and I_2.
The effects of H^+ ions are seen in the next experiment in neutral solutions.

6.1.4 BEHAVIOR AT pH 7 AND THE EFFECT OF H^+

The solid i(D), i(R+) and i(R-) curves in figure 22 shows the experiment of figure 21 in a neutral supporting electrolyte and higher concentration of I^-. The limiting current for the photooxidation of I^- is indicated by only a slight inflection in the curve i(D). Considerable hystheresis is observed at the foot of the curve prior to the reduction wave. The anodic and cathodic redox reactions at the disk cause concommitant changes in the ring fluxes, i(R+) and i(R-) curves. The ring currents continue unaltered when the disk crosses over into the corrosion regime at 0.2 V. For the anodic photooxidation process, i(R+) follows the shape of the i(D) scan and reaches a limiting value at a potential corresponding to the inflection in i(D) indicating that I^- is being consumed by the disk. Detection of the photogenerated I_2, shown by the i(R-) trace, is not synchronous with either the onset of i(D) or the decrease in i(R+). The hystheresis between the forward and reverse i(R-) traces is considerably greater than that seen in the corresponding curve of figure 21. The current increase in the reverse trace, in the potential between 0 and 0.1 V, implies that the flux of I_2 generated is higher than expected from the consumption of I^-, i(R+) curve. Alternatively, this increase could also result from the collection of soluble species from a surface reaction at the disk.

The effect of H^+ ions on the ring and disk reactions is shown by the dashed curves. 0.1M HCL content is sufficient to reduce the hystheresis in the ring and disk curves as well as to improve the definition of the anodic disk limiting current wave.

The results in figure 22 infer that not all the I^- consumed by the disk is converted to soluble I_2. A small fraction may be incorporated in the surface film during the forward scan, so that less of it reaches the ring, i(R-).

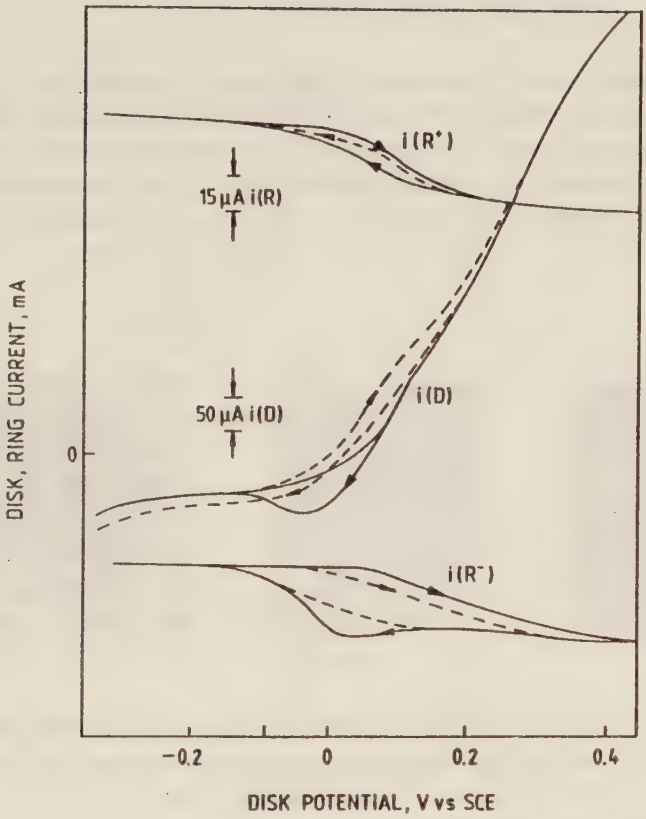

Figure 22. Experiment of figure 21 in 10mM I^-/I_2 + 0.5M KCl(solid lines) and with addition of 0.1M HCl (dashed lines).

The increased collection during the reverse scan may be accounted for, by the additional flux of I_2 or some other reducible species, released by the reduction of a surface film, during the cathodic disk transition. Higher solubility of this film in an acidic medium may explain the reduced hystheresis in the dashed curves.

6.2 ANALYSIS OF CORRODED $CuInSe_2$ SURFACE

Insight into the corrosion reaction of $CuInSe_2$ in I^--I_2-HI solution and identification of the surface film, implied by the RRDE experiments, is provided by scanning electron microscopic examination in conjunction with X-ray fluorescence analysis of the electrode surface before and after exposure to the electrolyte.

A B1 B2

Figure 23. SEM of (A) as sawn $CuInSe_2$(112) surface and the surfaces of a photoelectrode after photocorrosion for (B1) 1 hour and (B2) 20 hours in I^--I_2-HI electrolyte. Marker represents 10 microns.

Figure 23 shows SEM of (A) an untreated $CuInSe_2$ surface and (B1) and (B2) the surface of a (112) photoelectrode after 1 20 hours of photocorrosion, respectively, at the maximum power point in I^--I_2-HI electrolyte. The white triangular crystals, which distinguish surface B2, constitute the crusty deposit visually observed on the corroded electrode surface. Formation of these crystals (B1) is evident during the first hour of exposure of the crystal to the electrolyte.

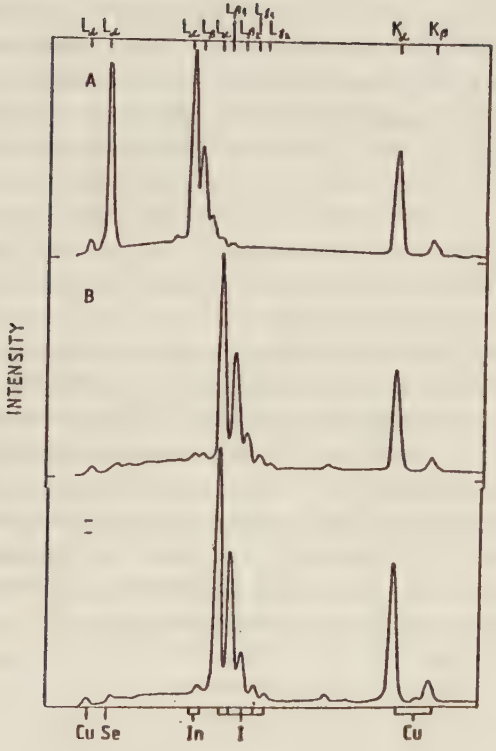

Figure 24. XFR traces of (A) untreated $CuInSe_2$, (B)triangular cyrstallites in figure 23 B1 and B2 ,(C) CuI standard.

Figure 24 shows the results from XRF analysis of the two surfaces shown in figure 23. Trace A shows $K\alpha$, $K\beta$, $L\alpha$ lines of Cu, $L\beta$ line for Se and $L\alpha$, $L\beta$ lines of In for the as machined $CuInSe_2$ surface of the reference sample. The dark areas on the corroded surface (B) yield the same spectrum indicating that it is essentially the $CuInSe_2$ substrate. The white triangular crystals show the same Cu lines. But instead of the In and Se lines, $L\alpha$, $L\beta 1$, $L\beta 2$, $L\gamma 1$ and $L\gamma 2$ lines of Iodine appear. Trace C was obtained for a reference sample of pure CuI. The relative intensities for this CuI standard are similiar to those of trace B thus identifying the triangular crystals as CuI.

Formation of CuI is apparently an intermediate step in the corrosion process of the $CuInSe_2/I^-$-I_2-HI/C cell. A potential difference of 0.3 mV, measured between $CuInSe_2$ electrode and Cu(I)/Cu in a CuCl solution, indicates a concentration gradient. Self-diffusion in $CuInSe_2$ is dominated by the motion of Cu between Cu vacancies via interstitial or substitutional mechanism [54] and chemical diffusion may also occur by the same mechanism. Conduction of Cu ions to generate CuI at the interface could thus lead to the degradation of the semiconductor.

6.3. VOLTAMMETRY OF $CuInSe_2$ IN $Cu^{+/++}$

Diffusion of Cu ions from the $CuInSe_2$ substrate into the electrolyte appears to be responsible for the degradation of the cell. Further insights into the degradation mechanisms are provided by the rotating ring-disk studies of the interactions between $CuInSe_2$ and the $Cu^{+/++}$ couple.

6.3.1 CHARACTERISTICS OF $Cu^{+/++}$

Voltammetry of Cu has also been extensively investigated by various methods including the RRDE [55]. Existence of the two oxidation states depends on the solution medium. In non-complexing solutions Cu exists predominantly in the divalent state. Solutions of $Cu^{+/++}$ ions are stable in the presence of complexing agents. Monolayers of Cu ions are also adsorbed on Pt and reduced at underpotentials [56]. Evidence for the existence of Cu^{+++} in alkaline solutions has also been found [57].

The current-potential behavior of $Cu^{+/++}$ in HCl varies with the state of oxidation of the Pt electrode. Oxidised electrodes have to be reduced in $Cu^{+/++}$ free solutions to reduce residual currents. The i(R) - E(R) curve of $Cu^{+/++}$ in 1M HCl at the Pt ring shown in figure 25 was observed by linearly scanning E(R) between -0.5 and 0.5 V. The cathodic trace shows a poorly defined wave for the reduction

$$Cu^{++} + e \dashrightarrow Cu^{+} \qquad (11)$$

in the potential region indicated by E(R-)1. The poor definition is caused by residual currents and underpotential deposition of adsorbed Cu ions. A second wave observed in the region E(R-)2 is a composite of reductions,

$$Cu^{+} + e \dashrightarrow Cu \qquad (12)$$

$$Cu^{++} + 2e \dashrightarrow Cu \qquad (13)$$

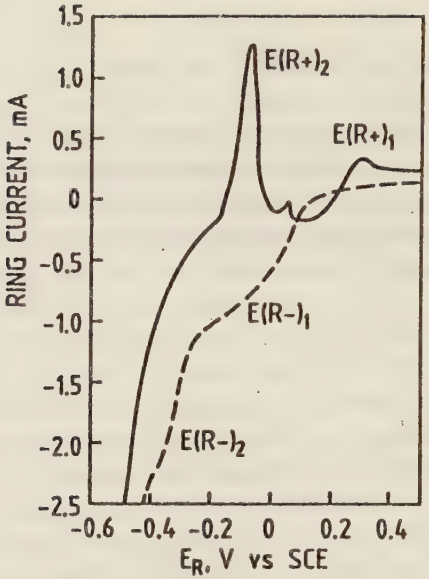

Figure 25. Ring potential scan in 10mM $Cu^{+/++}$ + 1M HCl. E(R+)1 and E(R+)2 are oxidation potentials and E(R-)1 and E(R-)2 the reduction potentials for the two valence states of Cu.

Both waves show rotational speed dependence indicating that they involve convective diffusion controlled processes. Better definition of the waves is observed on the anodic potential scan. The anodic peak superimposed on the reduction wave results from the dissolution of the electrodeposited Cu via oxidation,

$$Cu \dashrightarrow Cu^{+} + e \qquad (14)$$

The magnitude of this peak increases with the cathodic potential limit and the period of the reduction at -0.5 V. The anodic wave at E(R+)1 includes currents from the oxidation

$$Cu^{+} \dashrightarrow Cu^{++} + e \qquad (15)$$

as well as dissolution of the underpotential deposited monolayer.

6.3.2 REDOX REACTIONS AND SURFACE INCORPORATION OF $Cu^{+/++}$, pH 0

Figure 26 shows disk current curves obtained by linearly scanning the disk potential between the limits of +0.5 and -0.4 V in 1M HCl containing $Cu^{+/++}$ redox couple. After the initial scan the i(D) trace is reproducible. Following the cathodic wave at -0.4 V, figure 26, i(D) rises yielding two oxidation peaks C and D superimposed on the wave B. Wave A shows rotation speed dependance. The magnitude of peak C varies with the time that the electrode remains in the region A whereas that of the peak D is invariant. Similiar peaks have been observed on metal electrodes and have been attributed to the dissolution of bulk Cu, peak C, deposited during the reduction A, and to the dissolution of underpotential deposited monolayer of Cu, peak D, [57]. At 0.15 V, i(D) crosses zero and rises to another peak E, drops sharply indicating a passive transition and levels off to near zero on the reverse scan represented by the region F. Surface reactivation occurs during the cathodic transition G and the reduction process A is resumed at -0.4 V.

Anodic and cathodic traces of figure 26 imply that the electrochemistry of $Cu^{+/++}$ at $CuInSe_2$ is complicated by the superposition of several film formation and dissolution processes on the mass transfer controlled redox processes. Detection of these processes at the platinum ring is further complicated by drifts in background currents arising from adsorption of copper and chloride ions. However by comparing the flux changes at the ring in the two detection modes of shielding and collection, a qualitative picture of the various concurrent disk processes may be derived.

i(R+) and i(R-) curves in figure 27 were obtained in separate scans with different ring potentials, E(R+) and E(R-), corresponding to E(R+)1 and E(R-)1 in figure 25, adjusted to

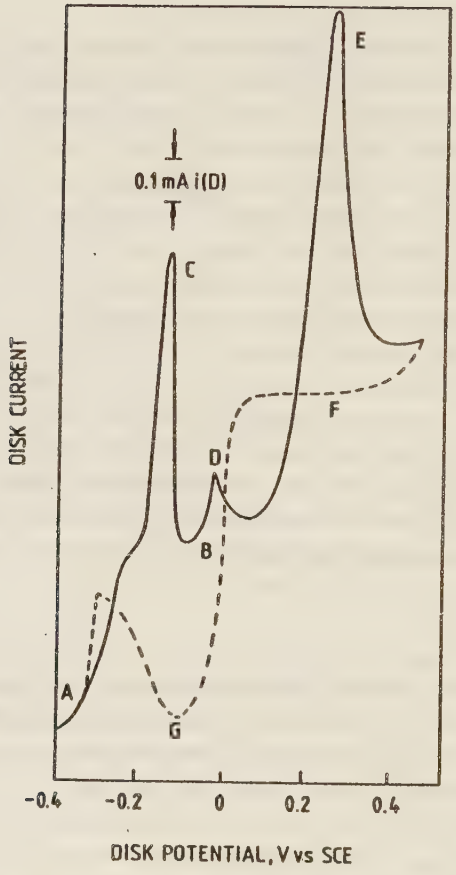

Figure 26. Disk current at illuminated $CuInSe_2$ in 10mM $Cu^{+/++}$ + 1M HCl. Solid curve is the anodic scan and dashed curve is the cathodic scan of disk potential at 10 mV/sec. w = 1600 rpm.

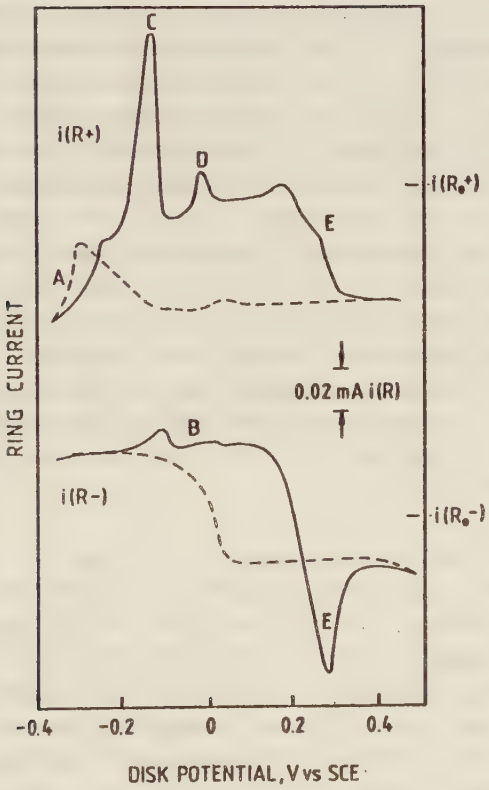

Figure 27. Ring oxidation, i(R+), and reduction, i(R-) currents, corresponding to the disk curves (solid and dashed) in figure 22. E(R+) = 0.4 V and E(R-) = -0.1 V vs SCE.

oxidise Cu^{+} and reduce Cu^{++}, via reactions 15 and 11 respectively. The unshielded ring currents, i(R+)o and i(R-)o, were estimated from the ring current levels when i(D) crosses the zero of the current axis. Disk processes A, C and D are tracked by i(R+) indicating that these transitions consume or generate Cu^{+}. Shielding of Cu^{+} in region A implies its consumption by the disk, via the deposition reaction 12. Subsequent dissolution of copper to Cu^{+} manifested by peaks C and D, is seen in the collection currents of these peaks at the ring, where Cu^{+} is further oxidised to Cu^{++}. In the potential region between -0.4 and 0.15, i(D-) shows a fully shielded wave of Cu^{++}, for the disk process B. This shielding continues into the region A indicating that the total cathodic disk current at A comprises reactions 12 and 13. Generation of Cu^{+} at the disk is not evidenced by an increase in i(R+) in the region B. This may be due to either incorporation of this Cu^{+} into the electrode surface or masking of the oxidation current at the ring by other concurrent processes. Cu^{++} generated by i(D) peak E is collected by i(R-). Corresponding changes in Cu^{+} flux at i(R+), by shielding, represent less than half of the magnitude of the peak E at i(R-). As i(D) and i(R-) decrease from the peak value, i(R+) actually increases.

During the cathodic scan, in the region F of the disk passivity, i(R+) and i(R-) continue to indicate shielding of Cu^{+} and generation of Cu^{++} at the disk. As i(D) proceeds into the cathodic region G, i(R-) decreases as Cu^{++} is reduced at the disk. Only a part of the current in the region G is accounted for by i(R-) equivalent to that consumed by process B of the anodic scan. The rest of the current under the peak G probably involves surface filming. i(R+) on the other hand shows only a small inflection as i(D) changes polarity and continues in the shielding mode until the maximum of the peak G. The simultaneous shielding of Cu^{+} and Cu^{++} in the region G suggests that the flux of Cu^{+} arriving at the disk surface by convective diffusion

transport as well as those produced by the reduction of the flux of Cu^{++} ions are being assimilated by the semiconductor during the transition G. Upto the end of the anodic scan very little photoresponse is observed . The processes described occur in the dark as well. Photocurrent is observed only at E > 0.5V.

The difference in the flux changes of Cu^{+} and Cu^{++} may be accounted for, by a dissolution of surface incorporated Cu^{+} during the process B. The disparity in i(D) and i(R+) suggests that all processes at $CuInSe_2$ involving Cu ions may not be charge transfer reactions or charge consuming processes. Adsorption/desorption or intercalation/deintercalation of Cu ions may account for the differences in the flux.

These results show that normal redox reactions 11-15, including bulk and monolayer deposition and stripping, processes A, B, C and D, observed on metal electrodes, figure 25, also occur on $CuInSe_2$. These reactions are superimposed by non Faradaic processes involving Cu^{+} incorporation into or release from the semiconductor in regions E, F and G.

6.4. REACTIONS AT $CuInSe_2$ IN A COMPOSITE ELECTROLYTE COMPRISING COPPER AND IODIDE IONS, pH 0

Figure 28 shows the effects of adding 10mM I^- to the $Cu^{+/++}$-HCl solution employed in the experiment of figure 26.

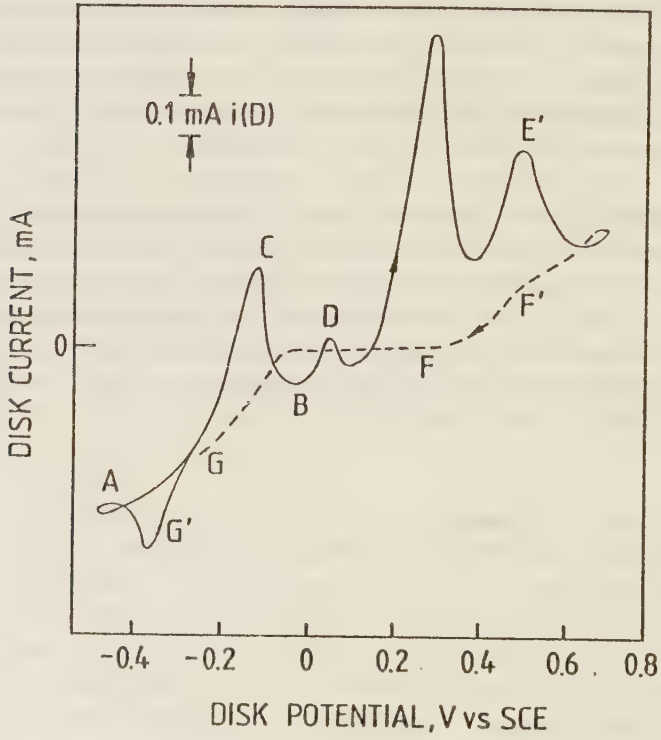

Figure 28. Potential sweep cycles at illuminated $CuInSe_2$ disk in 10mM I^-/I_2 + 10mM $Cu^{+/++}$ + 1M HCl. Letters A-G are assigned to transitions in the disk proceses as in figure 22. Letters E', F' and G' represent additional transitions in the presence of I^-/I_2 couple.

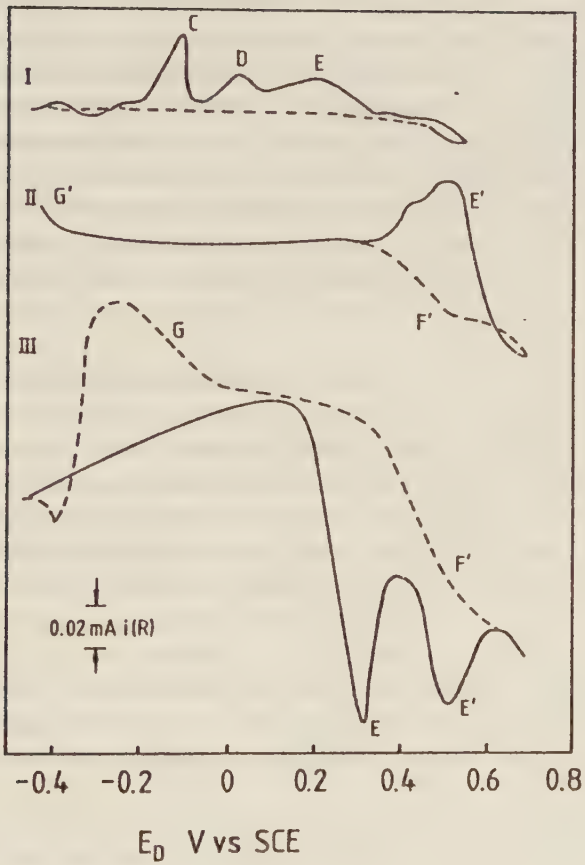

Figure 29. Ring current traces at constant ring potentials. Curve I, E(R+) = 0.4 V; curve II, E(R+) = 0.6 V; curve III, E(R-) = 0.1 V vs SCE. Letters indicate shielding or collection of Cu^{+}, Cu^{++}, I^{-} and I_2 during the corresponding disk transitions of figure 28.

Comparison of the i(D) curves in figures 26 and 28 that the peak E is retained. An additional peak E' develops at E(D) > 0.5 V superimposed on a mass transport limited wave indicated by F' on the cathodic scan. The passive region F extends ~ -0.1 V more negative. Processes in the region G are also separated into a convective diffusion controlled, rotation speed dependent wave G upto -0.3 V and a peak G' at -0.35 V. The characteristics of the anodic scan in the region G depend on the cathodic E(D) limit. Reversing the scan direction at -0.35 V yields the solid curve in the anodic direction of the region H; extending the negative potential limit to -0.4 V yields the dashed curve with peaks C and D superimposed on the wave B as in figure 26.

Fluxes to and from the disk during the potential cycle of figure 28 analyzed by the ring are shown in figure 29. The changes in the fluxes of Cu^{+} and I^{-} are monitored by curves I and II at E(R) of +0.4 V and +0.6 V respectively. At E(R) = -0.1 V, curve III, the ring detects both Cu^{++} and I_2 species generated or consumed by the disk. Potential regions of the various disk transitions are indicated by letters A-G.

Curve I shows no shielding of the peak G'. Cu^{+} dissolved by peaks C and D is however detected. Shielding of peak E is detected but is prevented from reaching the level observed in figure 27 (curve i(R+)) by a concurrent process at 0.3 V.

Curve II shows an increase in the flux of I^{-} released from the peak E' and G', and shielding of I^{-} during the reverse scan at F'.

Curve III shows shielding of the cathodic wave G and collection in the region G'. Collection continues in the reverse scan, drops to the unshielded level at ~ 0.1 V and increases again reflecting peaks E and E'. Collection wave in he region F' corresponds to the shielding wave for I^{-}, curve II and can thus be interpreted as collection of iodine.

6.5. FORMATION AND DISSOLUTION OF CuI

The processes in figure 28 appear quite complex as they involve reactions of two systems represented by figures 20 and 26 as well as, reactions between the two systems. Processes A, B, C, E, F and G were observed in the system of figure 26. The new transitions may be interpreted in terms of equations 1 - 5. Addition of iodide to $Cu^{+/++}$ solutions could result in several changes in the solution composition as well as in the semiconductor surface chemistry. Cu^{++} content of the electrolyte is expected to be considerably reduced or eliminated via reaction,

$$Cu^{++} + 2I^{-} \dashrightarrow CuI + 1/2I_2 \qquad (16)$$

generating iodine in the solution. Reaction 16 goes to completion inspite of the more positive reduction potential of the $Cu^{+/++}$ couple relative to the covalent character of the Cu-I bond and the low solubility of CuI in aqueous solutions [58]. Further, as seen in figure 24, CuI is also formed readily on $CuInSe_2$ in acidic media via reaction

$$Cu^{+} + I^{-} \dashrightarrow CuI \qquad (17)$$

but requires high I^{-} concentration to dissolve via a complexation reaction

$$CuI + I^{-} \dashrightarrow CuI_2^{-} \qquad (18)$$

and may therefore exist as a film on the electrode surface.

Transition E' releases I^{-}, curve II, and Cu^{++}, curve III, in the anodic scan and is quite likely to involve oxidation of CuI by

$$CuI \rightarrow Cu^{++} + I^{-} + e \qquad (19)$$

The oxidation potential for reaction 19 of 0.62 V vs SCE [59] corresponds to that of the peak E'. This transition E' is superimposed on the I^{-} oxidation wave as seen by the development of a shielding wave in curve II and a collection wave in curve III at 0.6 V. These waves are clearly visible during the cathodic scan, region F', without the superimposed filming processes.

Since Cu^{++} in the electrolyte is expected to be reduced by reaction 16, the shielding current in region G detects only I_2 species. I^{-} is not collected by curve II, hence it may be incorporated in a surface film involving reaction 17. Se and In reactions have not been considered. If these ions occur as soluble reaction products, they would not interfere with the ring detection of Cu and I ions in this potential range according to figure 17.

Peak G' appears at a potential corresponding to the reduction potentialof -0.43 V vs SCE [59] of CuI by,

$$CuI + e \rightarrow Cu + I^{-} \qquad (20)$$

Therefore Cu deposited in this process dissolves as Cu^{+} during the anodic scan as detected by curve I, peaks D and C, which appear only when scanning into the region G'. I^{-} released from reaction 20 is collected in curve II.

6.6. CORROSION INHIBITION via FILM FORMATION

Surface analysis of corroded electrodes and the RRDE results suggest that the formation of CuI is inevitable in the $CuInSe_2/I^-$-I_2-HI system and is evidently an intermediate step in the corrosion process in the $CuInSe_2/I^-$-I_2-HI cell. The reaction mechanism is apparently leaching out of Cu+ ions from the semiconductor by the I^- ions to yield CuI by reaction 17 and subsequent dissolution of CuI in concentrated iodide solution by complexation reaction 18. CuI formation is thermodynamically favored as $\Delta H(298) = -16.085$ kcal/mol and $\Delta G = -16.058$ for Cu(s) + I(s) = CuI(s) [60]. However, a kinetic limitation exists, which might be advantageously used to stabilize the cell.

The dissociation constant of CuI is 1.1×10^{-12} and the equilibrium constant of the complexation reaction 18 is 6.3×10^{-4} [61]. The low dissociation constant of reaction 17 indicates that this is a faster process than reaction 18, thus accounting for the low solubility of CuI, which may also be responsible for the increasing cathodic passivity seen in figures 16 and 24, and the sluggish charge transfer kinetics in the absence of HI. The partial coverage of the corroded semiconductor surface by some undissolved CuI crystals and improvement in the shape od the I-V curves in figures 16 and 24 on addition of HI imply that the solubility of the film is greater but still restricted in the acidic medium. Considering the low solubility of CuI, it should be possible to raise the surface concentration of CuI_2^- to saturation level with relatively low concentrations of CuI to the electrolyte. The direction of equilibrium of reaction 18 may thus be reversed and possibly arrest semiconductor dissolution.

7. STABLE SEMICONDUCTING INTERPHASE

7.1 IN-SITU PHOELECTROCHEMICAL GROWTH

The information deduced from passivation studies, RRDE and surface analysis is collectively used to construct a PEC cell with n-$CuInSe_2$ using :

(a) I^-/I_2 couple with resonably fast kinetics, in a concentration ratio to prevent I_2 layer formation [51],

(b) HI, to improve interfacial kinetics by reducing passivity and

(c) CuI, to induce growth of an insoluble film at the interface and stabilize the cell.

Interfacial layers were grown on etched faces of n-$CuInSe_2$ by operation as photoanodes in an electrolyte consisting of 1M I^-, 0.05M I_2, 2M HI and 0.02M CuI. This involved, initially, cyclic polarization of the electrode between the potential limits of short circuit and open circuit conditions. The electrode was then left at the maximum power point. Film quality was monitored by the photocurrent-voltage output. Generally 3-4 intermediary etches were required to optimize the film performance.

7.2 CELL PERFORMANCE AFTER FILM GROWTH

(a)

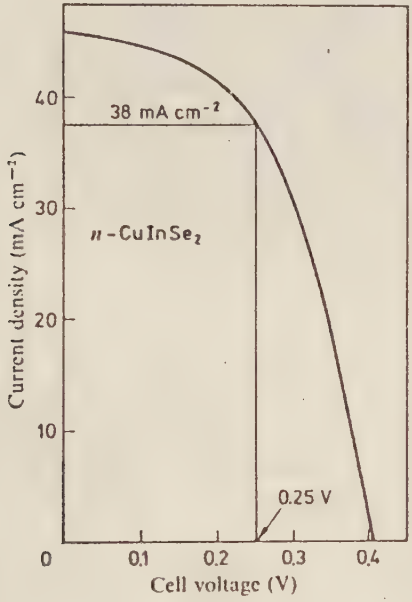

(b)

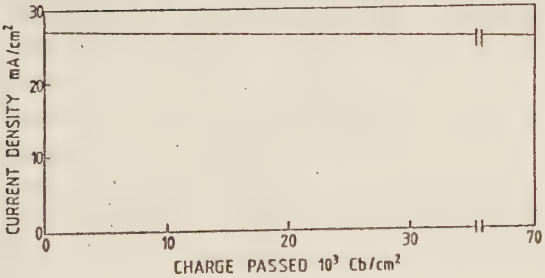

Figure 30.(a) Output power characteristics of n-$CuInSe_2$-I^--I_2-Cu^+-HI/C cell.
(b) Charge passed during operation at the maximum power point (0.25 V vs E(redox).

The performance of n-$CuInSe_2$ on addition of 0.02M CuI to the electrolyte employed in the experiment of curve 3, figure 15 is shown in figure 30. A maximum output of 9.4 mW/cm^2 is delivered at 0.25 V and 37.7 mA/cm^2 under AM1 illumination. presence of Cu(I) does not alter the I-V characteristics significantly from the initial output obtained in the absence of Cu(I) ions in solution. However the loss in FF and Voc observed in subsequent scans, figure 19, can be recovered by the addition of CuI. A Long-term stability measurement performed near the maximum power point is shown in figure 30b. After passage of 70,000 C/cm^2, the cell continues to deliver virtually unchanged photocurrents.

In a parallel experiment the stability of $CuInSe_2$ in this electrolyte was also tested in dark without applied potential. 1-2 mm thick wafers of $CuInSe_2$ single crystals were left immersed in the electrolyte for a period of 5 weeks. No measurable changes in weight or thickness of these samples or those operated in the light was observed.

7.3 FILM MORPHOLOGY AND COMPOSITION DURING AND AFTER GROWTH WITH SEM AND XRF

Visual inspection of the electrode after the stability test evidenced an altered surface morphology. Characterization of the new phase and insights into the circumstances leading to $CuInSe_2$ surface transformation and thus to the stabilization of the cell are provided by SEM and XRF analysis. Morphology of three films on, grown under different conditions on electrode surfaces, are displayed by the SEM photographs in figure 31.

The surface of an electrode during the initial stages of film growth is shown in figure 31A. This film was grown by the proceedure described above for a period of 30 minutes. The film appears polycrystalline comprising cystallites of hexagonal shape.

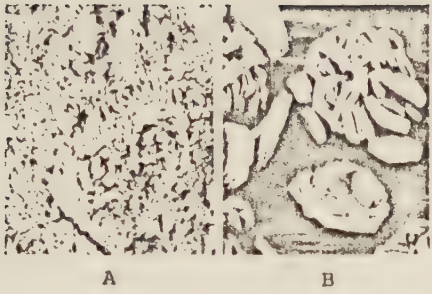

Figure 31. Scanning electron micrographs (SEM) of films on $CuInSe_2$ grown in I^--I_2-Cu^+-HI electrolyte showing: A, initial stages of photoelectrochemical growth during 30 min; B, growth by immersion in the dark for 5 weeks; C1, topography and, C2, C3, profiles of film after 5 weeks of continuous photoelectrochemical operation.

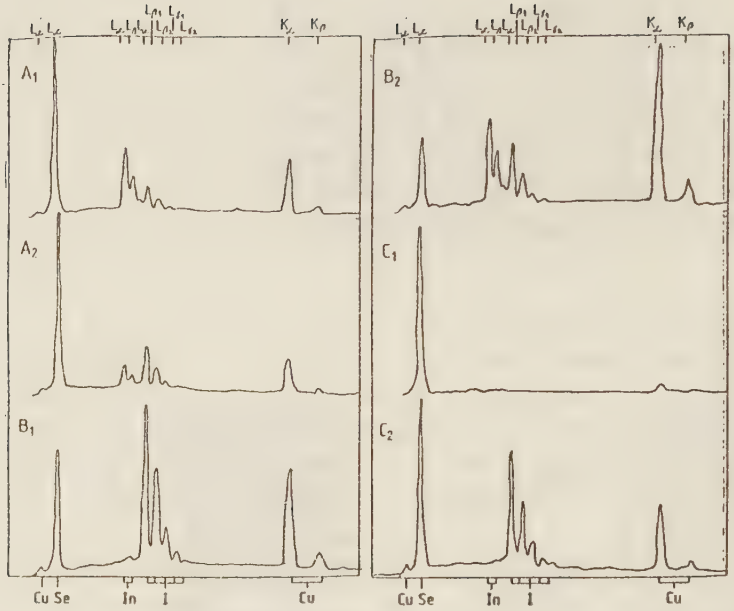

Figure 32. X-Ray fluorescence analysis of surfaces shown in figure 31. A1, A2, show two quartenary composites on SEM A; B1 represents the dark areas of SEM B and B2 the hexagonal crystallites. C1, C2, represent the hexagonal cystallites on SEMs C1, C2 and C3.

Figure 32B shows the topography of the film grown by immersing $CuInSe_2$ crystals in the acidified polyiodide electrolyte, in the dark for 5 weeks. Agglomerates of hexagonal crystallites are seen interspread on a dark relatively smooth surface. The growth appears dendritic and the substrate coverage incomplete or very slow. The indvidual crystallites are flat and randomly oriented with sizes ranging between 2-5 microns.

Front and lateral views of the film grown on the sample employed in the stability test are shown in figure 31. Figure 31C1 shows that a polycrystalline film comprising hexagonal crystallites, resembling those of figure 31B, covers the $CuInSe_2$ substrate. The crystallites are also randomly oriented. Figure 31C2 shows a cross-section of a cleaved crystal with the film. The growth of the platelets from the film is clearly visible. The film does not penetrate deeper than 2 microns into the substrate even after prolonged operation (5 weeks). The film, however, appears to completely cover the substrate and, as shown in figure 31C3, grows also into microscopic crevices.

Compositional analysis of the surfaces shown in figure 31, including the hexagonal crystallites is given by the XRF traces in figure 32. Trace A1 shows the Cu, In and Se lines seen for $CuInSe_2$ substrate in figure 23A. the relative intensities of the two cations, Cu and In are much lower compared to that of Se. In addition the I lines seen in figure 23B for CuI appear also at lower intensities. Trace A2 corresponds to another spot on the same surface of figure 31A. A similar quarternary composite is detected but the comparatively lower intensity of In suggests a different stoichiometry.

Composition of the dark underlying area on the surface shown in figure 31B is shown by Trace B1. Another stoichiometry of the quartenary composite is found with relatively enhanced Cu intensity and diminished Se intensity. In contrast to the dark, uncovered areas of $CuInSe_2$ in figure 23, trace B1 shows surface transformation in the dark areas of figure 31B by incorporating I and additional Cu. Trace B2 corresponding to the hexagonal crystallites of figure 31B, shows Se lines in addition to the Cu and I lines observed for the triangular crystals in figure 23B. The hexagonal shape and the the Se content distinguish the new layer grown in Cu^+ containing electrolyte from the CuI crystals on corroded surfaces.

The hexagonal crystallites in figure 31C are characterized by trace C. The same Cu, I and Se lines seen in in trace B2 are found. No trace of In or $CuInSe_2$ was found on the entire surface of the electrode within the detection limits of XRF. A substantial fraction of the hexagonal cystallites were characterised by trace C2 as comprising elemental Se.

7.4. FILM IDENTIFICATION

7.4.1 OXIDATION STATES OF FILM COMPONENTS AND DEPTH PROFILE BY XPS ANALYSIS

Oxidation states of the various constituents of films grown on $CuInSe_2$, air annealed and annealed/electrolyte exposed were determined by XPS. This technique exhibits high surface sensitivity(depth resolution ~ 30 A^{o}) but lower lateral resolution than XRF and can thus provide supplementary information on surface composition and allow depth profiling.

TABLE I

(a) $CuInSe_2$ substrate

Element	E(B)	(FWHM)	n	Intensity	SPC	Intensity Correction	Stoichiometry
Cu	932.6	(1.5)	0,1	3189	1.5	2126	0.8
In	444.8	(1.0)	1,2,3	5412	1.88	2878	1.08
Se	54.4	(1.7)	-2,-4	1212	0.24	5050	1.9

(b) Film grown photoelectrochemically on $CuInSe_2$

Element	E(B)	(FWHM)	ΔE(B)	ΔE1/2	Int. Corr.	SPC	Intensity	Stoichiometry
Cu	932.6	(1.5)	0	0	3888	1.5	2592	1
In	444.9	(1.3)	0.1	0	935	1.88	497	0.2
Se	55.0	(2.1)	0.6	0.4	807	0.24	3362	1.3
I	619.4	--	---		155	1.88	828	0.3

The binding energies E(B), the full width of half maximum (FWHM) values and the subshell photoionisation cross section(SPC) observed for the untreated $CuInSe_2$ surface and for surfaces with films grown in I^--I_2-Cu^+-HI electrolyte, are tabulated in Table I. Stoichiometry of the two samples, a a depth of ~800 A^o is estimated from the line intensities and the subshell photoionised cross sections. The stoichiometry estimate for the $CuInSe_2$ reference sample is in close agreement with $CuInSe_2$. The binding energies and the FWHM values for this sample correspond to Cu^+, In^{3+} and S

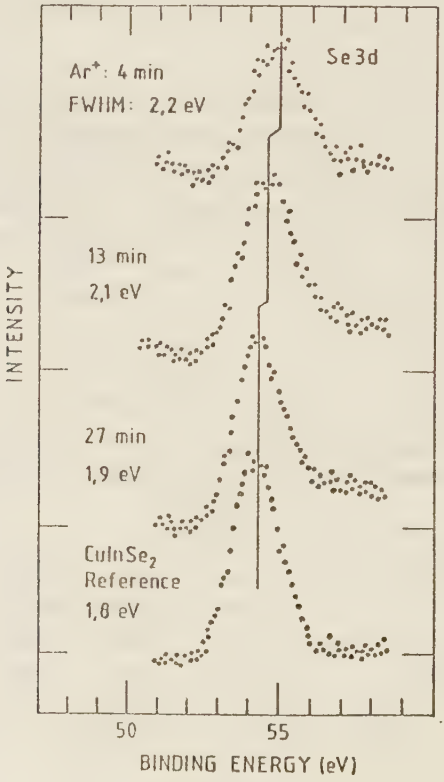

Figure 33. XPS Se lines at various sputtering times.

For the sample with film the binding energies and FWHM values for Cu and In are the same as in the $CuInSe_2$ standard, and the binding energy for the I signals corresponds to a charge of -1. However, the binding energy for Se in the film shifts and the FWHM broadens relative to the standard $CuInSe_2$ crystal as shown in figure 33. This shift and the broadening is consistent with the assumption that the Se peak observed for the surface with film represents a convolute of two signals corresponding to Se^{2-} and Se^{0} in roughly equal proportions.

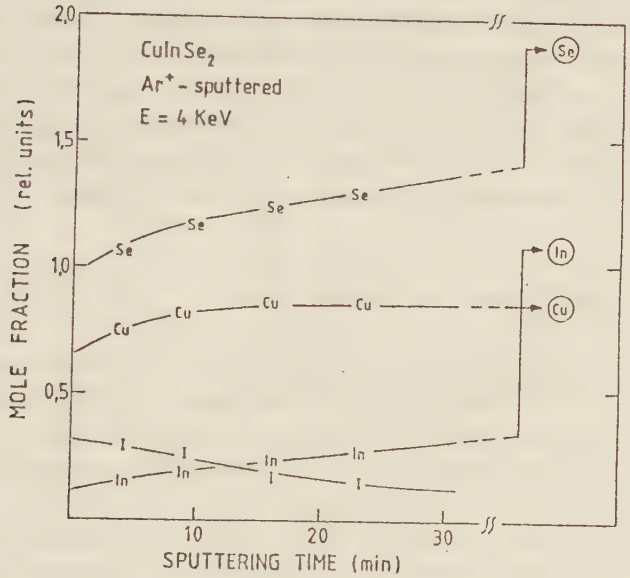

Figure 34. XPS depth profile of I, Cu, In and Se for the film grown on $CuInSe_2$ in I^--I_2-Cu^+-HI electrolyte.

XPS depth profiles for Cu, In, I and Se for the film on $CuInSe_2$ are shown in figure 34. Short sputtering (sputter rate ~20 A°/min) was necessary to remove atmospheric surface contaminants. Figure 34 reveals incorporation of I into the film, and substantial In and moderate Se depletion at the surface. The Cu concentration exhibits a relatively small variation over the thickness of the film. These measurements are averaged over a relatively large cross section. The depth profile or the stoichiometric estimate of the film does not necessarily represent the hexagonal crystallites. Variation in composition of the film constituents with distance from the substrate, as infered from the X-ray fluorescence analysis of the initial growth stages is supported by the depth profile. A small discrepancy exists between the results of the two techniques. The presence of In, as seen in the depth profile of the film, was not detected by XRF analysis. Localised heating of the sample by the X-ray beam, during the XPS experiment, is quite likely to induce diffusion of In from the substrate into the film. Subsequent annealing experiments support this explanation.

7.4.2. X-RAY DIFFRACTION OF THE FILM

The distinct crystallite geometry of the hexagonal platelets, depicted by the SEMs in figure 33C, suggests that a chemically well defined compound is grown at the $CuInSe_2/I^-$-I_2-Cu^+-HI electrolyte. The photoelectrochemically grown layer on $CuInSe_2$ substrate was analyzed with X-Ray diffraction at the grazing angle of incidence. Figure 35 shows the X-ray diffraction pattern of the film and the reference of Se and $CuISe_3$ [62], shown for comparison. The clearly identifiable peaks correspond to polycrystalline $CuISe_3$ and elemental Se.

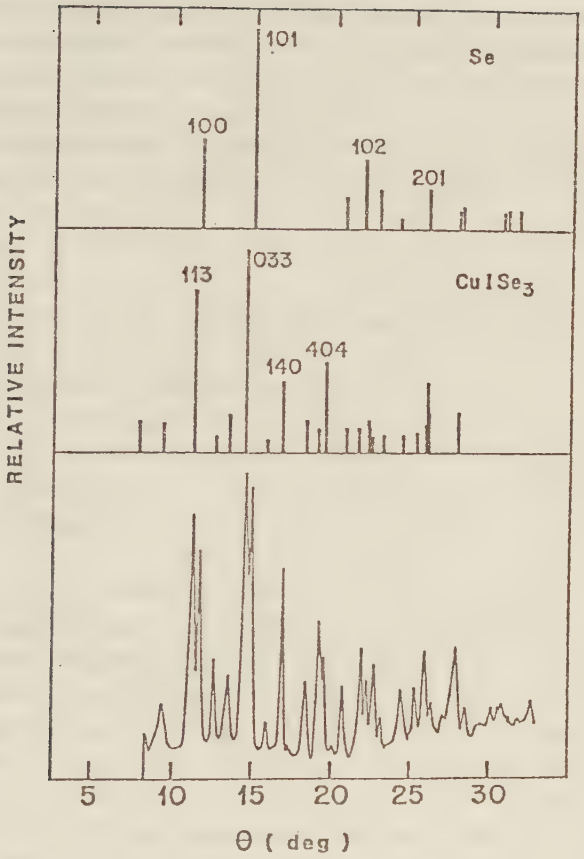

Figure 35. Grazing incidence X-ray diffraction analysis in Guinier configuration. (a) diffraction pattern of electrochemically formed film on n-$CuInSe_2$; angle of incidence 2^o; diffraction patterns of (b) elemental Se powder and (c) of $CuISe_3$ powder.

The Se content varies laterally across the sample surface and represents ~30% of the film composition. The spectrum in figure 35 corresponds to a sample with relatively high Se concentration. Due to the single crystalline nature of the substrate no pattern from the $CuInSe_2$ was detected. Amorphous films and films thinner than 500 A^o cannot be easily detected with this method. The formation of polycrystalline $CuInSe_2$ or CuI can be excluded. The good agreement between the sample and the powder diffraction data also excludes preferential orientation in the film.

7.5 CONVERSION OF $CuInSe_2$ TO $CuISe_3$-Se

The results show that the nature of the film formed at the semiconductor/electrolyte interface determines the performance of the $CuInSe_2$ photoanodes in I_2/I^- solution. The composition and the morphology of this film depend on the electrolyte constituents and the growth conditions.

ETCHED SURFACE: A native film of In_2O_3 with a transition layer of Cu_xSe has been reported to grow on single(110) and polycrystalline $CuInSe_2$ surface upon exposure to oxygen [63,64]. Similiar layers are likely to form on $CuInSe_2$ electrodes on exposure to oxidative etchant and air. The effect of HI in reducing the passivity of $CuInSe_2$ surfaces in polyiodide solutions, figure 15, suggests that the In_2O_3 is at least partially dissolved. The remaining surface layer of Cu_xSe is an ionic conductor with respect to Cu^+ ions but inhibits further growth of In_2O_3 [65]. The $CuISe_3$ and CuI films formed in solutions with and without Cu^+ ions, respectively, would thus nucleate on the Cu_xSe transition layer.

INITIAL TRANSFORMATIONS: In the initial stages of film growth the etched $CuInSe_2$ surface receives H^+, Cu^+, I^- and I_2 from the Cu containing solution. These species may be adsorbed under partial stripping of the solvation shells. Although the same chemical species exist at the surface in the dark the surface concentration of I_2 in the light is substantially enhanced as a consequence of the photooxidation reaction $I^- + h^+ \rightarrow I$. This is followed by a slow dimerization step $I + I \langle\rightarrow I_2$, complexing $I_2 + I^- \langle\rightarrow I_3^-$ and removal of the I_3^- by diffusion into the electrolyte. Clearly a high surface concentration catalyses this sequence of reactions and prevents the formation of an I_2 film. However, in view of the more electropositive potential of I_2/I^- solution with respect to Se/Se^{2-} couple, oxidation of Se^{2-} by,

$$I_2 + Se^{2-} \dashrightarrow 2I^- + Se \qquad (21)$$

is a likely reaction and leads to the nucleation of the new phase. Traces A1, and A2 in figure 32 reveal that initial surface conversion involves formation of quarternary composite of In, Cu, I and Se. The stoichiometry of this composite appears to vary. The relatively high Se intensity in these traces and the XPS data of Figure 33, imply that Se exists partly in elemental form in the initial stages of surface transformation.

$CuISe_3$ FORMATION: Prolonged exposure to the electrolyte results in further transformation generating the hexagonal crystallites of $CuISe_3$. High surface concentrations of Se (on electrode surface and CuI(in the electrolyte) in an acidic ambient are required to initiate the growth of $CuISe_3$. Surface morphology and the depth profile suggest that the film growth occurs at the film/electrolyte interface, rather than at the semiconductor/film interface, leaving a transition layer of the quartenary composite. The rate of film growth thus depends on the

availability of Se. Absence of indium in the layer, indicates that indium diffusion through this layer, at room temperature is inhibited thus leading to the cell stabilization.

TRANSFORMATIONS IN THE DARK: Similar surface reactions occur on immersion of $CuInSe_2$ into the electrolyte in the dark but at a lower rate without the assistance of light to generate elemental Se. The quarternary composite as well as the clusters of hexagonal crystallites in traces B1 and B2, figure 33, show lower Se intensities than traces A1, A2 or C2. These results lend further support to reaction 21 as an intermediary step in the synthesis of $CuISe_3$.

$CuISe_3$ crystals have been previously prepared by reacting stoichiometric mixtures of CuI and Se in a HI medium under hydrothermal conditions [66]. For the reaction,

$$CuI + 3Se = CuISe_3 \qquad (22)$$

the thermodynamic calculations yield ΔH of ~ -14.3 kcal/mol at room temperature [66]. The reactants employed in the hydrothermal synthesis of $CuISe_3$ are thus provided by the electrolyte and the semiconductor components in the cell, while the reaction enthalpy is probably supplied by the photons.

Thus chemical reactions of $CuInSe_2$ with the I^-/I_2 couple transform the semiconductor surface to generate (i) CuI as discussed in section V and, in the presence of Cu ions in the electrolyte, to generate (ii) $CuIn_xI_ySe_z$ and $CuISe_x$ in the dark, (iii) $CuIn_xI_ySe_z$ and Se, in the the light initially and (iv) $CuInSe_3$ and Se with prolonged exposure. CuI is required to prevent corrosion and light, to generate Se.

7.6 OPTO-ELECTRONIC PROPERTIES OF THE INTERFACIAL FILM

7.6.1 SPECTRAL RESPONSE

Spectral reflectance measurements performed on the hydrothermally grown $CuISe_3$ crystalls yield a band gap of 2 eV [65]. The mean value of the band gap of Se is also ~ 2 eV [66] and so the Se content in the film would not be deleterious to the performance of the junction. The thickness of the photoelectrochemically grown $CuISe_3$ film is comparable with the absorption length for direct gap materials, and could thus affect the spectral response of $CuInSe_2$. Figure 1 shows the relative spectral response of a $CuInSe_2$ electrode with the $CuISe_3$ film in the wavelength region between 800 and 1300 nm. The long wavelength cutoff at ~1.0 eV corresponds to the band gap of $CuInSe_2$ for which values from 0.934 to 1.06 eV have been reported [67-69].

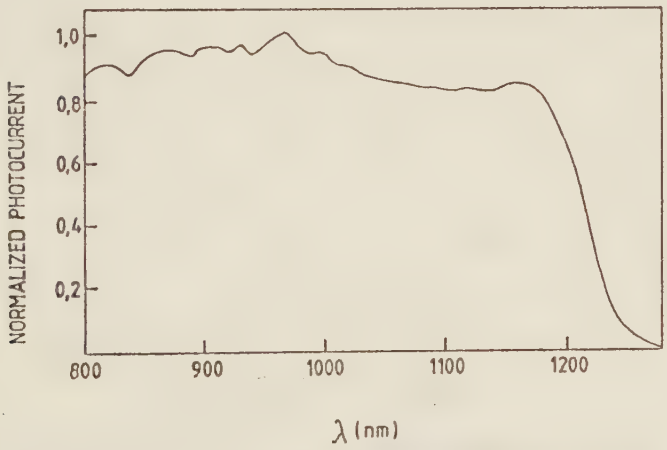

Figure 36. Long wavelength response of $CuInSe_2/CuISe_3$-Se electrode in I^--I_2-Cu^+-HI electrolyte.

7.6.2 MICROWAVE CONDUCTIVITY

Surface microwave conductivity was used to study the effect of the $CuISe_3$ film on the photogeneration and separation of charge carriers at the $CuInSe_2/CuISe_3$ interface. Light induced changes in the conductivity were monitored by detecting the corresponding change on microwave absorption as a function of time [44]. Curve I in figure 37 shows the change in amplitude and kinetics of the reflected microwave signal produced by a 530 nm laser pulse on an etched n-$CuInSe_2$ crystal. The induced conductivity shows a fast decaying peak followed by a slower decaying signal beyond 50 ns. No such signal could be obtained on an as cut $CuInSe_2$ wafer. The microwave response of $CuInSe_2/CuISe_3$ structure, in curve II, shows a higher peak amplitude as well as increased height and slower kinetics in the decaying part. Etching of the $CuISe_3$ film reverts the microwave response to that of curve I.

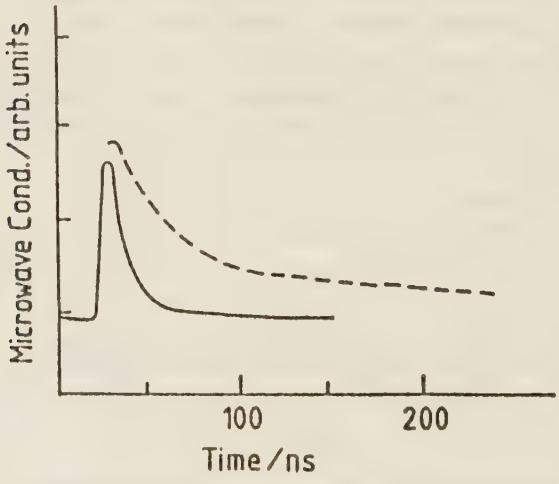

Figure 37. Excess microwave conductivity of a $CuInSe_2$ electrode upon illumination with a 20 nsec pulse of 530 nm light, before (solid lines) and after (dashed lines) film growth.

The fast kinetics of curve I indicate efficient recombination of the photogenerated charge carriers in n-$CuInSe_2$ without the film. The slower decay in curve II suggests efficient separation of the charge carriers in a space charge region. Increase in the electric field, as a consequence of formation of the $CuInSe_2/CuISe_3$ interface, could be attributed to the creation of a p-n junction. Alternatively the slow decay may be interpreted in terms of decreased surface states as a result of film formation.

7.6.3 ELECTRONIC STRUCTURE

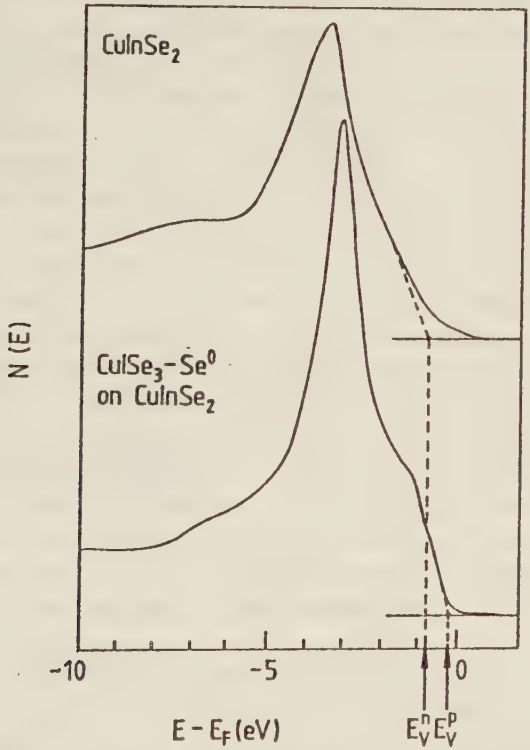

Figure 38. Energy distributions, N(E), obtained by UPS using He(II) excitation (hv = 41.8 eV).

The density of electron states in the valence band can be obtained with ultra-violet photoelectron spectroscopy, UPS, from energy distribution curves, N(E). Figure 38 compares N(E) of the untreated $CuInSe_2$ single crystal and the $CuISe_3$-Se structure. With the Fermi levels E(F) aligned, the edges of the valence band , E(V)n and E(V)p, differ by 0.65 eV. |E(V) - E(F)| is 0.85 eV for $CuInSe_2$ and 0.2 eV for the film. With a band gap of 2 eV $CuISe_3$ is thus a p-type semiconductor.

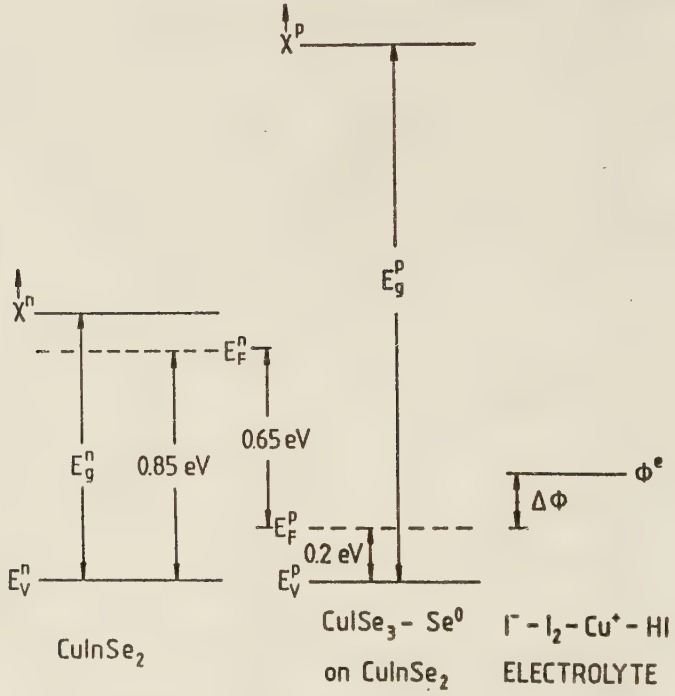

Figure 39. (a) Schematic of energy levels of n-$CuInSe_2$ p-$CuISe_3$-Se film and the electrolyte.
(b) Schematic of electrolytically contacted heterojuncti

Measurements of the relative work functions of the two samples with the vaccum levels aligned additionally indicate that the Fermi levels differ by 0.65 V. Hence E(V)[$CuInSe_2$] = E(V)[film on $CuInSe_2$]. Adding the electron affinity of 4.58 eV [70] to the band gap of 1 eV for $CuInSe_2$ the absolute value of E(V) is estimated to be 5.58 eV.

The energetics of the three junction components are compared in figure 39. Experimental and literature values for the various electronic parameters indicated with superscripts n and p refer to n-$CuInSe_2$ and p-$CuISe_3$-Se, respectively. An estimate for the work function of the I^--I_2-Cu^+-HI electrolyte of 5.1 eV is obtained by adding the measured redox potential of 0.2 eV versus SCE to the more recent value of NHE = 4.7 eV [71]. Correlation of the Fermi levels of the n- and p- type semiconductors and the work function of the electrolyte yields a junction potential of at least 0.65 eV at the substrate/film junction and of 0.2 eV at the film/electrolyte interface. This would result in a p-n junction between the solids and in a rectifying junction at the electrolyte contact. The spectral response and the anodic photocurrent, however, attest the light absorption and photogeneration of holes in the $CuInSe_2$. A barrier at the film/electrolyte interface would impede hole transfer to the iodide species. The high quantum efficiency and the photovoltage of 0.42 V argue against such a barrier and suggest that the principal potential drop occurs in the p-n junction with the minority carriers in $CuInSe_2$ being transported as majority carriers in the p-type film and the electrolyte providing an ohmic contact.

Interactions between the semiconductor and the electrolyte upon immersion may account for the energetic difference at the film/electrolyte interface, as the scheme in figure 39 disregards the effects of pH and specific adsorption.

8. INTERPHASE TRANSFORMATION

Photoelectrochemical growth of the new phase comprising polycrystalline p-$CuISe_3$ crystallites on n-$CuInSe_2$ is pivotal to the stable and efficient operation of the electrolytically contacted p-n heterojunction cell. Although the p-$CuInSe_3$-Se layer serves primarily as a window material its band gap of 2 eV [69] suggests partial contribution to the photogeneration of charge carriers. Photoresponse of the solid heterojunction thus hinges on the electronic and structural properties of the p-$CuISe_3$-Se film. In order to enhance the energy conversion efficiency of the hybrid solar cell, the parameters influencing the growth and the composition of the film have to be optimized to minimize interface states and defect sites that might hinder efficient charge transport.

The parameters affecting the film growth include surface preparation, orientation, concentration of electrolyte constituents, temperature and annealing. Dependence of the cell performance on these parameters is investigated by monitoring the current-voltage characteristics and analyzing surface transformations.

8.1 EFFECTS OF SURFACE PRETREATMENT

Surface impurities , adsorbates or lattice defects represent discontinuities in the periodicity of the chemical bonds between lattice atoms. Differences in chemical bonding between the surface atoms and the bulk lattice atoms may locate the impurity energy levels in the band gap of the bulk material

giving rise to surface states. Direct correlation between the surface topography and photovoltaic sensitivity has been found for most single crystalline semiconductors employed in solar cells. Effects of surface topography are specially acute in the case of heterojunctions where the imperfections can lead to high local density of interface states when a barrier is formed. This gives rise to a corresponding increase in the recombination velocity and an accompanying reduction in efficiency.

Preparation of the $CuInSe_2$ substrate surface prior to the film growth includes chemical etching and mechanical polishing. The effects of these procedures on the cell performance are investigated.

8.1.1 CHEMICAL ETCHING OF SURFACE LAYERS

Surface layers that have been damaged by cutting, abrasion or polishing of the semiconductor electrodes introduce recombination centers and are usually removed by selective etching. A lattice defect represents a point at a higher chemical potential than that of the lattice. Consequently, it dissolves at a potential that is inadequate to corrode the lattice. This can be advantageously used to reduce the density of lattice defects in the light absorbing region of photoelectrodes.

DEPENDENCE OF PHOTORESPONSE: The influence of etching was monitored by the photoresponse of the electrodes shown in figure 40. The low output of the as sawn $CuInSe_2$ crystals in curve (I) is attributed to the mechanical damage inflicted on the surface layers during the sawing proceedure. An etching sequence consisting of 3:1, $HCl:HNO_3$, H_2O rinse, 10% KCN dip, H_2O rinse was employed to remove surface imperfections. Cyclic polarization of the electrode between the potential limits of short circuit and open circuit conditions in the

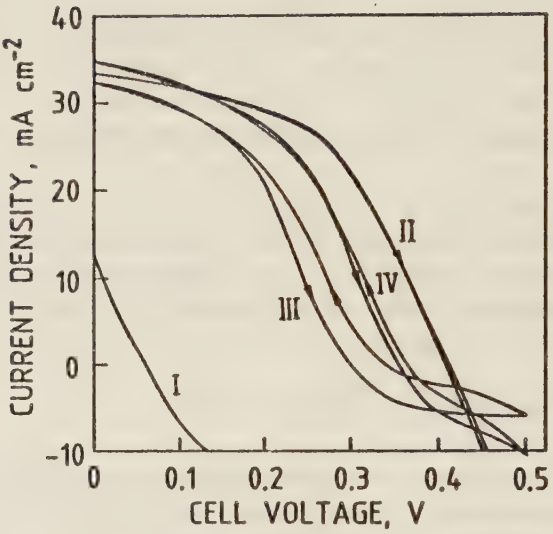

Figure 40. Effects of etching on the current-voltage output of $CuInSe_2$ in I^--I_2-Cu^+-HI electrolyte. (I) Low output of unetched surfaces; (II) improvements after 3-4 sequences ofetching in 3:1, $HCl:HNO_3$, H_2O rinse, 10% KCN etch, H_2O rinse and potential cycling between Isc and Voc; (III)deterioration on further etching in 3:1, $HCl:HNO_3$; (IV) partial recovery after KCN etch.

I^--I_2-Cu^+-HI electrolyte was also resorted to, to improve the I-V curves. Optimum output of curve (II) was attained when the sequence of etching and cycling was repeated 3-4 times. Adverse effects of further use of the oxidising etch are evident in curve (III). Hystheresis, poor FF and low cathodic currents are indicative of a passive surface.

Subsequent etching in KCN helps to remove the insoluble products of the $HCl-HNO_3$ etch, partially and yields the slightly improved curve (IV). The behavior exhibited in curve (II) can be recovered by repeatedly cycling the electrode in the I^--I_2-Cu^+-HI electrolyte. In contrast to the beneficial effect of Ru in polysulfide solutions, either negative or insignificant effects on the current-voltage characteristics of $CuInSe_2$ in polyiodide were noted.

MORPHOLOGY AND COMPOSITION OF ETCHED SURFACES: Morphology of an etched $CuInSe_2$ surface is depicted by the scanning electron micrograph in figure 41. The pyramidal, faceted grains on an etched surface expose larger surface area on a microscopic scale, and specific surface orientation to the electrolyte, which might lead to more efficient and uniform conversion of $CuInSe_2$ to $CuISe_3$.

Figure 41. SEM of an etched (112) surface of n-$CuInSe_2$.

X-ray fluorescence analyses of the etched surface in figure 42 shows CuLα, SeLα, InLα, CuKα and CuKβ lines in a ratio characteristic of $CuInSe_2$ which is essentially unchanged from that of an untreated surface. The composition of the $CuInSe_2$ crystal was confirmed by XPS measurements No significant stoichiometric or compositional changes could be detected on etching within the sensitivity limits of XRF.

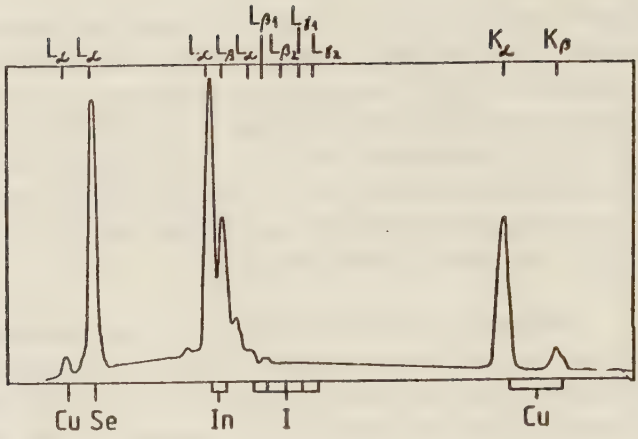

Figure 42. X-ray fluorescence analysis of $CuInSe_2$ after etching.

Results of photoluminescence experiments suggest that the machining damage of $CuInSe_2$ is extensive [74]. Therefore the observation that repeated etching and film growth cycles improve the I-V characteristics of $CuInSe_2$ electrodes may be explained as an effect of removal of residual machine damage. Because of the oxidative nature of the etchant and the exposure of the electrodes to air after etching, the electrode surface may be covered by a native oxide consisting of an outer layer of In_2O_3 and a transition layer of CuxSe of unknown stoichiometry [63,64]. Electrode passivity caused by In_2O_3 formation results in a slower rate of charge transfer kinetics at the foot of the curve III in figure 40. The effect of HI on the passivity of $CuInSe_2$ photoelectrodes suggests that the outer In_2O_3 layer is at least partially dissolved in the I^--I_2-Cu^+-HI electrolyte. Thus the $CuISe_3$ film formed upon exposure to the cell electrolyte nucleates on the remaining Cu_xSe transition layer.

Subsequent etches remove the $CuISe_3$ film. Both CuI and Se are soluble in KCN. Thus fresh layers of CuxSe and In_2O_3 are exposed to the electrolyte to form a new $CuISe_3$ layer.

Electrochemical conversion of $CuInSe_2$ to $CuISe_3$ by cyclic polarization in the I^--I_2-Cu^+-HI electrolyte is also a form of etching away of the surface imperfections. Continuous cycling thus leads to slow improvement of photocurrent-voltage output. The rate of conversion of the damaged $CuInSe_2$ layers is, however, be expected to be slower than that of converting freshly etched and appropriately oriented layers.

A maximum in the electrode performance versus the number of etches indicates a counterbalance of at least two different effects. While the removal of surface damage enhances the electrode behavior, surface roughness and inhomogeneity introduced by etching becomes more pronounced with repetitions and leads to te deterioration of the electrode performance. Increasing thickness of te In_2O_3 layer formed on etching may be a further kinetic impediment to the photooxidation reaction.

8.1.2. MECHANICAL POLISHING

When a sawn crystal surface is chemically etched, deep fissures may be propagated along the saw marks producing a highly irregular surface. The irregularities resulting from etching may be reduced if it is performed on an initially smooth surface.

For this purpose the sawn face of an <110> oriented $CuInSe_2$ sample A, was mechanically polished with diamond paste down to 0.3 um particle size to a mirror finish. Although this proceedure produced a smooth surface the work damaged layer had to be removed by chemical etching in the sequence described above. The same etching treatment was administered to another similiarly oriented but not polished sample B, having approximately the same surface area.

PHOTORESPONSE DEPENDENCE: The importance of the polishing step on the initial I-V outputs of two $CuInSe_2$ samples is shown in Figure 43. Although both surfaces received the same etching treatment, higher FF and Voc were realized for sample A. Lower reflectivity and larger exposed area of the sample B may contribute to the slightly higher Isc.

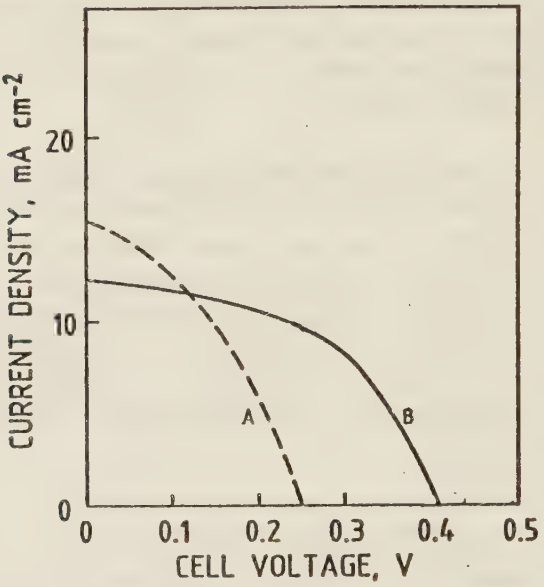

Figure 43. Influence of mechanical polishing on the initial photoresponse of n-$CuInSe_2$ in I^--I_2-Cu^+-HI solution.

MICROWAVE CONDUCTIVITY: Changes in the surface recombination centers with surface treatments were followed with microwave conductivity measurements. Figure 44 shows the response, on excitation with a 1060 nm laser pulse of 20 ns duration, of $CuInSe_2$ samples (I) cut and etched, (II) cut and polished and (III) etched after polishing. The signal decay

of an as cut sample was too fast to allow detection, indicating abundance of recombination sites. The less rapid decay (100ns) of the signal in curve I suggests partial reduction in recombination sites or introduction of band bending on etching. Relatively lower absorption intensity of curve II may arise due to reflection losses from a highly polished surface. The kinetics of decay are slower implying increased carrier lifetimes attributable to a more efficient separation or to the unavailability of recombination sites. The signal amplitude in curve III increases ~5-fold. Here the mechanical damage is removed by polishing and reflection losses are eliminated by etching resulting in the generation of larger number of carriers with longer lifetimes.

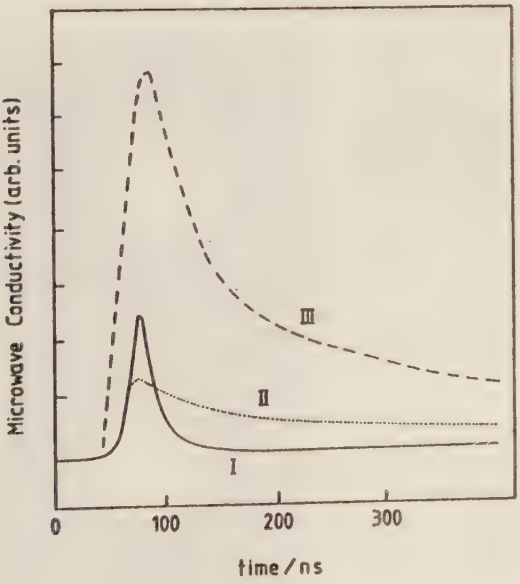

Figure 44. Excess microwave conductivity response on illumination with 1060 nm laser pulse in a n-$CuInSe_2$ crystal (I) etched, (II) polished and (III) polished and etched.

8.2 EFFECTS OF CRYSTALLOGRAPHIC ORIENTATION

Surface orientation tends to affect barrier heights particularly in polar solids where the interface states may vary with the exposed crytal face. The influence of crystal orientation on the photoresponse of the cell is examined.

IDENTIFICATION: The boules were oriented using the X-ray back reflection technique and then cut into ~2mm thick slices along (110) and (112) planes using a diamond saw with large area faces perpendicular to the c-axis. Figure 45a shows a crystal bar with long axis ⟨110⟩ and figures 45b and 45c show Laue X-ray photographs taken on the perpendicular (110) and (112) faces.

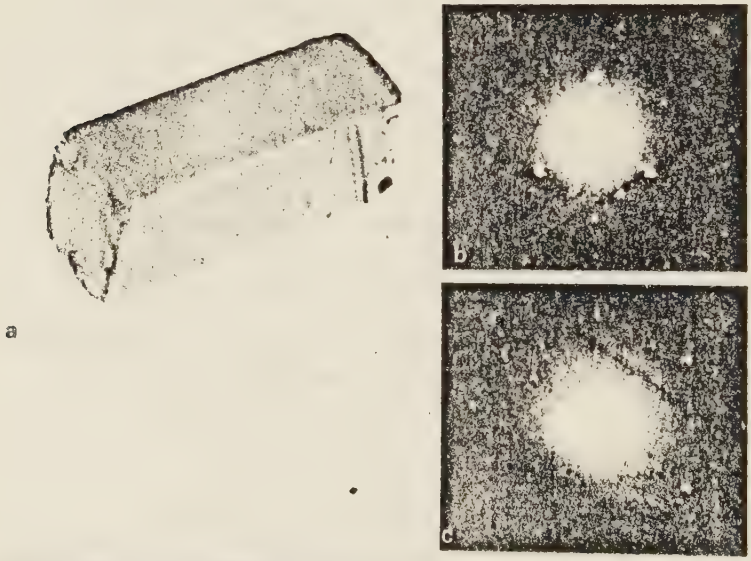

Figure 45. (a) $CuInSe_2$ single crystal bar, long axis ⟨110⟩. (b), (c) Laue back reflection photograghs of the (112) and (110) faces.

TABLE II

(hkl)	Isc	Voc	FF	n
(110)	1.00	1.00	1.00	1.00
(112)	1.01	1.00	1.00	1.01
(112)*	0.99	1.02	0.89	0.90
Random	0.89	0.90	1.04	0.84

* Opposite polar face

PHOTORESPONSE: Electrodes were fabricated from 4 different orientations, the (110), (112)A, (112)B and random face of n-$CuInSe_2$ single crystal. Surface preparation involved lapping with wet Linde B powder, followed by the etching and cycling sequences described above. To determine the effect of the orientations photocurrent-voltage output of similiarly treated electrodes was measured under a constant, AM1 illumination. Table 1 shows the relative Isc, FF, Voc and n for the four isolated crystal faces cut from the same crystal relative to the (110) face that was chosen as a reference. We note that the difference in efficiency for the various crystallographic surfaces is within 15%. This relatively small change in efficiency is within experimental error and suggests that the efficiency of polycrystalline electrodes should be insensitive to their texture.

Although the same $CuISe_3$-Se film appears to grow on the different faces, the orientation could affect the rate of growth and the homogeneity of the layer. The (112) face is a polar face exposing either Cu and In or Se atoms. The (110) face exposes all three elements simultaneously. The lateral proximity of Cu and Se ions in the Cu_xSe layer may lead to a more uniform conversion to CuI and Se which then react to generate the $CuISe_3$ layer. More reproducible output and better fill factors were observed on the (110) face which is, therefore, employed in subsequent efficiency measurements.

8.3. CONCENTRATION DEPENDANCE OF ELECTROLYTE CONSTITUENTS

The role of Cu^+ as a stabilizer and of HI in improving the interface kinetics is evident from figure 30. To improve the cell performance it is essential to determine the optimum electrolyte composition paticularly the effects of Cu^+ and HI concentrations efficiency and stability.

8.3.1. [Cu^+] DEPENDENCE

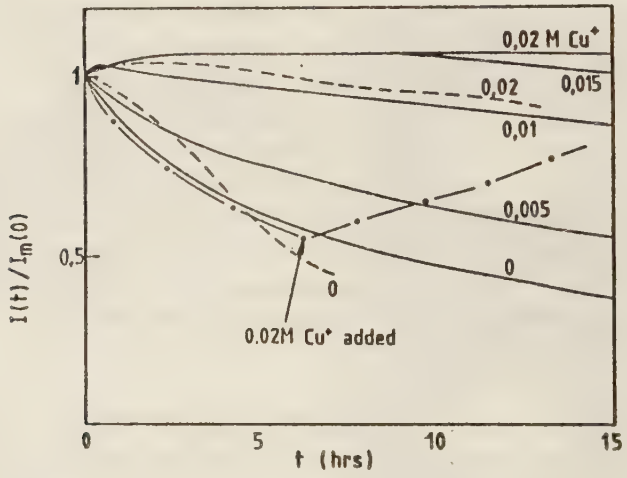

Figure 46. (a) Relative photocurrent at the maximum power point Im(t)/Im(0) as a function of time t of continuous operation under AM1 illumination. Solid curves in 1M CaI_2 + 50mM I_2 + 2.5M HI, dashed curves in 2M CaI_2 + 50mM I_2, with CuI additions indicated, dash dotted curve, in 1M CaI_2 + 50mM I_2 + 2.5M HI, with 20mM CuI added as indicated.

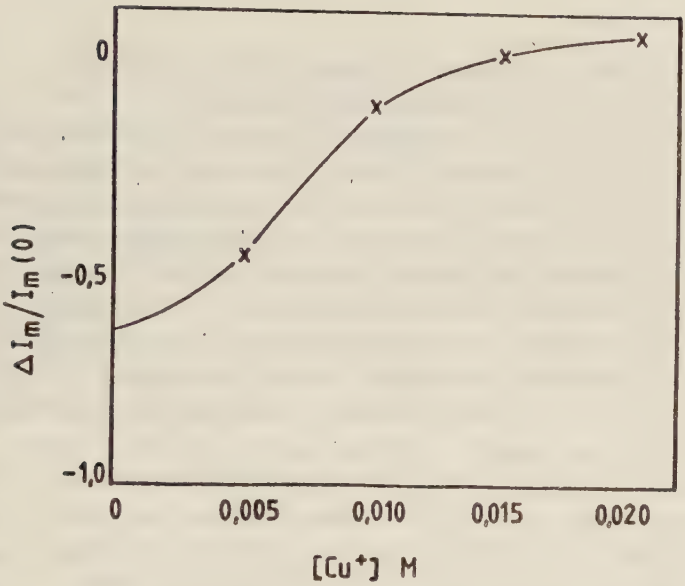

Figure 47. Change in the relative photocurrent, /\I/I, after 15 hours of continuous operation under AM1 illumination, as a function of Cu^+ concentration.

Figure 46 shows the relative photocurent of (112) oriented photoelectrodes at the maximum power point Im(t)/Im(0) as a function of time, of continuous operation under AM1 illumination. The electrode surfaces were renewed by etching away the film before each stability run to yield similar initial surface conditions and the same initial photocurrent output. The solid curves were obtained in 1M CaI_2 + 50mM I_2 + 2.5M HI and the dashed curves in 2M CaI_2 + 50mM I_2 with and without addition of CuI as indicated. From these curves, it is evident that the photocurrent output of $CuInSe_2$ in contact with the redox electrolyte without CuI declines rapidly to less than 50% of the initial value in 15 hours. Output stability improves with successive increments of CuI concentrations. In concordance with earlier observations, in figure 30, the initial photocurrent in solutions with and without Cu^+ ions is not significantly different. However,

the curves in figure 46 show that, while Isc, FF and Voc decrease in the electrolyte without Cu^+, these parameters paticularly the FF actually improve in the initial 2-3 hours. The increase in Im(t)/Im(0) represents improvements resulting from the growth of the $CuISe_3$ phase. This increase is retained for the 0.02M Cu^+ containing solution beyond the duration of measurement whereas at 0.015M Cu^+ level, the ratio of Im(t)/Im(0) drops back to 1 after 15 hours. The influence of Cu^+ addition to a deteriorating electrode is quite dramatically illustrated by the dash-dotted curve. In the absence of Cu^+ it follows the shape of the solid curve(0). Addition of 0.015M CuI after hours of photocorrosion reverses the slope of the curve. The slow increase indicates that the rate of conversion of a photocorroded surface to $CuISe_3$ is slower than on an etched surface. Similiar effects were also observed with the RRDE. The initial current voltage output of a well etched electrode in iodide solutions generally deteriorates on cycling, figure 19. with CuI addition to the solution it is possible to reverse these effects.

A comparison of the solid and dashed curves shows that the performance also degrades in the absence of HI. Cu^+ is however still effective in suppressing electrode degradation. The shapes of the two dashed curves and the decrease in Im even in the presence of 0.02M CuI suggest effects of increasing surface passsivity contributing to the deterioration. HI is one of the main ingredients in the hydrothermal synthesis of $CuISe_3$ [66]. Growth of CuISe3 film on the electrode in the absence of HI, thus appears unlikely. The solubility of the corrosion reaction products, CuI, Se and In_2O_3 decreases in the absence of HI. The passive film may comprise one or more of these products. Its thickness increases with time and probably slows down the kinetics at the electrode surface.

Figure 47 shows the change in the relative photocurrent $\Delta I/I$ after 15 hours of operation as a function of the CuI concentration in 1M CaI_2, 2.5M HI, 50mM I_2 electrolyte. The plot crosses zero with 15mM Cu^+. As seen in figure 46 this is due to the increase in Im during the film formation phase, in solutions containing $[Cu^+] > 0.015M$. The long term stability measurement shown in figure x indicates less than 5% decrease of the photocurrent after passage of 70,000 C/cm^2. Higher Cu^+ concentrations improve the stability. Therefore, Cu^+ concentrations have been increased to saturation level in all subsequent cell performence measurements.

8.3.2. [HI] DEPENDANCE

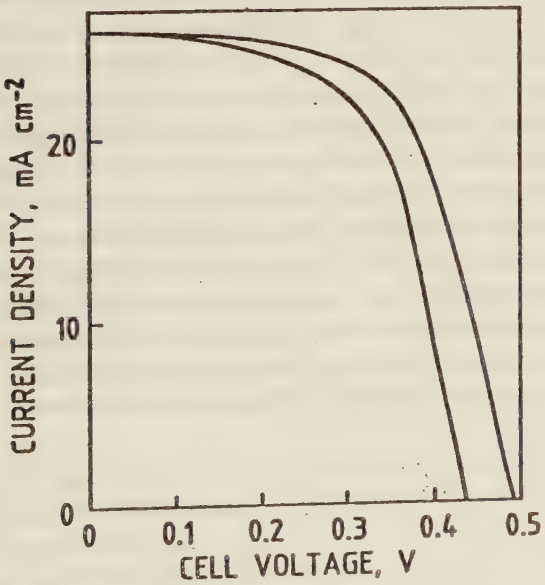

Figure 48. Current-voltage characteristics of an optimized n-$CuInSe_2$(110)/p-film electrode in I^--I_2-Cu^+ solution with (I) 2.5M HI and (II) 4M HI.

A high concentration of HI is essential to diminish hystheresis and improve I-V characteristics of the electrode, thus increasing the cell efficiency. This influence of HI on the initial I-V characteristics can be interpreted as inducing the growth of $CuISe_3$ while inhibiting the growth of other passive films. Figure 48 shows the effects of increasing HI concentration on the cell output after film formation and post growth heat treatments. Curve A represents the optimum output of an electrode, treated sequentially by mechanical polishing, brief chemical etch, photoelectrochemical film growth and an air anneal, in the cell electrolyte containing 2.5M HI. Increments in HI concentration of up to 4M improve both the FF and Voc leading to the characteristics of curve B.

No appreciable effects of similar variations in the concentrations of I^- or Cu^+, redox potentials, age of the electrolyte, exposure to nitrogen or air were discernible on the cell efficiency after film formation. Of course, all the ingredients and conditions are essential for the growth of the film and the Cu^+ ions are required to maintain the stability of the PEC cell. The major influence of the electrochemical environment on the efficiency comes from the solution pH. Thus a certain level of H^+ activity is required to maintain appropriate stoichiometry in the interphase. Alternatively, a lower pH may shift the band edges of the heterojunction at the film/electrolyte interface favorably, to reduce any small barriers to hole transport to the iodide species that might be present.

8.4 EFFECT OF AMBIENT TEMPERATURE

The semiconductor properties which determine the influence of temperature are the diffusion length the absorption coefficient and the intrinsic carrier density. In solid state solar cells, the effects of increasing temperature are seen as an increase in Isc and decreases in Voc, FF and n. The increase in Isc is partly due to improved lifetimes, which increase the base diffusion length, and partly due to the shift of the absorption edge to lower energies, both of which improve the long wavelength spectral response. The decrease in Voc is mostly because the intrinsic carrier density and hence the dark current increases with temperature. As a result of the decrease of Voc, partly offset by improvement in Isc, the FF and the n decrease with increasing temperature.

In most photoelectrochemical cells, Voc similiarly decreases due to increase in the forward dark current at higher temperature. However, since the rate of the photoelectrochemical reaction may be temperature dependent as well, additional increases may occur in the Isc and the n may also increase with temperature. This is the case where the electrochemical reaction rate constant cannot keep up with the supply of minority carriers at the surface or a product film forms at high current densities.

8.4.1. PHOTOCURRENT-VOLTAGE OUTPUT

The influence of temperature during the operation of the $n\text{-}CuInSe_2/p\text{-}CuISe_3\text{-}Se/I^-\text{-}I_2\text{-}Cu^+\text{-}HI/C$ cell has been examined. The illuminated cell was heated in a water bath. I-V plots obtained at various temperatures from 25-70^{o}C are shown in figure 50. The behavior at 25^{o}C is typical of samples that have not been optimized by the proceedures described above. The curves become increasingly steeper with rising temperature as Isc increases and

Voc decreases. To ensure the reversibility of these trends the solution was allowed to cool and I-V curves were again obtained at various temperatures. The Voc and Isc for this set of cooling down curves were comparable to those in figure 50, at respective temperatures. This set of curves, however, showed better FF.

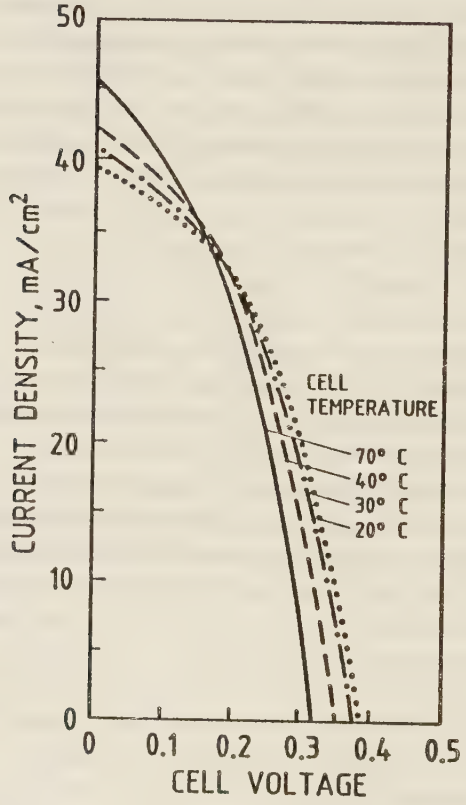

Figure 50. Current voltage curves for the $n\text{-}CuInSe_2/p\text{-}CuISe_3\text{-}Se/I^-\text{-}I_2\text{-}Cu^+\text{-}HI/C$ cell at different temperatures.

8.4.2 VARIATION IN THE PEC CELL PARAMETERS

To examine the temperature dependance more closely the relative variation in Voc, Isc, FF and n, normalized to the values at 25°C, with temperature are plotted in figure 51. The general trends observed for solid state p-n junctions [75] are evident. Isc increases by 20%. Several temperature dependant parameters (lifetime t, mobility u, absorption coefficient a, band gap Eg may contribute to this increase. Voc decreases by 16% between 25° and 70° as predicted by the expression,

$$Voc = Eg/q-(kT/q \ln[(D/t)^{1/2}T^3B/Jsc] \qquad (21)$$

where D represents the diffusion coefficient and B a relatively temperature independant terms [76]. Equation (21) suggests that extrapolation of experimental Voc could be used to estimate the effective barrier height for Shottky diode and the band gap(smaller) for heterojuntions. The extrapolation of the Voc data for $CuInSe_2$, from figure 51a, to 0° K yields a value of 0.8 eV as shown in figure 51b. The Voc in optimized cell is o.49 V at 25oC, figure 49 curve II. Assuming that the rate of increase in Voc is the same as that for the electrode employed in this experiment, of 1.4 eV/°C, yields an extrapolated value of Eg = 0.92 eV. Heterojunctions whose dark currents are determined mainly by thermal injection show decrease in Voc whereas those dominated by tunneling cause Voc to remain fairly constant with increasing temperature. The rates of decrease in Voc with temperature for GaAs and Si cells where thermal injection is the dominant mechanism of transport, range between 1.9 to 2.5 V/°C. Also the 0°K extrapolation overestimates the Eg by 5% for transport models that do not include tunneling. A lower rate of decrease as well as a lower estimation of Eg for the $CuInSe_2$ cell may indicate partial tunneling transport at least in the unannealed structure.

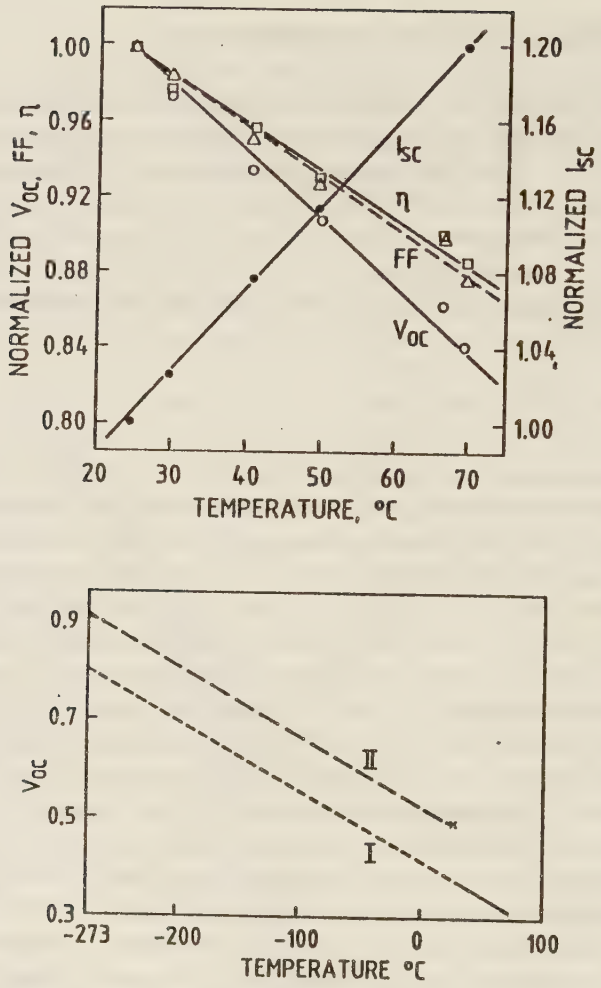

Figure 51.(a) Temperature dependance of the cell parameters during operation at AM1 intensities. Isc, Voc and FF and n are normalized to 25°C values.(b) I, Measured (solid) Voc variation with temperature extrapolated (dashed) to T = 0°K; II, Measured maximum RT value of Voc at AM1 (x) extrapolated (dashed) to T = 0°K.

The n and the FF decrease roughly by 12%. In contrast, previous investigations of $CuInS_2$ and $CuInSe_2$ in polysulfide cells under comparable illumination and temperatures indicate increases of 20% in the FF, 50% in the n and the Isc [33,34]. The dissolution of sulfur is the rate limiting step in the photooxidation of sulfide ions. Increasing the temperature leads to a more rapid dissolution of elemental sulfur and thus allows the chemical rates to keep up more readily with the minority carrier flux. This increases the Isc. Improved kinetics of the photoelectrochemical reaction decrease the relative effect of reconbination and therefore improve the shape of the I-V curve and hence the fill factor.

Similiar effects could be expected in the polyiodide electrolyte where iodine dissolution is also the rate limiting step. Evidence to the contrary indiates independence of the solar cell characteristics on the electrochemical kinetics. Two other considerations could explain the trends in figure 51a. First, the location of the principal barrier at the p-n solid interface may decrease the influence of the interfacial kinetics at the solid-electrolyte interface. Secondly, the kinetics of the $CuInSe_2$ surface in acidic and basic solutions vary considerably as seen by the different passivation characteristics in these media, figures 11 and 12. The sluggish interfacial kinetics in the polysulfide solution may result from the formation of a thick oxide or hydroxide film. A high concentration of H^+ is necessary to reduce the passity in the polyiodide cell. The abscense of this passive film in the 4M HI solutions may thus be responsible for the temperature effects observed.

8.5. POSTGROWTH FILM ANNEAL

SEM and X-ray diffraction reveal that the electrochemically grown $CuISe_3$-Se layer is polycrystalline. The individual crystallites have defined hexagonal symmetry but their random orientation and size, diameter ~5um and thickness < 1 um, suggest interruptions by numerous grain boundaries and voids. Grain boundaries represent regions of increased disorder with structural defects and seggregated impurities in large densities. Thus they are generally regions of increased recombination. In addition, charge trapping at the grain boundary energy levels can form potential barriers that impede carrrier transport.

Although the temperature effects on the current-voltage curves in figure 50 appear generally reversible a small degree of irreversibility was detected in the 'cooling' curves in terms of increased FF. Thus the photoelectrochemically generated p-n junction may benefit from heat treatments.Thermal annealing has been variously used to increase crystallite size, improve dopant homogeneity, remove lattice defects, induce chemical reaction between phases or oxidize surface components. Most of these effects involve removal of recombination sites which lead to increases in the effective lifetime and diffusion length. Several reports on polycrystalline solar cells claim improvements in Isc, Voc and FF as a result of thermal annealing.

8.5.1. INFLUENCE ON CURRENT-VOLTAGE BEHAVIOR

To determine the effects of heat treatment, photoelectrochemically grown $CuISe_3$-Se films, on $CuInSe_2$ substrates, described in section B were annealed in air for 15 minute periods at different temperatures. Effects of the annealing step were monitored by the I-V output of the electrodes in the I^--I_2-Cu^+-HI electrolyte, under constant illumination as a function of the annealing temperature and time and the pretreatment of the electrode surface.

FILM FORMED BY ECTH/GROWTH SEQUENCES: Typical behavior, on annealing, of a sample with a film grown via repeated etch/growth cycles, is shown in figure 52. Curve I represents I-V characteristics before annealing. The improvement after a 70^{o}C anneal is evident in curve II and enhanced after further annealing at 140^{o}C in curve III. The relative increments observed in the photovoltaic parameters, of 55% in Isc, 44% in Voc and 10% in FF were typical for initial annealing treatments. Improvements were relatively higher for samples deteriorated from excessive etching or other surface damage, and less for samples yielding reasonable initial output.

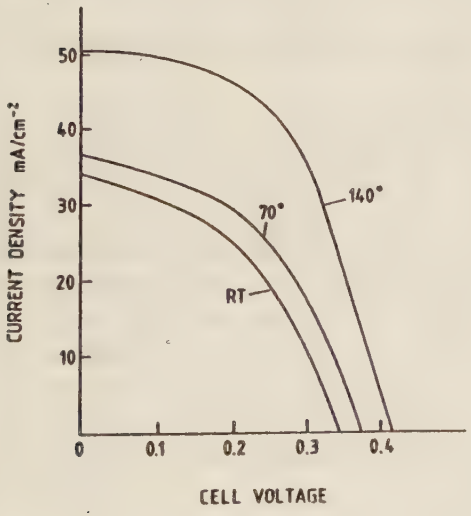

Figure 52. Influence of annealing on the performance of $CuISe_3$-Se film grown on $CuInSe_2$(112) face by etch/growth cycles in the I^--I_2-Cu^+-HI solution. (I) pre-anneal; after air anneal for 15 minutes at (II) 70^{o}C and (III) 140^{o}C.

FILM FORMED ON POLISHED SURFACES: As with etching extensive annealing can also be detrimental to the electrode performance. Figure 53 shows the annealing effects for a well polished and etched sample, with initial I-V characteristics of curve A $CuISe_3$ film grown on this surface by cycling in the I^--I_2-Cu^+-HI electrolyte, without intermediary etches was annealed for 10 min at 200°C. the output of this electrode, given by curve B, represents over 100% increase in Isc and 25% in Voc.

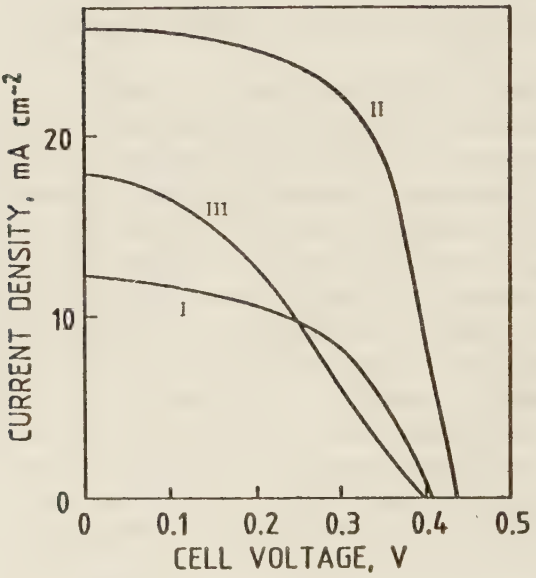

Figure 53. Effects of the duration of the annealing step, on the performance of $CuISe_3$-Se film grown on a polished n-$CuInSe_2$ (110) face. (I) pre-anneal; air anneal at 200°C for (II) 10 min and (III) 30 min.

Thus it is possible to attain optimal electrode behavior without resorting to the less reproducible etch/growth sequences with better surface preparation and annealing. Curve III shows the effects of prolonged heat treatment, additional 30 min anneal at 200^{o}C, leading to the degradation in the I-V output. Adverse effects of annealing such as removal of volatile components, phase segregation, which increase recombination centers and cause degradation in the photovoltaic behavior have also been noted before. The degration of the p-film is, fortunately not irreversible. The output of curve II could be recovered by potentiostatic cycling of the electrode or by leaving it immersed in the electrolyte for several hours. This implies that the $CuInSe_2$ substrate is unaffected by annealing and the film is reconstructed on exposure to the electrolyte.

8.5.2. MORPHOLOGY AND COMPOSITION OF ANNEALED SURFACES

Dependance of the cell parameters on the annealing step imply compositional and structural alterations in the interphase. The role of the annealing step was investigated with SEM, XRF and XPS. SEM and XRF methods were used for morphological and compositional characterization of large surfaces (1 mm^2 area) as well as individual crystallites comprising the film. Electrodes with film were examined under 3 different conditions: (I) unannealed (II) annealed and (III) annealed and exposed to the cell electrolyte. The results were compared and supplemented with XPS, which provides information on the oxidation states of the constituents, higher surface sensitivity but less lateral resolution.

SEM and XRF ANALYSIS: Several new structures and phases as well as restructing of the unannealed cystallites are observed on annealing. Some representative structures are displayed by the SEM pictures in figures 54, 56 and 58 and their composition is given by the XRF traces in figures 55, 57 and 59.

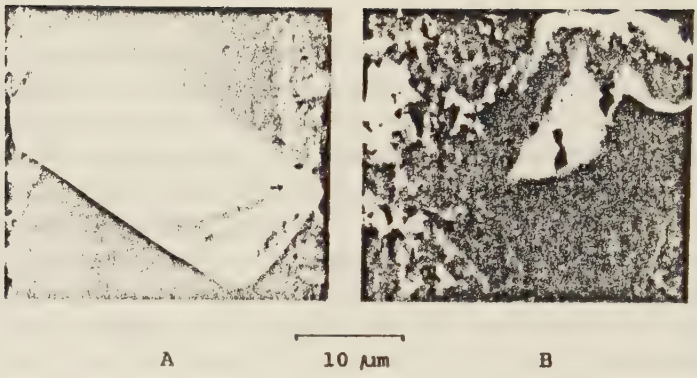

Figure 54. SEM on CuInSe2/film surfaces after air anneal.

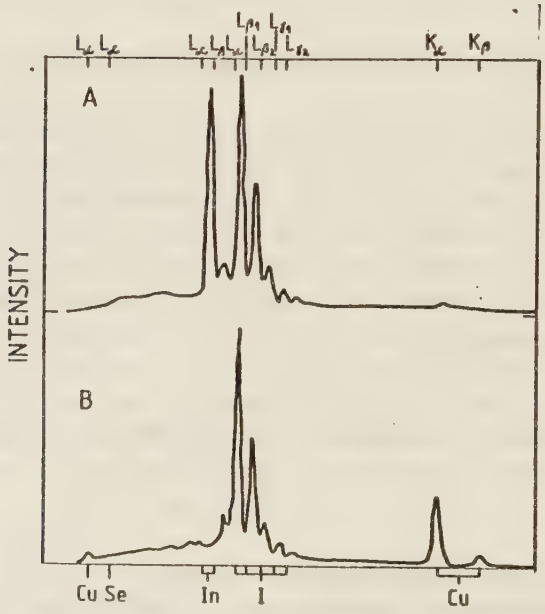

Figure 55. XRF analysis of binary structures shown in figure 54. Trace A represents the dark rectangular or triangular crystallites in SEM 54A and trace B to the structures in SEM 54B.

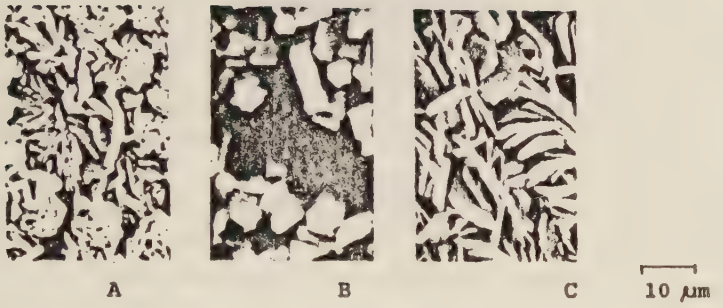

Figure 56. SEM of ternary structures formed on (A) type I and III electrodes, (B) type II and III electrodes and (C) type III electrodes.

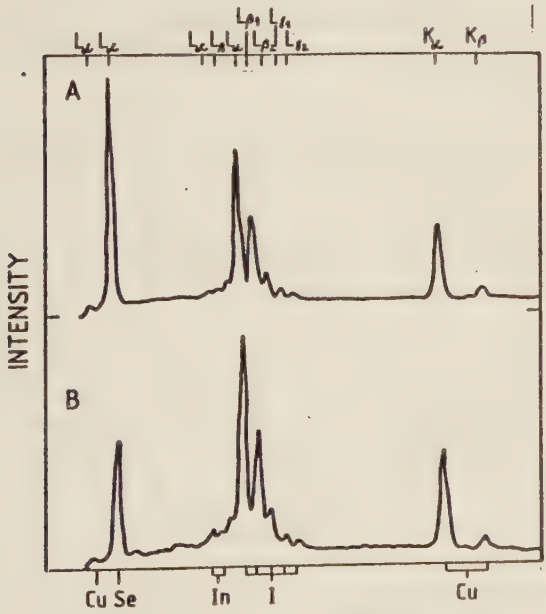

Figure 57. XRF analysis of (A) hegagonal platelets or columnar structures in SEM 56 A and B and (C) clusters in SEM 56C.

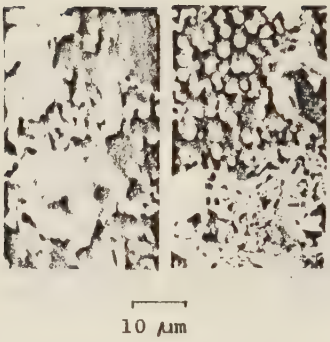

Figure 58. SEM of ternary and quarternary structures on type III surfaces.

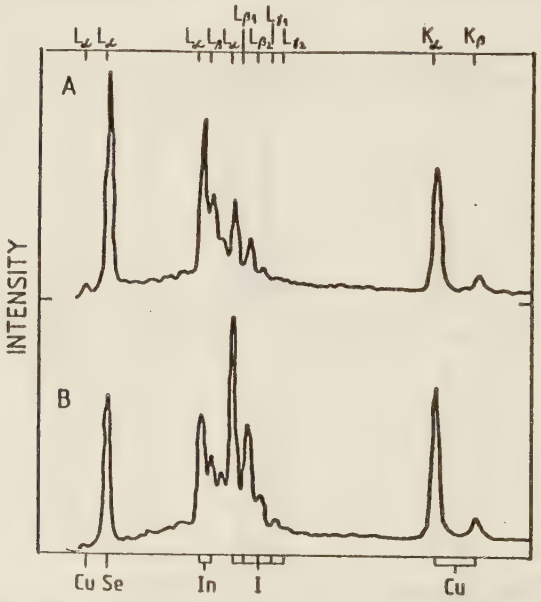

Figure 59. XRF of structures shown in SEM of figure 58.

Elemental Se: Samples in the category II and III were notably devoid of any elemental Se. Hexagonal and rhombic crystallites of Se interspread between $CuISe_3$ crystals were present on type I electrodes.

Binary structures: These were inhomogeneously distributed on type II surfaces. Large, dark rectangular crystals, as shown in figure 54A were seen randomly protruding from the electrode surface. Clusters of smaller triangular crystallites, resembling those on the corroded electrolytes of figure 23, are found in the viscinity. XRF analysis of both types of structures is given by the trace A in figure 55, which shows the Ka and Kb Cu lines and La, Lb and Lg I lines. These lines compare with a CuI standard in figure 23. A Ca peak sometimes detected for the larger crystals, is probablly an impurity.

In and I composites were found on type II and III samples in various shapes and sizes shown in figure 54B. All these structures yield similiar composition and and stoichiometry, as shown by the La, Lb and Lg In lines and the La, Lb and Lg I lines in figure 55B. No binary compounds of Se^{2-} were detected.

Ternary structures: Three structural variations of the ternary composite of Cu, I and Se detected in the various specimens are displayed by the SEM pictures in figure 56. The hexagonal platelets constitute the film in sample A. A major fraction of these platelets have the composition shown by the XRF trace of figure 57A. The Cu, I and Se lines and the relative peak heights correspond to those observed in f-igure 32C for $CuISe_3$. These lines and the peak heights remain unchanged for the hexagonal columnar structures, seen in figure 56B, found on type II and III samples, indicating that the nearly flat platelets undergo restructuring. The clusters of platelets, shown in figure 56C were found on type III samples and are analyzed by the XRF trace in figure 57B. The Cu, I and Se lines are the same as in trace 57A, but the height of the Se peak is relatively lower(~50%). Similiar structures yielding the analysis of figure 57B were found in the films grown in the dark. The change in stoichiometry may be caused by insufficiency of accessible Se to produce $CuISe_3$. The compound is quite likely CuISe [67]. Alternatively the higher Se peak in trace 57A could arise from combined signals from overlapping Se and $CuISe_3$ crystals.

No evidence of $CuInSe_2$ substrate exposure or recrystallization was detected on any of the type I, II or III surfaces.

Quarternary Structures: Crystallites comprising Cu, In, I and Se were found on type III samples and appear to occur in several stoichiometries. Two predominant structures shown by the SEM of figure 58 yield XRF traces of figure 59. The difference between the two stoichiometries appears mainly in their Se and I content.

COMPOSITION OF QUARTERNARIES: In an attempt to identify the stoichiometry of the quarternary compounds, various structures on type III samples comprising Cu, In, I and Se were quantitatively analyzed using the necessary standards. The relative compositions are summarized in Table III.

TABLE III

Spot No.	Cu	In	I	Se
1	0.09	0.14	1.00	0.43
2	0.23	0.33	0.68	1.00
3	0.30	0.37	0.57	1.00
4	0.30	0.17	0.30	1.00
5	0.20	0.28	0.39	1.00
6	0.13	0.29	1.00	0.26
7	0.07	0.25	1.00	0.17
8	0.65	0.23	1.00	0.68
9	0.58	0.25	0.17	1.00
10	0.23	0.31	1.00	0.70

The data in table III implies that quantitative analysis of the quarternaries is not as straightforward as the $CuISe_3$-Se phase. Considerable variation in composition observed with either I and Se being the dominant species suggests some overlap of structures. The fluctuations in the stoichiometric compositions in Table III indicate lateral inhomogeneity across the surface of the sample.

XPS ANALYSIS: XPS was used to supplement XRF results because of its surface sensitivity. XPS spectra of three types of films (I) unannealed, (II) annealed and post anneal electrolyte treatment were compared. The Se, In, I and Cu peak positions for film I are in accord with the data in Table I for the sample with film. Annealed sample II shows large enhancement of iodide signal and total depletion of selenium in either oxidation states. The Se lines reappear for sample III but at lower intensities than in film I. These results confirm the XRF analysis. The oxidation states of the four film constituents remain unchanged from the unannealed film.

8.6 TRANSFORMATION OF $CuISe_3$-Se LAYER TO $CuIn_xI_ySe_z$

ANNEALED SURFACES: A counter balance of several effects of the annealing treatment is evident from the above results. SEM of the sample employed in stability measurements, shown in figure 23, indicates that film growth ceases after about 2 micron thickness. Annealing permits an increased mobility condition in the solid film phase after film growth without access to the electrolyte constituents. The major outcome of the increased mobility is obviously volatilization of Se and the diffusion of In from the substrate into the film. As a consequence, a host of new compounds and structures have been generated in the interphase. Absence of Se and formation of CuI and CuISe attest the removal of Se by the heat treatment. In ions diffusing from the substrate react with I^- ions to form InI_3. Restructuring of $CuISe_3$ into larger columnar structures may decrease the grain boundaries to some extent.

POST ANNEAL ELECTROLYTE EXPOSED SURFACES: Potentiostatic cycling in the cell electrolyte restores Se in the film. As discussed earlier Se is indirectly photogenerated by the reaction of photooxidized I_2 with Se^{2-} ions from the $CuInSe_2$ lattice. Film on type II surfaces have scarcity of elemental Se because of difficult access to the substrate compared to the freshly etched $CuInSe_2$ surfaces where large surface areas are exposed to the electrolyte. This may lead to the formation of quarternary compounds and CuISe rather than $CuISe_3$. The situation is quite similar to the film grown in the dark. In the absense of photooxidized I_2, the oxidation of Se^{2-} ions is slow or inhibited. Formation of quartenaries is, however, an intermediary step in the conversion of the $CuInSe_2$ surface to $CuISe_3$. The probability and rate of conversion thus depends on the various factors of surface condition, photocurrent and electrolytic environment.

Comparison of XRF traces yielding quarternary compositions in Figs. 33 A1, A2, B2 and 59 A, B, show excess Se in traces 33 A1 and A2. This difference appears to be not in stoichiometry of the quarternaries but rather in the absence of elemental Se phase in traces 33 B2, 59 A and B. This Se deficiency is caused by scarcity of I_2 to oxidise Se_{2-} ions from $CuInSe_2$ in trace 33 B2 and by inaccessiblility of the lattice Se^{2-} ions due to intervening layer in the samples of traces 59 A and B.

Reaction of stoichiometric quantities of In_2Se_3 and CuI at High temperatures leads to he synthesis of a dark metallic crystalline quarternary with composition of $CuIn_2Se_3I$ [77]. This compound cystallizes in a cubic zinc-blend type structure and has a lattice constant, a = 5.75 A^o matching closely with that of $CuInSe_2$ (a = 5.85 A^o) and is thus a likely constituent of the film on sample III.

8.7 PERFORMANCE OF $n\text{-}CuInSe_2/p\text{-}CuISe_3\text{-}CuIn_2ISe_3/I^-\text{-}I_2\text{-}Cu^+\text{-}HI/C$ CELL

The comparative studies of surface treatments, concentration dependence, crystallographic orientation, temperature and annealing effects were aimed at optimizing the solar conversion efficiency of the $n\text{-}CuInSe_2/p\text{-}CuISe_3\text{-}Se$ electrochemically contacted heterojunction. Based on the results of these studies the following modifications were incorporated in the junction fabrication proceedure:

(i) The repeated ecthing/film formation sequences employed were eliminated as adverse effects of this proceedure became evident and and pronounced after 3-4 repetitions. An initial prepolishing/etch step, corresponding to the surface conditions of figures 43A and 44(III), was introduced instead.

(ii) The (110) face of $CuInSe_2$ was exposed to the electrolyte.

(iii) The HI concentration was increased to 4M and CuI concentration to saturation to yield an electrolyte with composition of 1M CaI_2 + 50mM I_2 + sat CuI + 4M HI.

(iv) The film, grown photoelectrochemically in the above electrolyte, was annealed in air at 200°C for 10 minutes.

Typical performance of the heterojunction incorporating the above modifications in the interphase growth procedure is shown in figure 60. At 100 mW/cm^2 simulated insolation, the cell delivers 12.17 mW/cm^2 at the maximum power point. The open circuit voltage is 0.49 V and the short circuit current is 40 mA/cm^2 and the fill factor = 0.62 leading to a solar to electrical conversion efficiency of 12.2% for an electrode area of 21 mm^2.

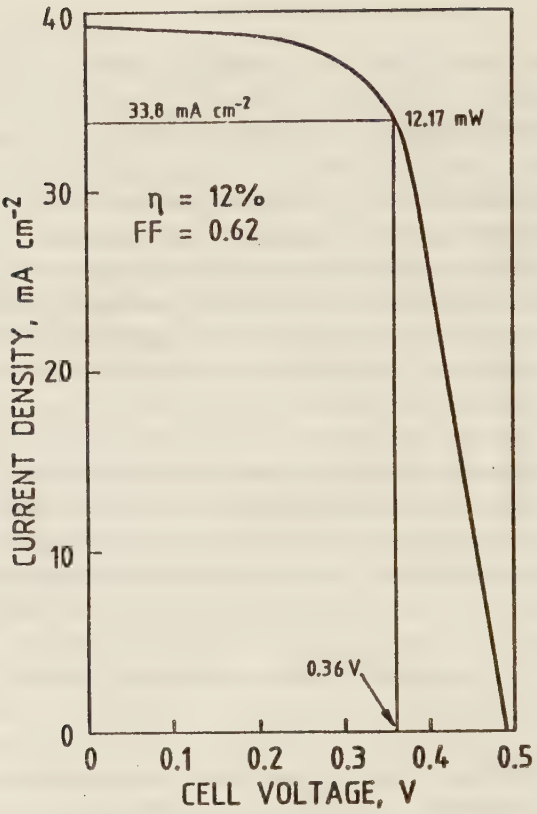

Figure 60. Output power characteristics of the n-$CuInSe_2$/p-$CuISe_3$-$CuIn_2ISe_3$/I^--I_2-Cu^+-HI/C cell.

Short term stability tests show no degradation in the current output at the maximum power point. Also no appreciable effects of small variations in the concentration of iodide, CuI, redox potential or age of the electrolyte, exposure of the cell to air or nitrogen were discernible after film formation. The lateral inhomogeneities in the film apparently are not detrimental to the performance of the cell. The near perfect match between the lattice constants of $CuInSe_2$ and $CuIn_2Se_3I$ may reduce interface states in the heterojunction and contribute to the improvement in efficiency.

SUMMARY

Semiconductor corrosion continues to be the major limitation of photoelectrochemical(PEC) cells. Under certain circumstances, insoluble(A) or soluble(B) products of a corrosion reaction may be utilized to form an interfacial film in-situ, which in turn can reduce recombination sites, avert further decomposition and direct the reaction path into the regenerative mode.

The probability of film formation and the nature of the film formed depends on the surface chemistry between the semiconductor and the electrolyte, hence on their constituents, the electrolyte pH, composition and the potential region of film growth. By adjusting these parameters, a tunneling oxide is formed at the InP/HCl interface whereas a metal film has to be interposed, to control the oxide growth at the GaAs/acetate interface. GaInPAs exhibits the film formation tendencies of InP. Its behavior in the presence of redox couples approaches that of GaAs.

Interfacial processes at $CuInSe_2$ are unravelled with an illuminated rotating ring-$CuInSe_2$ disk electrode while the surface transformations are monitored with SEM, XRF, XPS, UPS and XRD. Figure 61 outlines the formation and properties of various interphases between $CuInSe_2$ and the respective electrolytes. Films formed on $CuInSe_2$ also exhibit a strong pH dependance.

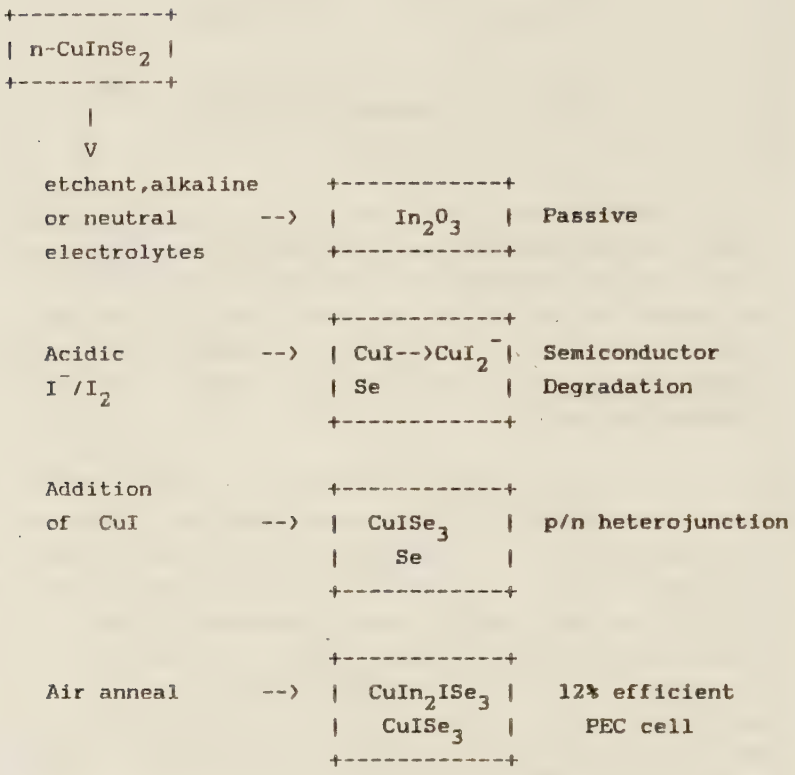

Figure 61. Schematic representation of interphase transformations.

Formation of porous, oxides which eventually grow thick hindering both mass and charge transport are responsible for the low efficiencies in the polysulfide, pH 14, electrolyte. Similar films formed in neutral solutions contribute to the sluggish charge transfer kinetics and cathodic passivation in neutral polyiodide solutions. Surface passivity is reduced in the presence of HI resulting in efficient photooxidation of I^-.

Unfortunately, the cell output degrades rapidly via concurrent reactions of iodide and photogenerated iodine with Cu^{+} and Se^{2-} ions from the $CuInSe_2$ lattice to generate triangular CuI crystallites and elemental Se, respectively, on the corroded surface. CuI dissolves partially via CuI_2^- formation. This system represents case (B) where the higher solubility of corrosion products leading to semiconductor degradation.

On addition of CuI to the electrolyte, its dissolution from the semiconductor surface is inhibited. Instead, the CuI reacts with Se on the surface, the photons providing the free energy, to generate a new interphase comprising of hexagonal $CuISe_3$-Se crystallites. Under illumination this film mediates efficient charge transfer between the $CuInSe_2$ and the electrolyte while inhibiting corrosion and does not grow beyond ~2 microns even after extended (70,000 C/cm^2) stability tests. This photoelectrochemically synthesized interphase comprises mainly CuISe3 and upto 30% Se, and exhibits p-type conductivity. Correlation of the energy levels of n-$CuInSe_2$, p-$CuISe_3$-Se film and the electrolyte suggests that the principal barrier is located in the solid p-n heterojunction with the electrolyte providing the front contact.

Restructuring of the film by modifying the growth conditions, which include the use of prepolished n-$CuInSe_2$ (110) surfaces, higher concentration of HI and CuI during film growth and a post growth air anneal, increased the cell efficiency to 12%. Major effect of annealing are volatilization of Se and diffusion of In from the substrate into the film resulting in formation of a host of new structures comprising of Cu and I or In and I, and hexagonal columns of $CuISe_3$. Exposure of the annealed surface to the electrolyte leads to further transformations generating quarternary composites of Cu, In, I and Se with different stoichiometries and $CuISe_3$. The system continues to be stable and relatively insensitive to small variations in the concentration

of electrolyte components. Although n-$CuInSe_2$ is the principal light absorber,a decrease of interfacial states on annealing and better lattice match of $CuInSe_2$ with the quartenary ($CuIn_2Se_3I$) may contribute to the higher cell efficiency.

Thus, by controlling the growth conditions, interfacial films may be formed, transformed or restructured to generate efficient and stable PEC cells or p-n heterojunctions. Detailed knowledge of the surface chemistry of other semiconductors could enable the extension of this proccedure to other systems.

REFERENCES

1. 'Semiconductor Liquid Junction Solar Cells', A. Heller, ed, The Electrochem. Soc.,Inc.: Princeton , NJ, 1977.
2. H. Gerischer, 'Phys. Chem. - An Adv. Treatrise', H. Eyring, D. Anderson and W. Jost, ed., p. 463, Academic press, NY, 1970; Electroanal. Chem Interf. Chem.,58, 263 (1975).
3. S. R. Morrison, 'Electrochemistry at Semiconductor and Oxidised Metal Electrodes', Plenum, NY, 1980.
4. R. H. Wilson, in Ref.1, p.67; CRC, Critical Rev. in Solid State and Mat.Sci., p.1 (1980).
5. R. Memming, 'Electro. Anal. Chem..', A. J. Bard, Ed., Marcel Decker, NY, p.1 (1974); Electroanal. Chem., 11, 1 (1979).
6. A. J. Bard and M. S. Wrighton, J. Electrochem. Soc., 124, 1706 (1977).
7. H. Gerischer, J. Electrochem. Soc., 82, 133 (1977).
8. K. C. Chang, A. Heller, B. Schwartz, S. Menezes and B. Miller, Science, 196, 1097 (1977).
9. B. A. Parkinson, A. Heller and B. Miller, J. Electrochem.Soc., 126, 954 (1979).
10. H. Tributsch, Ber. Bunsenges Phys. Chem., 82, 361 (1977); 82, 169 (1978).
11. J. Gobrecht, H. Tributsch and H. Gerischer, J. Electrochem. Soc., 102, 1817 (1980).
12. G. Kline, K. Kam, D. Camfield and B. A. Parkinson, Solar Energy Materials, 4, 301, (1981).
13. S. Menezes, L.F. Schneemeyer and H. J. Lewerenz, Appl. Phys. Lett., 38, 948 (1981).
14. H. J. Lewerenz, A. Heller and F. J. DiSalvo, J. Am. Chem. Soc., 102, 1817 (1980).
15. A. Heller, B. Miller, H. J. Lewerenz and K. J. Bachmann, Am. Chem. Soc., 102, (1980).

16. P. A. Kohl, and A. J. Bard, J. Electrochem. Soc., 126, 603 (1979); D. Laser and A. J. Bard, J. Phys. Chem., 80, 459 (1976).
17. K. D. Legg, A. B. Ellis, J. M. Bolts and M. S. Wrighton, Proc. Nat. Acad. Sci., USA, 74, 4116 (1977).
18. H. Gerischer, Photochem, Photobiol., 10, 243, (1972).
19. M. Gleria and R. Memming, Z. Phys. Chem., 198, 303 (1975).
20. Y. Nakato, T. Ohnishi and H. Tsubomura, Chem. Lett., 833 (1975); Y. Nakato, K. Abe and H. Tsubomura, Ber. Bunsenges Phys. Chem. 80, 1000 (1976).
21. S. Menezes, A. Heller and B. Miller J. Electrochem. Soc., 127, 1268 (1977).
22. R. Noufi., A.J. Frank and A. J. Nozik, J. Am. Chem. Soc.,
23. S. Gourgaud and D. Eliot, J. Electrochem. Soc. 124, 102 (1977); M. Tomkiewicz and J. M. Woodall, J. Electrochem. Soc.,
24. A. B. Bocarsly, E. G. Walton and M. S. Wrighton, J. Am. Chem. Soc., 102, B390 (1980); M. S. Wrighton, J. M. Bolts, A. B. Bocarsly, M. C. Palazzoto and E. G. Walton, J. Vac. Sci. Tech., 15, 1429 (1978).
25 P. R. Moses, L. Wier and R. W. Murray, Anal. Chem., 47, 1882 (1975).
26. S. Menezes, B. Miller and K. J. Bachmann, J.Vac. Sci. Tech., Bi, 48 (1983).
27. A. Heller, G. P. Schwartz, R. G. Vadimsky, S. Menezes and B. Miller, J. Electrochem.Soc., 125, 1156 (1978).
28. S. Menezes and B. Miller, J. Electrochem. Soc., 130, 517 (1983).
29. S. Menezes, H. J. Lewerenz, F. A. Thiel and K. J. Bachmann, Appl.Phys. Lett., 38, 710 (1981).
30. A. Fahrenbruch and R. H. Bube, 'Fundamentals of Solar Cells', Acad. Press, NY, 1983, 417.
31. J. L. Shay, S. Wagner and H. M. Kasper, Appl. Phys. Lett., 27, 87 (1975).
32. R. A. Michelson and W. s. Chen, Proc. 15th IEEE Photovoltaic Special. Conf., 800 (1981).

33. M. B. Robbins, K. J. Bachmann, V. G. Lambrecht, F. A. Thiel, J. Thomson Jr., R. G. Vadimsky, S. Menezes, A. Heller and B. Miller, J. Electrochem. Soc., 125, 831(1978).
34. Y. Mirovsky, D. Cahen, G. Hodes, R. Tenne and W. Giriat, Solar Energy Mater., 4, 169(1981); Y. Mirovsky and D. Cahen, Appl. Phys. Lett., 40, 727 (1982).
35. V. G. Levich, Physicochemical Hydrodynamics', Prentice Hall, Englewood, N. J. 1962.
36. Yu. V. Pleskov and V. Yu. Filinovskii,'The Rotating Disk Electrode', Consultants Bureau, N. Y. 1976.
37. S. Bruckenstein and B. Miller, Acc. Chem. Res., 10, 54 (1977).
38. W. J. Albery and M. L. Hitchmann, 'Ring-Disk Electrodes', Oxford Univ. Press, London, 1971.
39. B. Miller, S. Menezes and A. Heller, J. Electrochem. Soc., 126, 1483 (1979).
40. Bruckenstein and B. Miller, J. Electrochem. Soc. (1982).
41. W. J. Albery and S. Bruckenstein, Trans. Faraday Soc.,62, 1920 (1966).
42. K. J. Bachmann, M. Fearheily, Y. H. Shing, and N. Tran, Appl. Phys. Lett.,(in press).
43. K. J. Bachmann and F. A. Thiel grew the p-CuInSe2 and GaInAsP polycrystalline material.
44. M. Kunst and H. Tributsch, J. Electrochem. Soc. (1984).
45. K. K. Nj and H. C. card, IEEE Trans. Electronic Devices, ED-27. 716(1980).
46. J. Shewchun, D. Birk and M. B. Spilzer, IEEE Trans. Electronic Devices, ED-27, 705 (1980).
47. H. J. Lewerenz, D. E. Aspnes,B. Miller, D. L. Malm and A. Heller, J. Am. Chem. Soc., 104, 25 (1982).
48. H. H. Wieder, J. Vac. Sci. Tech., 15, 1498 (1978).
49. R. Memming, J. Electrochem. Soc. , 125, 117 (1978).
50. K. W. Frese Jr., M. J. Madou and S. R.Morrison, J. Phys. Chem., 84, 3172 (1980).

51. P. G. Desideri, L. Lepri and D. Heimler, in 'Encyclopedia of Electrochemistry of elements', A. J. Bard, Ed.,p. 91.
52. P. Beran and S. Bruckenstein, Anal. Chem., 40, 1044 (1968).
53. D. C. Johnson, J. Electrochem. Soc., 119, 331 (1972).
54. S. Wagner, Electrochem. Soc. Photovoltaics Symp. Series, 410, (1984).
55. U. Bertocci, D. R. Turner,"Encyclopedia of electrochemistry of elements"
56. G. W. Tindall and S. Bruckenstein, Anal. Chem., 40, 1051 (1968).
57. B. Miller, J. Electrochem. Soc., 116, 1675 (1969).
58. A. G. Casey, Comprehensive Inorganic Chem., , 17 (1973).
59. A. J. De Bethune, T. S. Licht and N. Swendeman, J. Electrochem. Soc., 106, 616 (1959).
60. R. F. Rolsten,'Iodide Metals and Metal Iodides', Electrochem. Soc. Series, Wiley, NY, 194 (1961).
61. W. M. Latimer, Oxidation potentials, 2nd ed, Prentice Hall, NY, 186 (1952).
62. Powder Diffraction Files, inorganic Phases, ICPDS (1981).
63. L. L. Kazmerski, P. J. Ireland, O. Jamjoum, S. K. Deb, P. Sheldon, R. A. Michelsen, W. Chen and K. J. Bachmann, in: 15th IEEE Photovoltaic Specialists Conf. record, denver, CO. 1981,p 247.
64. L. L. Kazmerski, P. F. Russel, O.Jamjoum, R. J. matson, R. Ehrenkiehl, P. J. Ireland, R. A. Michelson, W. Chen and K. J. Bachmann, in: 16th IEEE Photovoltaic Specielists Conf. Reccord, San Diego, CA, 1982.
65. O. Jamjou, L.L. Kazmerski, D. L. Lichtman and K. J. Bachmann, Surface Interface Anal. 4, 227 (1982)
66. A. Rabenau, H. Rau, G. Rosenstein, Z. Anorg. Allgem. Chem., 374, 43 (1970).
67. A. Rabenau and H. Rau, Solid State Commun., 1, 1281 (1969).
68. W. H. Strehlow and E. L. Cook, J. Phys. Chem. Ref. Data, 2, 183 (1973).

69. Y. R. Hsiao, W. S. Chen, R. A. Michelsen, J. M.Stewart, V. Lowe, L. C. Olsen and A. Rothwarf, CuInSe2/CdS Thin Film Solar Cell Development, Final Report, boeing Aerospace Company, Seattle, WA, May 1983.

70. H. Neumann, N. Van Nam, H. J. Hobler and G. Kuhn, Solid State Commun., 25, 899 (1978).

71. T. Irie, S. Endo and S. Kimura, Japan. J. Appl. Phys,18, 1303 (1979).

72. K. J. Bachmann, E. Buehler, j. C. Shay and S. Wagner, Appl. Phys Lett, 29, 121 (1976).

73. R. Gomer, G. Tryson, J. Chem. Phys., 66, 4413 (1977).

74. K. J. Bachmann and A. F. Schreiner, unpublished results.

75. J. J. Wysocki and P. Rappaport, J.Appl.Phys., 31, 571 (1960).

76. R. K. Yasui and L. W. Schmidt, Conf Rec, IEEE Photo Spec Conf. 8th, Seattle, p 110(1970).

77. H. Hahn, W. Nickels, Z. Anorg. Chem., 303, 107(1960).

This work was performed in the Strahlenchemie Division of the Hahn-Meitner Institut fur Kernforchungs, Berlin between July 1982 to October 1984.

I wish to thank Prof. Tributsch and Dr. H. J. Lewerenz for the invitation to the HMI, support during this work and constructive critism of the manuscript. I am grateful to Prof. K. J. Bachmann for helpful suggestions and the $CuInSe_2$ crystals, to my colleagues in the photoelectrochemistry group at HMI for useful discussions and to Dr.J.Lillie for the text editing system.

RESUME

Shalini Menezes

RESEARCH EXPERIENCE & INTERESTS

- Semiconductor Electrochemistry
- Photoelectrochemical Solar Cells
- Solid State Devices
- Surfaces, Interfaces and Films
- Corrosion of Metals and Alloys
- Materials Characterization
- Polyelectrolytes
- Electroplating Mechanisms
- Mass Transport, Optoelectrochemical, Computer, Surface Analytical and Radioisotope techniques.

EMPLOYMENT

- Hahn-Meitner Institut, Berlin, FRG, 1982-84
  Wissenschafliche Angstellte, Ber. Stralenchem.
- Bell Laboratories, N. J., USA, 1974-82
  Member of Technical Staff, Phys. Chem. Research
- Ciba-Geigy, N. Y., USA, 1974
  Research Assistant, Corporate Research Dept.
- Seton Hall Univ., N. J., USA, 1971-73
  Teaching/Research Assistant, Chemistry Dept.
- Bombay Univ. India, 1966, 1969-70
  Laboratory Instructor, Physics/Chemistry Dept.

EDUCATION

M.S. Chemistry, Seton Hall Univ., N.J.,1973
Dissertation: Diffusion in Polyelectrolytes

M.S., Physical/Nuclear Chemistry, Bombay Univ.,1968

B.S., Chemistry, Physics(minor), Bombay Univ., 1966